Seismic Imaging of the Mantle Transition Zone

by

Qin Cao

SUBMITTED TO THE DEPARTMENT OF EARTH, ATMOSPHERIC AND PLANETARY SCIENCES IN PARTIAL FULFILLMENT OF THE REQUIREMENTS FOR THE DEGREE OF

DOCTOR of PHILOSOPHY

AT THE
MASSACHUSETTS INSTITUTE OF TECHNOLOGY

February 2012

© 2012 Massachusetts Institute of Technology
All rights reserved.

ARCHIVES

MASSACHUSETTS INSTITUTE OF TECHNOLOGY
MAR 14 2012
LIBRARIES

Signature of Author: _____
Department of Earth, Atmospheric and Planetary Sciences
Oct 21, 2011

Certified by: _____
Robert D. van der Hilst
Schlumberger Professor of Earth and Planetary Sciences
Thesis Supervisor

Certified by: _____
Maarten V. de Hoop
Professor, Purdue University
Thesis Co-Supervisor

Accepted by: _____
Maria T. Zuber
E.A. Griswold Professor of Geophysics
Head, Department of Earth, Atmospheric and Planetary Sciences

Seismic Imaging of the Mantle Transition Zone

by

Qin Cao

Submitted to the Department of Earth, Atmosphere and Planetary Sciences
on October 21, 2011, in partial fulfillment of the
requirements for the degree of
Doctor of Philosophy

Abstract

In this thesis, we developed a generalized Radon transform of *SS* precursors for large-scale, high-resolution seismo-stratigraphy of the upper mantle transition zone. The generalized Radon transform (GRT) is based on the single scattering approximation and maps singularities (reflections) in broad-band data into singularities (reflectors/scatters) in the medium. It is able to detect and characterize mantle discontinuities at a lateral resolution of several hundred kilometers. Synthetic tests with realistic source–receiver distributions demonstrate that the GRT is able to detect and image deep mantle interfaces at correct depths, even in the presence of noise, depth phases, phase conversions, and multiples generated by reverberation within the transition zone. We apply the GRT to ~1,600,000 broadband seismograms to delineate transition zone interfaces beneath distinct tectonic units, including a cross-section in the northwest Pacific Ocean that is far away from known down- and up-wellings, the volcanic islands of Hawaii, and the northwest Pacific subduction system. We account for smooth 3D mantle heterogeneity using first-order perturbation theory and independently derived global tomography models. Through integration with mineral physics data, the GRT seismic sections can put important constraints on the mantle temperature and mineralogy of the transition zone.

Our GRT imaging results beneath the Central Pacific (including the Hawaii hotspot) reveal a more complicated mantle convection picture than a thin narrow vertical mantle "plume" passing through the transition zone. We found an 800- to 2000-kilometer-wide thermal anomaly (with a maximum temperature increase of ~300 to 400 kelvin) deep in the transition zone west of Hawaii, by explaining the 410 and 660 km discontinuity topographies with olivine and garnet transitions in a pyrolitic mantle. According to our geodynamical modeling study of mantle upwellings, this might suggest that the hot materials feeding the Hawaii volcanoes do not rise from the lower mantle directly through a narrow vertical plume but may accumulate near the base of the transition zone before being entrained in flow toward Hawaii. In the GRT images of the subduction system, we found a deepened 660 km discontinuity in the slab that penetrates directly into the lower mantle according to tomography results. In another cross-section, where tomography results show that the slab is stagnant above the top of the lower mantle, we found broadening of the 660 km discontinuity signals at both edges of the slab. No

corresponding uplift of the 410 km discontinuity is found. However, deepening of the 410 km discontinuity is observed beneath the continental side of the subduction system in both cross-sections, indicating hot anomalies at 410 km depth at the continental side if only the thermal effect is playing a role.

Thesis Supervisor: Robert D. van der Hilst
Title: Schlumberger Professor of Earth and Planetary Sciences

Thesis Co-Supervisor: Maarten V. de Hoop
Title: Professor, Purdue University

Acknowledgement

I would like to take this opportunity to thank many people I encountered during my study at MIT. Without them, this dissertation would not have been possible.

I would like to first thank my advisor Prof. Rob van der Hilst for offering me the opportunity to study at MIT, and for spending a lot of time and effort helping me overcome difficulties I met in the thesis projects. I am also grateful to my co-advisor Prof. Maarten de Hoop. Each time I discussed with him, I benefited greatly from his deep insights on seismic imaging problems and was always inspired by his enthusiasm about mathematics and seismology.

Second, I would like to thank the professors in my thesis committee, for their valuable advices on improving this thesis. In particular, I would like to thank Prof. Brad Hager and Prof. Dan Shim. I was so fortunate to have Brad as my second general exam project adviser. The observations from our modeling work finally gave rise to one of the core ideas behind our publication in *Science*. I am also grateful to Prof. Dan Shim, for taking precious time out of his busy schedule to discuss the mineral physics implications of our seismic images. This dissertation would never be possible without his deep understanding of the transition zone minerals.

I also wish to thank my fellow students and friends at MIT and at Boston, for all their emotional support, caring and nice jokes. In particular I greatly appreciate Ms. Sue Turbak and Ms. Carol Sprague's help all these years. They made me life much easier. I will never forget their thoughtfulness and considerateness.

I would also like to thank Shell Oil Company for awarding me a MIT-SHELL Energy Initiative Fellowship, and to thank Mr. Dirk Smit, Mr. Colin Perkins, Mr. Peng Shen, Mr. Fons Ten Kroode and Mr. René-Édouard Plessix for hosting me and teaching me exploration seismology during my internships in the summer of 2009 and 2010. These two summers are the most productive summers for me.

Finally, and most importantly, I want to thank my parents for allowing me to study abroad, understanding and supporting me during my Ph.D. study. To them I dedicate this thesis.

Table of Contents

List of Figures

Chapter 1

Introduction

1.1 Background and motivation

The upper mantle transition zone (here defined in a broad sense as the region between 300 and 1000 km depth) is the key to understanding the thermal/chemical state of and dynamic processes in the Earth's mantle. Seismically, this region is characterized by rapid velocity and density jumps, which are referred to as upper mantle discontinuities and often attributed to mineral phase transitions (e.g., *Ringwood, 1975; Bina and Helffrich, 1994*). The existence, depth variations (that is, topography), and geographic variability of these upper mantle discontinuities can be used as a thermal and chemical probe to study the deep interior of the Earth.

In recent years, significant progress has been made in seismology to constrain first-order properties of upper mantle discontinuities (see *Shearer, 2000; Deuss, 2009* for recent reviews). The most robust observations concern the prominent seismic discontinuities near 410 and 660 km depth (e.g., *Shearer and Masters, 1992; Shearer, 1993; Gossler and Kind, 1996; Flanagan and Shearer, 1998; Gu et al., 1998; Flanagan and Shearer, 1999; Gu and Dziewonski, 2002; Lebedev and van der Hilst, 2002, 2003; Chambers et al., 2005a, b; Deuss et al., 2006; Schmerr and Garnero, 2006; An et al., 2007; Rost and Thomas, 2009*). There are many reports of discontinuities at other depths in the transition zone, most notably near 520 km depth (e.g., *Shearer, 1990; Deuss and Woodhouse, 2001*). For convenience, in this

thesis, we will refer to the 410, 520 and 660 km discontinuities as the 410', 520', and 660', respectively, although the actual depths to these discontinuities vary geographically.

Mineral physics experiments data have shown that the 410', 520', and 660' are generally consistent with isochemical phase transitions in the $(Mg,Fe)_2SiO_4$ olivine system: olivine to wadsleyite (~14 GPa; ~410 km depth), wadsleyite to ringwoodite (~520 km), and ringwoodite to perovskite and ferropericlase (~23 GPa; ~660 km depth) (*Ringwood, 1975; Ita and Stixrude, 1992; Weidner and Wang, 2000; Li and Liebermann, 2007*). The latter is also referred to as the post-spinel transition. The measurements of the depth to a discontinuity, which can be converted to the pressure at which the associated phase transition occurs, can be used to infer local temperature and chemical composition based on the thermodynamics of and effects of chemistry on the transition. The relationship between variations in discontinuity depth and variations in local temperature is given by the Clapeyon slope of the corresponding phase transition, that is, the slope of the transition curve in a pressure (P) versus temperature (T) phase diagram (dP/dT). The Clapeyron slope of the olivine to wadsleyite transition is positive, which implies that the presence of a hot (cold) anomaly will lead to a deeper (shallower) 410'. By contrast, the Clapeyron slope of the post-spinel transition is negative, which means that the presence of a hot (cold) anomaly will result in a shallower (deeper) 660'. The exact values of the Clapeyron slopes are debated, but reasonable estimates are 4 MPa/K (*Katsura et al., 2004*) for olivine to wadsleyite and -2.7 MPa/K for the post-spinel transition (*Irifune and Isshiki, 1998*). Additional phase transitions, for instance in garnet, have also been reported to occur in the depth range of the transition zone (e.g. *Vacher et al., 1998; Weidner and Wang, 2000*).

The global existence of 410' and 660' is no longer disputed. But owing to the limited data coverage and resolution of commonly used imaging methods, the level of (anti)correlation between the 410' and 660' is still debated (*Shearer, 2000*) and the mapping of fine scale regional topographies of 410' and 660' is still beyond reach for many geographic regions. For example, there are regional seismic studies

of the transition zone discontinuities around the Hawaii hotspot (*Deuss, 2007; Li et al., 2000*), which is regarded as the archetype of plume-related hotspot activity. But the results from these studies are inconclusive regarding the location and size of the mantle thermal anomaly responsible for the hotspot. *SS* precursor stacks near the locations of hotspots identified in the catalog of *Courtillot et al.* (2003) suggests larger-than-average depths for the 410-km discontinuity in about two-thirds of the cases (*Deuss, 2007*). Because the lateral resolution of *SS* precursor stacks is of the order of several thousand kilometers (as explained in the next section), which is likely to be larger than the plume diameter (probably of the order of a few hundred kilometers, see *Nataf, 2000*), traditional *SS* studies may fail to detect the plume, even in the places with good *SS* bounce point coverage. Receiver function methods have also been applied to measure the transition zone thickness underneath seismic stations deployed on the Hawaii islands (*Li et al., 2000*). The lateral resolution of the receiver function method is several hundred kilometers. However, because of the lack of ocean-bottom seismometers, high-resolution imaging of the 410' and 660' is limited to relatively small oceanic regions. The lateral extent of the 520' is still debated, and it is uncertain if other (seismologically detectable) interfaces exist in or near the transition zone.

High resolution, large scale imaging of transition zone structure over diverse geotectonic settings will help determine the existence, regional fine-scale topographies, and the lateral extent of mantle transition zone discontinuities across different geotectonic domains. Collectively, such information would help constrain *in situ* mantle thermal, chemical and dynamic conditions of the Earth's interior (including the existence, depth of origin, and morphology of plumes).

1.2 Why do we need inverse scattering?

In view of the important implications for our understanding of the thermochemical state of and

dynamic processes in Earth's mantle, many seismological investigations have been devoted to the detection and characterization of mantle discontinuities. The receiver function method uses converted waves and has been widely employed for high-resolution imaging of transition zone structures (*Vidale and Benz, 1992; Petersen et al., 1993; Niu and Kawakatsu, 1995; Bostock, 1996; Vinnik et al., 1996; Shen et al., 1996, 1998; Dueker and Sheehan, 1997; Li et al., 1998; Gurrola and Minster, 1998; Castle and Creager, 1998*). However, because of the near-vertical raypaths of the converted waves beneath the seismograph stations, the applicability of this method is limited to the regional studies of transition zone discontinuities beneath continents and island arcs. By implication, receiver function analysis cannot be used to constrain transition zone structure beneath regions without seismographic stations, which includes most continental and almost all oceanic regions.

Another approach concerns common mid-point (CMP) stacking, which involves the stacking of waveforms associated with reflections from discontinuities within a predefined geographical bin. However, the assumption that the properties (including depth) of the discontinuities are invariant across the geographical bins over which data are stacked limits lateral resolution and may bias depth estimates if the undulating interfaces are unevenly sampled. The size of the bin is usually several thousand kilometers in radius (of the scale of the Fresnel zone of the waves used). *SS* precursors scattered from the transition zone (i.e. S_dS waves, with subscript d denoting the depth of the discontinuity where the underside reflection occurs) are the most widely used phase groups in the CMP stacking approach (*Shearer and Masters, 1992; Shearer, 1993; Gossler and Kind, 1996; Lee and Grand, 1996; Gu et al., 1998; Flanagan and Shearer, 1998; Deuss, 2009*). The travel time difference between *SS* reflection and *SS* precursors, which mainly results from the two-way *S* wave travel time within the transition zone, provides valuable information about the velocity structure and interface depth at the reflection point, and the overlap of raypaths near the Earth's surface essentially removes any effect associated with the velocity structure near the earthquake source and receiver. To enhance the signal-to-noise ratio of the

weak signal of *SS* precursors, waveforms with midpoints falling in a common geographic bin (e.g. 10 degrees in radius) are stacked after normal movement out correction. Then the travel time differences between *SS* and *SS* precursors (e.g. $S_{660}S$, $S_{410}S$) are converted to depths to determine at which depth the reflectors (discontinuties) occur.

The bounce points of *SS* on the Earth's surface are more evenly distributed over the globe than the earthquake sources and seismic stations that provide the seismic data, and CMP stacking has been successfully applied to make global maps of 410' and 660' topographies (*Shearer and Masters, 1992; Shearer, 1993; Gossler and Kind, 1996; Lee and Grand, 1996; Gu et al., 1998; Flanagan and Shearer, 1998; Deuss, 2009*). However, because of the assumption of flat reflectors (discontinuities) within each geographic bin underlying the CMP stacking method, only the average topography in the bin can be obtained, which not only limits the lateral resolution but also produces substantial differences between results based on different subsets of the available data.

In this thesis, we developed and applied the generalized Radon transform (GRT), an inverse scattering technique, of the global broadband wavefield comprising *SS* reflections and their precursors to detect and characterize transition zone interfaces. The GRT is based on the single scattering approximation, and unlike conventional CMP stacking, it does not assume planar interfaces but reconstructs laterally contiguous (and possibly undulating) discontinuities from the alignment of singularities (point scatters) in the medium. The GRT maps singularities in broad-band data (that is, scattered waves) into singularities (reflectors) in the medium (*Beylkin, 1985; De Hoop and Brandsberg-Dahl, 2000*). It can yield seismic images at a lateral resolution of a few 100 km, well within the Fresnel zones of *SS* waves. So-called common image point gathers are produced from the broadband *SS* wavefield. These image gathers represent radial profiles of changes in elastic parameters beneath each image point on the surface. The juxtaposition of such profiles creates 3-D laterally continuous images, which will enable us to detect and measure the depth to the discontinuities,

characterize the properties of these interfaces, and determine the lateral variation (e.g., intermittency, topography, correlation) of the interface properties at unprecedented scale.

The applicability of the GRT is not limited to places with seismic stations. We can apply this method to any place where the *SS* bounce points sampling is dense enough. The Hawaii islands are almost at the center of the Pacific Ocean and hence in the middle of the dense seismic networks on the North American continent and active seismic zones of the west Pacific rim, which (along with its central role in discussions about mantle upwellings) makes the Hawaii islands attractive study targets for GRT imaging. Also, the GRT does not rely on any prior assumptions about the presence, lateral continuity and depth of the discontinuities; the existence and the locations of the scatters will be inferred directly from data. By making use of the scattered waves, we are able to extract more information from currently available data compared to using CMP stacking, and we will be able to carry out 3-D exploration-type high-resolution seismic imaging over large geographical regions.

The GRT developed in this thesis is an adaptation of a successful pilot study of *D*" imaging with broadband *ScS* and *SKKS* waves (*Wang et al., 2006, 2008*).

1.3 Outline of thesis

In **Chapter II** (published in *Physics of Earth and Planetary Interiors* – vol. 180, p. 80-91, 2010) we outline the essential elements of the theory behind generalized Radon transform and the data processing steps used in the GRT of *SS* precursors to image the transition zone interfaces. Synthetics tests are carried out to demonstrate the feasibility and robustness of this method. Then, as a proof-of-concept, we apply the GRT method to obtain images for a cross-section in the northwest Pacific. In **Chapter III** (published in *Science* – vol. 33 2, p.1068-1071, 2011) we apply the GRT method to the Central Pacific, including the Hawaii hotspot. The seismic images are interpreted in terms of mineral physics and

geodynamics. In **Chapter IV**, we study the dynamics of the plume evolution in the presence of the ambient mantle flow and mineral phase transitions, using finite element modeling. In **Chapter V** we show preliminary images for cross-sections across northwest Pacific subduction systems. We also show the latest images for the same locations as in **Chapter II** and **Chapter III**, with a recently updated dataset. In **Chapter VI** we summarize the key results obtained in the course of this study and discuss possible avenues for future work.

References Cited

An, Y., Y. J. Gu, and M. D. Sacchi, 2007. Imaging mantle discontinuities using least squares Radon transform. *J. Geophys. Res.*, 112, B10303.

Beylkin, G., 1985. Imaging of discontinuities in the inverse scattering problem by inversion of a causal generalized Radon transform. *J. of Math. Phys.*, 26, 99–108.

Bostock, M. G., 1996. *Ps* conversions from the upper mantle transition zone beneath the Canadian landmass. *J. Geophys. Res.*, 101, 8393 – 8402.

Castle, J. C., and K. C. Creager, 1998. Topography of the 660-km seismic discontinuity beneath Izu-Bonin: Implications for tectonic history and slab deformation. *J. Geophys. Res.*, 103, 12,511 – 12,527.

Chambers, K., J. H. Woodhouse, and A. Deuss, 2005a. Reflectivity of the 410-km discontinuity from PP and SS precursors. J. *Geophys. Res.* 110, doi:10.1029/2004JB003345.

Chambers, K., J. H. Woodhouse, and A. Deuss, 2005b. Topography of the 410-km discontinuity from *PP* and *SS* precursors. *Earth Planet. Sci. Lett.*, 235, 610–622.

Courtillot, V., A. Davaille, J. Besse, and J. Stock, 2003. Three distinct types of hotspots in the Earth's mantle. *Earth and Planet. Sci. Lett.*, 205,295-308.

De Hoop, M. V. and S. Brandsberg-Dahl, 2000. Maslov asymptotic extension of generalized Radon transform inversion in anisotropic elastic media: A least-squares approach. *Inverse Problems*, 16, 519–562.

Dueker, K. G., and A. F. Sheehan, 1997. Mantle discontinuity structure from midpoint stacks of converted *P* to *S* waves across the Yellowstone hot spot track. *J. Geophys. Res.* ,102, 8313–8327.

Deuss, A., and J.H. Woodhouse, 2001. Seismic observations of splitting of the mid-transition zone discontinuity in earth's mantle. *Science*, 294, 354–357.

Deuss, A., S.A.T. Redfern, K. Chambers, and J. H. Woodhouse, 2006. The nature of the 660-kilometer discontinuity in Earth's mantle from global seismic observations of *PP* precursors. *Science*, 311, 198–201.

Deuss, A., 2007. Seismic observations of transition zone discontinuities beneath hotspot locations. Special Papers of the Geological Society of America, 430, *Plates, plumes and Planetary Processes edited by Foulger, G. R. and D. M. Jurdy*, 121-136.

Deuss, A., 2009. Global observations of mantle discontinuities using *SS* and *PP* precursors. *Surv. Geophys.*, 30 4–5, 301–326.

Flanagan, M. P., and P. M. Shearer, 1998. Global mapping of topography on transition zone velocity discontinuities by stacking *SS* precursors. *J. Geophys. Res.*,103, 2673– 2692.

Flanagan, M. P., and P.M. Shearer, 1999. A map of topography on the 410-km discontinuity from PP precursors. *Geophys. Res. Lett.*, 26, 549-552.

Gossler, J., and R. Kind, 1996. Seismic evidence for very deep roots of continents. *Earth Planet. Sci. Lett.*, 138, 1– 13.

Gu, Y., A. M. Dziewonski, and C. B. Agee, 1998. Global de-correlation of the topography of transition zone discontinuities. *Earth Planet. Sci. Lett.*, 157, 57–67.

Gu, Y.J., and A.M. Dziewonski, 2002. Global variability of transition zone thickness. *J. Geophys. Res.* 107(B7), doi:10.1029/2001JB000489.

Gurrola, H., and J. B. Minster, 1998. Thickness estimates of the upper-mantle transition zone from bootstrapped velocity spectrum stacks of receiver functions. *Geophys. J. Int.*, 133, 31–43.

Irifune, T. and M. Isshiki, 1998. Iron partitioning in a pyrolite mantle and the nature of the 410-km seismic discontinuity. *Nature*, 392, 702705.

Ita, J. and L. Stixrude, 1992. Petrology, elasticity and composition of the mantle transition zone. *J. Geophys. Res.*, 97, 6849–6866.

Katsura, T., H. Yamada, O. Nishikawa, M. Song, A. Kubo, T. Shinmei, S. Yokoshi, T. Aizawa, T. Yoshino, W. M. J., and E. Ito, 2004. Olivine-wadsleyite transition in the system $(Mg,Fe)_2SiO_4$. *Journal of Geophysical research*, 109, B02209.

Lebedev, S., S. Chevrot, and R. D. van der Hilst, 2002. Seismic evidence for olivine phase change at the 410- and 660-kilometer discontinuities. *Science*, 296, 1300–1302.

Lebedev, S., S. Chevrot, and R. D. Van der Hilst, 2003. Correlation between the shear-speed structure and thickness of the mantle transition zone. *Phys. Earth Planet. Int.*, 136, 25–40.

Lee, D.-K., and S. Grand, 1996. Depth of upper mantle discontinuities beneath the East Pacific Rise, *Geophys. Res. Lett.*, 23, 3369– 3372.

Li, B. and R. Liebermann, 2007. Indoor seismology by probing the earth's interior by using sound velocity measurements at high pressures and temperatures. *Proc. Natl. Acad. Sci.*, 104, 9145–9150.

Li, X., R. Kind, K. Priestly, S. V. Sobolev, F. Tilmann, X. Yuan, and M. Weber, 2000. Mapping the Hawaiian plume conduit with converted seismic waves. *Nature*, 405, 938-941.

Li, A., K. M. Fischer, M. E. Wysession, and T. J. Clarke, 1998. Mantle discontinuities and temperature under the North American continental keel. *Nature*, 395, 160–163.

Nataf, H.-C., 2000. Seismic imaging of mantle plumes. *Annu. Rev. Earth Planet. Sci.*, 28, 391-417.

Niu, F., and H. Kawakatsu, 1995. Direct evidence for the undulation of the 660-km discontinuity beneath Tonga: Comparison of Japan and California array data. *Geophys. Res. Lett.*, 22, 531– 534.

Petersen, N., L. P. Vinnik, G. Kosarev, R. Kind, S. Oreshin, and K. Stammler, 1993. Sharpness of the mantle discontinuities. *Geophys. Res. Lett.*, 20, 859– 862.

Ringwood, A.E., 1975. *Composition and petrology of the Earth's mantle. McGraw-Hill,* New York

Rost, S. and C. Thomas, 2009. Improving seismic resolution through array processing techniques. *Surveys in Geophysics*, 30, Issue 4-5, 271-299.

Schmerr, N., and E. Garnero, 2006. Investigation of upper mantle discontinuity structure beneath the central Pacific using *SS* precursors. *J. Geophys. Res.*, 111, B08305, doi:10.1029/2005JB004197.

Shearer, P. M., 1990. Seismic imaging of upper-mantle structure with new evidence for a 520-km discontinuity. *Nature*, 344, 121-126.

Shearer, P. M., and G. Masters, 1992. Global mapping of topography on the 660-km discontinuity. *Nature*, 355, 791– 796.

Shearer, P. M., 1993. Global mapping of upper mantle reflectors from long-period *SS* precursors. *Geophys. J. Int.*,115, 878–904.

Shearer, P. M., 2000. Upper mantle seismic discontinuities. *Geophys Monogr*, 117, 115–131.

Shen, Y., S. C. Solomon, I. T. Bjarnason, and G. M. Purdy, 1996. Hot mantle transition zone beneath Iceland and the adjacent Mid-Atlantic Ridge inferred from P-to-S conversions and the 410- and 660-km discontinuities. *Geophys. Res. Lett.*, 23, 3527– 3530.

Shen, Y., A. F. Sheehan, K. G. Dueker, C. de Groot-Hedlin, and H. Gilbert, 1998. Mantle discontinuity structure beneath the southern East Pacific Rise from P-to-S converted phases. *Science*, 280, 1232–1235.

Vacher, P., A. Mocquet, C. Sotin, 1998. Computations of seismic profiles from mineral physics: the importance of the non-olivine components for explaining the 660 km depth discontinuity. *Phys. Earth Planet Inter.*,106, 275–298.

Vidale, J. E., and H. M. Benz, 1992. Upper-mantle seismic discontinuities and the thermal structure of subduction zones. *Nature*, 356, 678– 683.

Vinnik, L. P., G. Kosarev, and N. Petersen, 1996. Mantle transition zone beneath Eurasia. *Geophys. Res. Lett.*, 23, 1485– 1488.

Wang, P., M. V. de Hoop, R. D. van der Hilst, P. Ma, and L. Tenorio, 2006. Imaging of structure at and near the core mantle boundary using a generalized Radon transform: I- construction of image gathers. *J. Geophys. Res.*, 111, 1230.

Wang, P., De Hoop, M.V., and Van der Hilst, R.D., 2008. Imaging of the lowermost mantle (D") and the core-mantle boundary with SKKS coda waves. *Geophysical Journal International*, 175, 103-115.

Weidner, D. and Y. S. Wang, 1998. Chemical and clapeyron induce buoyancy at the 660 km discontinuity. *J. Geophys. Res.*, 103, 7431–7441.

Weidner, D. and Y.S. Wang, 2000. Phase transformations: implications for mantle structure. In: Karato S, Forte A, Liebermann R, Masters G, Stixrude L (eds) Earth's deep interior: mineral physics and tomography from the atomic to the global scale, vol 117, *AGU geophysical monograph. American Geophysical Union, Washington, DC*, 215–235.

Chapter 2

Imaging the upper mantle transition zone with a generalized Radon transform of *SS* precursors[†]

Abstract

We demonstrate the feasibility of using inverse scattering for high-resolution imaging of discontinuities in the upper mantle beneath oceanic regions (far from sources and receivers) using broadband wavefield observations consisting of *SS* and its precursors. The generalized Radon transform (GRT) that we developed for this purpose detects (in the broadband data) signals due to scattering from elasticity contrasts in Earth's mantle. Synthetic tests with realistic source-receiver distributions demonstrate that the GRT is able to detect and image deep mantle interfaces, even in the presence of noise, depth phases ('ghosts'), phase conversions, and multiples generated by reverberation within the transition zone. As a proof of concept, we apply the GRT to ~50,000 broadband seismograms to delineate interfaces in the depth range from 300 to 1000 km beneath the northwest Pacific. We account for smooth 3-D mantle heterogeneity using first-order perturbation theory and independently derived global tomography models. The preliminary results reveal laterally continuous (but undulating) scatter zones near 410 and 660 km depth and a weaker, broader, and more complex structure near 520 km depth. The images also suggest the presence of multiple, laterally intermittent interfaces near 350 km and between 800-1000 km depth, that is, above and below the transition zone *sensu stricto*. Filtering of the data (we consider four pass bands: 20-50s, 10-50s, 5-50s, and 2-50s) reveals a prominent frequency dependence of the magnitude, width, and complexity of the interfaces, in particular of the scatter zone near 520 km depth; such dependencies may put important constraints on the mineralogy and phase chemistry of the transition zone.

Key words: transition zone, upper mantle discontinuities, inverse scattering, generalized Radon transform, *SS* precursors

2.1 Introduction

The upper mantle transition zone, here taken broadly as the depth interval between 300 and 1000 km depth, is marked by rapid radial changes in elasticity and mass density associated with phase

[†]Published as: Q. Cao, P. Wang, R. D. van der Hilst, M. de Hoop, and S.-H. Shim. Imaging the upper mantle transition zone with a generalized Radon transform of SS precursors, *Physics of Earth and Planetary Interiors*, 180, 80-91, 2010.

transformations in mantle silicates (Figure 2-1) (e.g., *Ringwood, 1975; Weidner and Wang, 2000; Li and Liebermann, 2007*). With seismic imaging one can estimate the depth to and the change in elasticity and mass density across such phase boundaries. Combined with mineral physics data this information puts constraints on local temperature, composition, and mineral phase, and the geographic variation of these parameters provides insight into large scale geodynamical processes (*Jeanloz and Thompson, 1983; Helffrich, 2000; Shearer, 2000; Weiner and Wang, 2000; Schmerr and Garnero, 2006; Li and Liebermann, 2007*).

Using a variety of top- and underside reflections and phase-converted waves, a number of seismic investigations have observed the global existence of what are usually referred to as '410' and '660' discontinuities (e.g., *Shearer and Masters, 1992; Shearer, 1993; Gossler and Kind, 1996; Flanagan and Shearer, 1998; Gu et al., 1998; Flanagan and Shearer, 1999; Gu and Dziewonski, 2002; Lebedev and van der Hilst, 2002, 2003; Chambers et al., 2005a, b; Deuss et al., 2006; Schmerr and Garnero, 2006; An et al., 2007; Rost and Thomas, 2009*), and a '520' discontinuity has been reported in some regions (e.g., *Shearer, 1990; Deuss and Woodhouse, 2001*). Many aspects of these discontinuities can be explained by phase transitions in the olivine system (olivine to wadsleyite, wadsleyite to ringwoodite, and ringwoodite to perovskite and ferro-periclase, respectively) (*Ringwood, 1969, 1975, 1991; Katsura and Ito, 1989; Bina and Helffrich, 1994; Weidner and Wang, 2000; Shim et al., 2001; Lebedev et al., 2002, 2003; Fei et al., 2004; Weidner et al., 2005; Li and Liebermann, 2007*), but not all seismic observations are consistent with transformations in a simple, isolated MgO-FeO-SiO_2 system. For example, despite the opposite signs of their Clapeyron slopes, on a global scale the '410' and '660' topographies are not convincingly anti-correlated (*Gu et al., 1998, 2003; Flanagan and Shearer, 1998; Helffrich, 2000; Shearer, 2000; Gu and Dziewonski, 2002*). Furthermore, the inferred global depth variations in '410' are generally smaller than in '660' (*Shearer and Masters, 1992; Flanagan and Shearer, 1998; Gu et al., 2002, 2003*), even though its Clapeyron slope is steeper.

Such inconsistencies suggest that published topography estimates or laboratory measurements are inaccurate or that more complex compositions and mineralogy must be considered. Laboratory experiments show that the depth to, the magnitude and transition profile of radial changes across discontinuities depend not only on temperature and pressure but also on, for instance, major element composition and partitioning, and the presence of water or (silicate) melt (e.g, *Weidner et al., 2005; Li and Liebermann, 2007*). Seismological evidence for such complexity has begun to emerge (*Deuss et al., 2006*), and manifestation of these effects on different length scales may degrade global-scale correlation between the depth variations of the discontinuities.

To enable better estimation of *in situ* mantle temperature, mineralogy, and composition from seismic data we must improve our capability to detect, image, and characterize seismic discontinuities. Receiver functions and near-source reflections have been used for regional-scale imaging of mantle discontinuities beneath dense receiver arrays or near (deep) seismic sources (*Collier and Helffrich, 1997; Castle and Creager, 2000; Rondenay et al., 2005; Zheng, 2007;* to name a few). Here we develop a method that can improve detection and imaging of transition zone over large geographical regions (including those far away from sources and receivers) with broadband *SS* data (Figure 2-2).

Since the pioneering studies by *Shearer* (1991), most attempts to determine lateral variations in the depth to the main upper mantle discontinuities with *SS* and *PP* and their precursors have employed form of common-midpoint (CMP) stacking (e.g., *Shearer and Master, 1992; Shearer, 1993; Gossler and Kind, 1996; Gu et al., 1998; Flanagan and Shearer, 1998; Gu and Dziewonski, 2002; Chambers et al., 2005a, b; Schmerr and Garnero, 2006; Houser et al., 2008; Lawrence et al., 2008*), with the mid-point corresponding to the bounce-point of the *SS* or *PP* waves. This method – see *Deuss* (2009) and *Rost and Thomas* (2009) for recent reviews – involves the stacking of (move-out corrected) waveforms over spatial bins followed by a time-to-depth conversion using a standard 1D reference model (and corrections for 3D heterogeneity inferred from tomography). The size of the geographical

bins used is often chosen to correspond loosely to the scale of the Fresnel zone of the associated *SS* or data, and stacking over bins with a radius of 10° is common (*Deuss, 2009*), but the complex shape of Fresnel zone (e.g., *Neele et al., 1997; Chaljub and Tarantola, 1997; Zhao and Chevrot, 2003; Dahlen, 2005*) can be accounted for to increase spatial resolution (*Lawrence et al., 2008*). Fundamentally, however, stacking over geographical regions implies substantial spatial averaging and thus the full resolving power of migration has been lost.

In contrast to stacking over bins followed by migration, methods based on inverse scattering directly localize and characterize point scatterers, and the spatial alignment of these scatterers then outlines a scatter interface or "reflector". This localization is based on the intersection of isochron surfaces and can be done with a spatial resolution much better than the Fresnel zones of the associated waves. With synthetic data, *Shearer et al.* (1999) demonstrated the potential of least-squares Kirchoff migration (inversion) of *SS* precursors for high resolution imaging of upper mantle discontinuities. Application to the then available data yielded noisy images, however, with few, if any, laterally coherent structures. To suppress effects of 'noise' (in the presence of uneven data coverage) *Shearer et al.* (1999) 'damped' the inversion, but the implied spatial smoothing rendered images at a spatial resolution similar to that obtained from the above-mentioned time migration followed by time-to-depth conversion. Given the spectacular increase in data quality and quantity – nicely illustrated in Figure 2 of *et al.* (2008) – it is likely that application of the Kirchoff migration introduced by Shearer and a decade ago would now give more satisfactory results. But it is also possible to improve the inverse scattering method itself. We present here a generalized Radon transform (GRT), which has better noise-suppression capabilities than Kirchoff migration (because of the different use of data redundancy) and it accounts differently for complex wave phenomena such as caustics. The GRT was first used for seismic imaging in the 1980s (*Beylkin et al., 1985; Miller et al., 1987*), see reviews by *Rondenay* (2005) and *Gu* (2009), but in recent years it has been used for large-scale imaging of deep mantle structure

ScS (*Chambers et al., 2006; Wang et al., 2006; Ma et al., 2007; Van der Hilst et al., 2007*) or *SKKS* (*Wang et al., 2008*).

The main objective of this paper is to present a 3-D GRT of the *SS* wavefield (including precursors) and to demonstrate the feasibility and promise of using this GRT for high-resolution transition zone imaging even far away from sources and receivers. We focus this feasibility study on the transition zone beneath the northern part of the Pacific Ocean (Figure 2-2) because the density of *SS* bounce points is high and because it is far away from known subduction (along NW Pacific island arcs) and presumed upwelling (beneath Hawaii) so that not much structural complexity is expected. In the sections below, we present the method, describe the selection and processing of data, illustrate the performance of the 3-D GRT on synthetic data, and – as a proof of concept – present (for different frequencies) a 2-D, a 20°-long seismic section of the transition zone.

2.2 Methodology

2.2.1 Concept of Inverse Scattering

Inverse scattering uses signal from a large number of seismic data to localize elasticity contrasts in the sub-surface by determining how much scattering (reflection) at a specific point $\mathbf{y}=(x,y,z)$ contributes to observed signal in recorded seismograms. Data in a narrow time window of a record associated with a fixed source-receiver pair can be due to scattering anywhere along a surface of constant travel time from source to scatter point to receiver. This isochron, in its finite-frequency form, is, in fact, the sensitivity kernel for inverse scattering. [We note that in analogy of raypaths versus finite frequency kernels for transmission and reflection tomography (e.g., *Dahlen et al., 2000; De Hoop and Van der Hilst, 2005; Tromp et al., 2005; De Hoop et al., 2006*), in the context of ray theory the isochron would have an infinitesimally narrow width, but in finite frequency theory the isochron would have

multi-scale properties.] The distribution of sensitivity along each isochron is generally non-uniform and is determined by the intersection of the isochron with the Fresnel volume of the scattered phases. The total data sensitivity to structure at a certain sub-surface location is then the cumulative contribution from all isochrons through that point. While fully accounting for Fresnel zones, this allows the resolution of structure at the Rayleigh diffraction limit, at scales smaller than the Fresnel zones of the associated phases (*Spetzler and Snieder, 2004*), provided that data from a sufficiently broad distance and azimuth range is available in order to suppress imaging artifacts (*Stolk and De Hoop, 2002*).

2.2.2 The generalized Radon transform (GRT)

Because the development of the GRT used in our study follows closely the formulation for lowermost mantle imaging with *ScS* and *SKKS* reflections (*Wang et al., 2006, 2008*) we only mention the most relevant aspects. In essence, the GRT estimates the locations of local contrasts in elasticity (scatter points) in Earth's interior from their contribution to the scattered wave field. With the single scattering (Born) approximation, these contrasts δc are considered local perturbations in density and elasticity relative to a smooth background c_0. For our application, the smooth background model is derived from the *ak135* reference Earth model (*Kennett et al., 1995*) by replacing the first-order transition zone discontinuities by gradual transitions in wavespeed (Figure 2-5), and the interfaces that we aim to image are thus represented as perturbations relative to this smooth background.

The data used by GRT, that is the wavefield δu due to scattering at δc, is modeled as

$$\delta u = F\delta c \,, \tag{1}$$

with F a single scattering operator. To estimate δc from the data one can set up the normal equations,

$$F^* F\delta c = F^* \delta u \,, \tag{2}$$

where F^*, the adjoint of F, is the imaging operator. Using ray theory, F^* yields a GRT while

with the "inverse" of the normal operator F^*F adapts the weighting of the GRT to form an inverse scattering transform:

$$\delta c = (F^*F)^{-1} F^* \delta u . \tag{3}$$

The geometry of the problem is illustrated in Figure 2-3. For each source-receiver pair, most of the energy in the recorded wavefield arrives at a time corresponding to a minimum or maximum two-way (reflection) travel time (T) path, which is commonly referred to as the specular reflection. For mini-max travel time phases (such as SS, $S_{410}S$, and $S_{660}S$), propagation along non-specular propagation paths can produce weak arrivals before or after the main phases. Conversely, for a given source-receiver geometry, arrivals in narrow time interval around a time t can be produced by scatterering anywhere along an isochron defined by $T(x^s, x^r, y) = t$, with x^s and x^r the position of the source and receiver, respectively (Figure 2-3a). In essence, the GRT uses data δu in narrow time windows around t to characterize the strength of scattering at y: for a given sub-surface point y the time t (and the data window used) depends on the source-receiver combination, and for a given (x^s, x^r) record t depends on the position of y (Figure 2-3b).

The total data sensitivity at a particular point y is the accumulation of sensitivities from isochrons t $T(x^s, x^r, y)$ for all source-receiver pairs, weighted by the data in a narrow window around the corresponding time. To describe this process we introduce the migration dip v^m, which is the normal to the isochron at the sub-surface point y for which the contribution to observed data is to be computed (Figure 2-3c). For a (broken) raypath connecting a source at x^s with a receiver at x^r via y, we define p^s the slowness vector (at y) for the ray from x^s to y, and p^r is defined similarly for the ray from x^r to y. slownesses define the migration dip $v^m = p^m/|p^m|$, with $p^m = p^s + p^r$, and the scattering angle θ and azimuth ψ (Figure 2-4c). Conversely, v^m and (θ, ψ) determine p^r, p^s at y, and hence the corresponding x^s, x^r and $t = T(x^s, x^r, y)$. We can thus view the data δu associated with image point y as a function of v^m, θ ,

and ψ – see *Wang et al.* (2006).

For each sub-surface point $\boldsymbol{y}$ an image gather $I(\boldsymbol{y};\theta,\psi)$ is obtained by integrating over all isochrons (with migration dip v^m) that pass through $\boldsymbol{y}$, with each contribution weighted with the corresponding data sample δu and weights W and w that control the sensitivity along the isochrons surfaces:

$$I(\boldsymbol{y};\theta,\psi) = \int_{E_{v^m}} \frac{\delta u(\boldsymbol{y};v^m,\theta,\psi,\boldsymbol{p}^m)^3}{W(\boldsymbol{y};v^m,\theta,\psi)^3 w(\boldsymbol{y};v^m,\theta,\psi)} dv^m \quad . \tag{4}$$

Here, w accounts for ray geometry and places more weight on the specular reflection; W can be used to account for radiation patterns but is not implemented here. A structural image at $\boldsymbol{y}$ can be obtained through statistical inference (*Ma et al., 2007*) or, as is done here, through integration over θ and ψ:

$$I(\boldsymbol{y}) = \iint I(\boldsymbol{y};\theta,\psi)\,d\theta\,d\psi \tag{5}$$

For constant (x,y), (5) yields a radial reflectivity profile at a particular geographic location, and lateral juxtaposition of such 1-D profiles would give a 2-D seismic section.

We note that for underside reflections the range of scattering angles that can be used depends on the depth to the image point $\boldsymbol{y}$ (or interface depth d): the scattering angle generally θ increases (and the radial resolution decreases) with increasing depth of the imaging points and decreasing epicentral (source-receiver) distance (Figure 2-2). Conversely, shallower signal is expected to appear in gathers for smaller θ and structure at greater depth appears at larger θ. This phenomenon, which we refer to as "spatial resolution drift", requires binning in θ.

2.3 Data

For this pilot study we consider the northern Pacific, where the density of *SS* bounce points is high owing to the abundance of sources and receivers along the plate margins and continents surrounding

Pacific basin (Figure 2-2). For *SS* waves with bounce points in a 20°×20° area from 25° – 45° N and 160° – 180°E we retrieve broad-band waveforms from the Data Management Center (DMC) of the Incorporated Research Institutions for Seismology (IRIS). We use hypocenter parameters from the catalog due to *Engdahl et al.* (1998).

The data selection criteria are rather similar to those used in other *SS* studies (*Deuss, 2009*). For data at epicentral distances from 90° to 170° we extract time windows containing *SS* proper and precursors due to scattering in the transition zone. We note – and demonstrate – that interference with phases other than *SS* precursors does not visibly degrade the GRT images. The minimum source magnitude is m_b=5.5 and focal depths are less than 75 km (to reduce contamination by depth phases). Figure 2-4 displays a (transverse component) record section of the data used here, aligned on *SS*, along with predicted travel times according to *ak135*. This record sections reveals $S_{410}S$ and $S_{660}S$ phases at distances less than 130°, with $S_{660}S$ appearing stronger than $S_{410}S$, and arrivals between $S_{410}S$ and $S_{660}S$.

For the data that pass the initial selection criteria we add event parameters from the EHB catalog to the file headers, check (and, if needed, correct) polarization, deconvolve the instrument response, rotate the data to radial and transverse direction, and then use a 4-pole Butterworth filter to band-pass the data between 20-50 s, 10-50 s, 5-50 s, and 2-50 s, respectively, in order to study the frequency dependence of the images. Subsequently, the traces are Hilbert transformed and normalized with respect to *SS*. For the shorter period data (that is, for the T=2-50 s and T=5-50 s bands considered below) we apply a signal-to-noise criterion (with the signal-to-noise ratio defined as the ratio of peak amplitude of SS proper signal to the maximum amplitude of the whole window containing *SS* proper and precursors) and discard data with signal-to-noise ratio smaller than 1/5.

All available data can be used for the calculation of total data sensitivity to structure at a given $\boldsymbol{y}$, but to reduce the computational burden and interference with other phases we restrict the

to records associated with rays with a specular reflection within a certain distance (here 6°) from y. We stress that waveforms are not stacked over these bins and recall that for each image point y a different time window is extracted from a seismogram, so that the total data sensitivity to structure at y is independent from that at adjacent sub-surface image points. Upon imaging, travel times are determined through table interpolation with time corrections for 3D structure from tomography (*Grand, 2002*).

2.4 Tests with synthetic data

We tested the performance of the generalized Radon transform of *SS* precursor with inversions of synthetic data. In all tests, we compute the synthetic wavefields using the actual earthquake-station distribution so that influence on the image of uneven data coverage, including the effects of a realistic focal depth distribution, is the same as for the inversion of the recorded wavefields.

In a first series of tests we use WKBJ *(Chapman, 1978)* synthetics to show that the generalized Radon transform of *SS* precursor data can detect and locate elasticity contrasts in the presence of noise, *P*-to-*S* phase conversions, depth phases, and multiple reflections. For this purpose synthetics for the *SS* wavefield (including $S_{410}S$ and $S_{660}S$) are computed for *ak135*; we use the same source function for all waveforms and the data are filtered using a pass-band of 20–80 s. These synthetics represent the total wavefield $u=u_0+\delta u$. Upon inversion, we seek to infer from δu the elasticity perturbations δc relative to a smooth reference model c_0 (associated with u_0) which, as mentioned above, is obtained from *ak135* by smoothing the step-wise velocity increases over a broad depth range.

With another type of test we demonstrate that the GRT can resolve structure at scales smaller than the Fresnel zones of the associated scattered waves. For this purpose we follow *Shearer et al.* (1999) and invert data generated (using the Born approximation) for interfaces with topography and gaps.

2.4.1 Image gathers

We first use WKBJ synthetics to see how interfaces at 410 and 660 km appear in the image gathers. Synthetics are computed for *ak135* (that is, with step increases in shear wavespeed at 410 and 660 km depth, but no contrast near 520 km). The GRT seeks to locate perturbations with respect to the smooth back ground. This test would be considered successful if the GRT yields contrasts near 410 km and 660 km (and nowhere else).

Using (4) we form image gathers $I(\mathbf{y};\theta,\psi)$ for image points $\mathbf{y}$ at 5 km depth intervals along 1-D (radial) profiles from Earth's surface to 1000 km depth – note the amplification (by factor of 4) for depths larger than 100 km. Integration over scattering azimuth ψ and combining the results in bins of scattering angle θ yields a series of common image point gathers spanning the whole range of θ but with varying sensitivity to structure at different depths (Figure 2-5). The latter is a manifestation of "spatial resolution drift" (see note at the end of section 2.2): shallow interfaces appear for scatter angles $39^\circ<\theta<60^\circ$, the '410' discontinuity appears at $60^\circ<\theta<90^\circ$, and scatter angles between 70-105° reveal the '660'. Integration over all θ reveals structure along the entire vertical profile (Figure 2-5, trace on the right). This GRT image shows peaks at the correct depths of 0, 410 and 660 km, and we note the absence of reflectivity contrast at depths other than 410 and 660 km. The amplitude of the peaks at 410 and 660 are comparable, and the widths are about 50 km (slightly more for 660 than the 410 because of the scatter angles generally being larger) which is consistent with the frequencies used. We have verified that peak location and width are insensitive to the (smooth) background velocity model.

2.4.2 Effects of noise, phase conversions, depth phases, or multiple scattering

With similar experiments we examined the effects on the image gathers of noise or the presence of *P*-to-*S* conversions, depth phases, or multiple reverberations. We first ran the GRT on WKBJ synthetics

that include white stationary noise, with signal-to-noise ratios between 1/20 and 1/100 for both $S_{410}S$ $S_{660}S$ and 1/5 for *SS* proper. Even though the precursors cannot be identified in the raw data, the GRT image gathers reveal the contrasts at 410 and 660 km well above the noise level (Figure 2-6a). Figure suggests that *PS* waves can arrive close to the *SS* precursors. Likewise, depth phases from deep earthquakes and multiple reflections of and reverberations between transition zone discontinuities can interfere with the *SS* precursors (e.g., *Schmerr and Garnero, 2006*). Applying the GRT to synthetic wavefields containing such signals demonstrates that such interfering waves do not, in general, contaminate the images of the '410' and '660' (Figures 2.6b-d). Converted phases such as *PS* and multiple reverberations can form prominent arrivals but the difference in slowness is sufficient to suppress them upon transformation (Figures 2.6b, d). Depth phases could contaminate the image if events occurred in a small depth range, but for the (realistic) depth distributions considered here the depth phases do not produce spurious 'events' in the image gathers. However, they can produce small phase shifts (pulse distortions) (Figure 2-6c). From these and other tests we conclude that seismic phases other than *SS* and its precursors do not produce major artifacts. [Caveat: since WKBJ only contain user-specified dynamic wave groups we cannot rule out the possibility that there are interfering phases that could produce imaging artifacts – more comprehensive tests require full wave synthetics, for instance from mode summation or reflectivity method.]

2.4.3 Lateral resolution

To test lateral resolution, and demonstrate that inverse scattering can resolve structure at length scales smaller than the Fresnel zone of the scattered waves, we use the GRT in a synthetic example similar to the one used in *Shearer et al.* (1999). The model (lower right corner of Figure 2-7) consists of a reflector east of 196°E, a flat 410-km discontinuity with a 4° wide gap near 192°E, and an undulating

660-km discontinuity with a strong topographic gradient around 195°E and a smooth change in depth of 210°E. The 2-D interfaces vary with longitude and are invariant in latitude. Using the Born approximation, and with fixed source-time function, synthetic data is generated with the real source and receiver distribution. The effective band-width of the scattered data is ~20 s, and the lateral extent of associated Fresnel zone would be of the order of 1000 km. The result of inverse scattering with our is shown in the main panel of Figure 2-7. Despite some smearing effects, the major features of the '220', the gap in the '410', and the topography of of the '660') are well resolved.

2.5. Preliminary images of the transition zone beneath the Northwest Pacific

The ~50,000 records displayed in Figure 2-4 are used for 3-D GRT imaging of the transition zone beneath the Northwest Pacific (Figure 2-2a). First, we examine the GRT image at (35°N, 175 °E). Subsequently, 21 such radial reflectivity profiles are juxtaposed to form a 2-D, north-south seismic section from (25°N, 175 °E) to (45°N, 175 °E) (Figure 2-8). We recall that for the inversion of real data we correct the travel times for 3-D mantle heterogeneity using the tomographic model due to *Grand* (2002). The effect on the images is small, and the results do not depend strongly on the choice of model, but we note that subtle pulse complexities may be introduced (or removed) when using (different) 3-D mantle models. Figure 2-9 displays the angle gather and resulting GRT image for a location with coordinates (35°N, 175 °E). The radial images as a function of scattering angle θ (traces on the left) are produced by integration (for fixed θ) over scattering azimuth ψ. The number of data samples used to calculate the traces at specific θ, plotted above the angle gather, is fairly constant over the range of scatter angle used. For narrow ranges of θ the angle gathers reveal structure in a limited depth range, as discussed above, but integration over θ yields a GRT image that reveals multiple peaks, including contrasts near 410, 520, and 660 km depth (Figure 2-9, trace on the right). There is also signal above 410 km and below 660 km

depth, but in isolated profiles the robustness and significance of such signals are not easily evaluated. Next, we create angle gathers and GRT reflectivity profiles for points 1° apart along the north-south line depicted in Figure 2-8, and lateral juxtaposition of them creates a 2-D seismic section from the surface 1000 kilometers in depth (Figures 2.10, 2.11). For display purposes, and to highlight deeper structures, the near-surface signal has been muted in the images.

In Figure 2-10a we display the radial GRT profiles for data filtered between 20-50 s superimposed on the tomographically inferred lateral variations in shear wavespeed (*Grand, 2002*) that are used to construct the image. The other panels of Figure 2-10 display the GRT images computed from data with a decreasing short-period band lower limit (10, 5, and 2 s, respectively). In Figure 2-11 we display for the same four bandwidths the seismic sections after lateral interpolation between the radial profiles. At all frequencies, and along the entire 2-D section, the data yield large-amplitude, laterally continuous and uniform signals near 415 and 665 km depth. A weaker, but laterally continuous signal appears near 520 km, but its appearance changes considerably with frequency. Hereinafter we refer to these reflectors as the '410', '660', and '520'. The images also reveal scatter zones in the upper mantle (that is, less than 410 km depth) and in the shallow part of the lower mantle between 800-1000 km depth, but their strength and depth vary considerably.

Figure 2-12 shows *SS* stacks at three positions along the section line shown in Figure 2-7 (*personal communication, A. Deuss, 2008*). On the right-hand-side we plot the average reflectivity along the entire section presented – this trace represents the stack of all 21 GRT images (reflectivity profiles) shown in Figure 2-10b. The excellent agreement suggests that on a lateral scale of the order of 1000 km, and for relatively low frequencies, the GRT images are in excellent agreement with those produced by common mid-point stacking.

For all frequency bands considered, the '410' and '660' discontinuities are prominent features in seismic sections. In the low frequency band, 20-50 s (Figures 2.10a, 2.11a), the appearance of the '410'

and '660' along the section is remarkably stable. The '660' appears somewhat wider than the '410' but part of this reflects the above mentioned decrease in radial resolution due to the fact that the deeper structures are constrained by larger scattering angles opening angles – indeed, this effect was also apparent in the synthetic tests (e.g., Figure 2-5). At these frequencies the images reveal no significant topography on either the '410' or the '660'. With increasing frequency band the '410' and '660' remain stable but slight lateral variation in depth becomes apparent and the pulse shapes begin to reveal subtle complexity. For example, the pulse width and amplitude vary slightly along the line of section, and at some latitudes the pulses that delineate the '660' become more asymmetric (locally the '660' may even appear split). However, such subtle variations are probably within the uncertainty caused by 3-D mantle heterogeneity and should interpreted considerable restraint. We observe that with increasing frequencies, the amplitude of the '410' decreases slightly compared to that of the '660'.

The '520' appears prominently in this region, especially at the lowest frequencies considered here. At periods between 20-50 s (Figures 2.10a, 2.11a) it forms a laterally continuous scatter zone that is substantially weaker and broader than both the '410' and the '660'. For periods longer than 10 s the shows prominently both in our GRT images and in the common midpoint stacks for the same region (Figure 2-12). When progressively higher frequencies are admitted, the structure of the reflectivity zone becomes increasingly complex and incoherent. At periods less than 10 s splitting of the '520' is (Figures 2.10b-d). This change in character is readily visible in the seismic sections displayed in 2.11b, c. Around 39°N, for example, the data suggest the presence of multiple (weak) elasticity and the different branches of the '520' form a complex pattern between 500 and 550 km depth (Figures 2.11c,d). The absence of comparable complexity in the '410' and '660', and the fact that the change in pulse shape with frequency is larger than the effects we have seen from 3-D mantle heterogeneity, suggests that the structural complexity and frequency dependence of the '520' is real and neither caused by local changes in data coverage or quality nor due to mantle structure that is not well represented by

tomographic model used. At low frequencies, the depth to the '520' varies smoothly along the profile the topography is positively correlated with the '410'. The topography is larger in the 10-50 s band, and short periods the '520' is too incoherent to give a meaningful estimate of topography.

In addition to the unequivocal interfaces near (on average) 415 and 665 km depth and a complex (frequency dependent) scatter zone around 520 km depth, the GRT images reveal significant structure between 200-300 km depth and between 800-1000 km depth. At the longest periods considered here (20-50 s) these signals could reasonably be dismissed as side lobes of the $S_{410}S$ and $S_{660}S$ (Figures 2.10a, 11a), but increasing the bandwidth demonstrates that they are distinct, unambiguous, albeit weak and perhaps laterally discontinuous structures. We also stress that the inversion of data computed for a model with only the '410' and '660' (Figure 2-5) did not produce artifacts near 300, 520, or 800 km depth. Furthermore, in the 20-50 s and 10-50 s windows the topography of the event around '300' does not correlate with that of the '410', which also suggests that they are not related to one another in a simple way.

2.6 Discussion

2.6.1 Transition zone imaging with the generalized Radon transform

The results of the resolution tests with synthetic data, the robustness of inversions of recorded data, and the excellent agreement (evaluated at the appropriate scale) between the seismic sections presented and results of conventional common midpoint stacking, demonstrate that transition zone imaging with the generalized Radon transform of the *SS* wavefield is feasible, at least in regions of dense data coverage such as the northern and northwestern part of the Pacific. A decade ago, *Shearer et al.* (1999) already demonstrated with synthetic data the promise of migration techniques for the imaging of transition zone discontinuities, but with the then available data coverage it did not appear possible to obtain results

better than common midpoint stacking. To a large extent, the success of GRT imaging reported here can probably be attributed to access to vastly more data, but there are also subtle – but important – technical aspects of the methodology that help produce high-resolution images.

An important aspect of the GRT, as presented in this paper, is that it fully exploits the redundancy in the data and is not restricted to "common-offset" subsets of the data. The GRT constructs multiple images of a given image point for varying scattering angles and azimuths, and the final image for that location is then obtained by integrating (stacking) over these angles. This way of using data redundancy (that is, stacking over angle for a fixed image point versus stacking of waveforms over spatial bins) is a fundamental difference between the GRT used here and methods involving stacking over spatial bins, such as common-offset Kirchoff migration.

The approach described by *Shearer et al.* (1999) and the GRT presented here both solve an underdetermined (linearized) inverse problem. In the GRT the least squares inversion is implicit through the inclusion of the approximate inverse of the normal operator F^*F, see equation (3). In the full implementation of the GRT, the normal operator controls the sensitivity along the isochrons by accounting for the radiation patterns (focal mechanisms and contrast source), geometrical spreading, and illumination. [We note that in our implementation we do not include all weights – see remark below (4).] Instead of Tikhonov regularization in the model space (which decreases spatial resolution), the GRT attributes sensitivity in accordance with the Fresnel zones of the relevant scattered phases by limiting the range of integration over migration dips, which is controlled by the available data. Applied to unevenly sampled data, the GRT accumulates the contributions from the corresponding sensitivity kernels weighted with available data samples. This localization of sensitivity, akin to the use of finite frequency sensitivity kernels in transmission or reflection tomography, reduces the need for regularization (spatial averaging) and preserves lateral resolution where illumination is sufficient.

Adequate localization of sensitivity requires data from a broad distance and azimuth range (*Stolk*

and De Hoop, 2002), and in regions with poor data coverage (in terms of the range of scattering angles and azimuths) application of the GRT as presented here may produce imaging artifacts. In such regions may still be possible to constrain some aspects of sub-surface scatters if one can achieve even better localization than is possible with the traditional GRT. The optimal way to implement such partial reconstruction with the GRT, in multi-scale sense, makes use of wave packets and localization in phase space (*De Hoop et al., 2009*), and this is a topic of further research.

2.6.2 Transition zone structure and mineralogy

The region studied here is far away from the northwestern Pacific subduction zones and the presumed mantle upwelling beneath Hawaii. The 2-D section crosses the Hawaii-Emperor seamount chain (around 30°N). Inverse scattering of *SS* data can in principle resolve topography at a lateral resolution of a few 100 km (Figure 2-7), which is up to an order of magnitude smaller than obtained by traditional stacking of long period *SS* data, but in this part of the tectonically stable Pacific the topography is (as expected) small and will, therefore, not be a topic of discussion here.

The data resolve scatter zones at several depths beneath the study region. The most pronounced and robust reflectors appear around 410 and 660 km depth, but the images also suggest elasticity contrasts around 300 km depth, between 500-560 km (especially at longer periods), and between 800-1000 km. The presence of interfaces near 410, 500-560, and 660 km depth is generally consistent with expectations from olivine mineralogy (Figure 2-1). Scattering near 300 km and between 800 and 1000 km depth occurs outside the pressure/depth range associated with the transitions in the olivine system (which mark the transition zone *senso stricto*) and may be related to pyroxene and garnet transitions.

The depth to the '410' (averaged along the profile) is 415 km, and the '660' occurs around 665 km depth. At a wavespeed of 5 km/s the uncertainty in depth is about 5 km at the short period range of the

data used here, and inaccuracies in the background wavespeed of the order of 1% would add (at most) another 5 km to this uncertainty. With these estimates of uncertainty, the '410' and '660' are imaged approximately at their global average depths, and both the variation in depth along the line of section the minor distortions of the pulses associated with the '410' and '660' km discontinuities are probably insignificant. The observation that with increasing frequencies the amplitude of the '410' decreases slightly compared to that of the '660' suggests that in this region the post-spinel (ringwoodite to perovskite and ferropericlase) transition (associated with the '660') is sharper than the olivine to wadsleyite transition (associated with the '410'). This is consistent with mineral physics studies that suggest that the olivine to wadsleyite transition occurs over a broader depth range (6-19 km) than the post-spinel transition (1-10 km) (*Bina and Wood, 1987; Irifune and Isshiki, 1998; Ito and Takahashi, 1989; Katsura and Ito, 1989; Akaogi and Navrotsky, 1989*).

The images reveal substantial scattering from depths in between the '410' and '660' interfaces. This depth range is consistent with the wadsleyite to ringwoodite transition, which previous seismological studies have referred to as the '520' discontinuity (e.g, *Shearer and Masters, 1992; Deuss and Woodhouse, 2001; Deuss, 2009*). For data with periods larger than 15 s our images reveal a single broad event between 500 and 560 km depth (e.g., Figure 2-11a). With increasing frequency the signal becomes weaker and increasingly less coherent, with (multiple) splitting observed in the GRT images at 5-50 s and 2-50 s (Figures 2.10c,d and 2.11c,d). This complexity is not seen in the '410' and '660' and cannot (in a trivial way) be attributed to deterioration of data coverage at these periods. These observations suggest that the frequency dependence of the '520' is real.

Deuss and Woodhouse (2001) observe reflections near 500-515 km and 551-566 km in some of Pacific, near the Indonesian subduction zone, and beneath the North African shield. They attribute splitting to the phase transitions in non-olivine (e.g., pyroxene, garnet) components. *Saikia et al.* (2008) proposed that the shallower discontinuity is due to the wadsleyite to ringwoodite transformation

the deeper one represents the formation of $CaSiO_3$ perovskite from garnet. In a fertile mantle – or in a mantle with a substantial component of recycled MORB crust, which contains more Ca than normal mantle – these two discontinuities would be separated. The regional variation of the character of the has thus been invoked as evidence for large-scale chemical heterogeneity.

Alternatively, the predominance of the '520' at low frequencies and its gradual break-down with increasing frequencies of the data used may – to first order – be explained by the broad two-phase loop of the divariant transition from wadsleyite to ringwoodite (*Shearer, 1996; Rigden et al., 1991; Frost et al., 2003*). In peridotite mantle this transformation is found to take place over a pressure interval corresponding to ~20 km at 1400°C even when buffering by garnet is considered. *Frost et al.* (2003) also showed that the phase-fraction profile is almost linear across the transformation, which would explain why its image is more pronounced for low frequency data. It is possible that the structure at short periods reflect transitions in the non-olivine components that become visible only when, with increasing data frequency, the image of the wadsleyite to ringwoodite transition weakens. We note, however, that this weak signal may not exceed the noise level (and its variability is within the uncertainty due to wavespeed variations that are not accounted for in the global tomography model that we use to make travel time corrections).

We have as yet no definitive explanation for the scattering that is visible near 300 km depth 2.10a,b and 2.11a,b). One possible cause is the transition in pyroxene from an orthorhombic to a monoclinic structure (*Woodland and Angel, 1997; Stixrude and Lithgow-Bertelloni, 2005*). For a mantle composition the effect of this transition on elasticity would be small but in material with higher concentrations of ortho-pyroxene, such as harzburgite, the change could be substantial. If this interpretation is correct, our results imply that even far away from zones of present-day subduction the upper mantle could contain significant fractions of harzburgite. *Williams and Revenaugh* (2005) proposed that a discontinuity at around 300 km might be generated by SiO_2-stishovite formation in

eclogitic assemblages. This explanation would imply widespread occurrence of materials with mid-oceanic-ridge basalt chemistry. Finally, the '300' could signify the base of a zone of carbonatite melting in the asthenosphere (*J.-P. Morgan, personal communication, 2009*).

These are exciting possibilities, both with far reaching implications for our understanding of mantle flow and mixing. We are hesitant, however, to push the interpretation of the observation of scattering near 300 km depth beyond these speculations and defer further discussion to a later time when robust evidence is available for a larger geographical region. Yet we note that most of the above explanations require a chemistry that is distinct from a pyrolitic composition, which may suggest significant compositional heterogeneity in a region is (at present day) far away from active subduction systems.

2.7 Conclusions

We have developed a generalized Radon transform to construct the images of mantle transition zone with the broadband wavefield of *SS* and its precursors. The GRT is a technique for inverse scattering and it exploits the redundancy in the data in that for a range of scattering angle and azimuth it creates multiple images of a single point. Combined, these common image point gathers represent a GRT image (i.e., the radial reflectivity profile) which reveals the position of scatterers as a function of geographic location and depth beneath the surface. The main objective of this paper was to demonstrate the feasibility of high resolution imaging of the transition zone beneath geographic regions (such as oceans) far away from sources and receivers. In future studies this new capability will be used for high resolution studies of the transition zone beneath, for instance, Hawaii.

The GRT images of the transition zone beneath the north Pacific reveal a pronounced '410' and for all frequencies considered. For periods $T > 10$ s our results are consistent with that of conventional stacking. With increasing frequency there is a slight increase in structural complexity and depth

and a strengthening of the '660' compared to the '410' (which may indicate that the former is sharper than the latter). The average depths to the '410' and '660' are 415±5 and 665±7 km, respectively, and small (~10 km peak-to-peak) depth variation is insignificant given the depth resolution of the data. The '520' is pronounced in the low frequency band, and broader and weaker than either the '410' or '660', there is an increase in the complexity of the '520' with increasing frequency, even when the '410' and '660' are not similarly affected. The frequency dependence of the '520' is consistent with the broad two-phase loop of the wadsleyite to ringwoodite transition, but structure that becomes visible at short periods may reflect transitions in non-olivine components.

In addition to the usual suspects (that is, the '410', '520', and '660'), the transition zone images also reveal substantial scattering from structures at around 300 km depth and between 800 and 1000 km depth. The prominence of the event near 300 km could indicate the presence of harzburgite or MORB material far away from sites of active subduction. These structures may be laterally intermittent, however, and larger scale imaging is needed to establish the geographical distribution and lateral continuity of these structures.

The vast and rapidly growing amount of high quality waveform data that is available through IRIS DMC has begun to allow large scale exploration seismology of the deep mantle. Following our studies of the lowermost mantle with inverse scattering of the *ScS* and *SKKS* wavefields (*Wang et al., 2006, 2008; Van der Hilst et al., 2007*) we have demonstrated here the feasibility of transition zone imaging with the *SS* wavefield. This is opening exciting new possibilities for collaborative studies of Earth's deep interior in general and for detailed investigations of the upper mantle transition zone, in particular.

Acknowledgments:

We thank Jason Phipps Morgan and Greg Hirth for stimulating discussions and excellent suggestions various aspects of our work, and we are grateful to Arwen Deuss for computing the *SS* stacks shown in

Figure 2-12. We thank Rosalee Lamm (MSc, MIT) for her contribution to the early stages of this The revision of the original manuscript benefited greatly from insightful comments by Peter Shearer, an anonymous reviewer, and the Editor (George Helffrich). This research has been supported by the program of the US National Science Foundation under grant EAR-0757871 and would not have been possible without the open availability of waveform data through the Data Management Center of the Incorporated Research Institutions for Seismology (IRIS).

References Cited

Akaogi, M., Ito, E., and Navrotsky, A., 1989. Olivine-modified spinelspinel transitions in the system Mg_2SiO_4-Fe_2SiO_4: calorimetric measurements, thermochemical calculations, and geophysical application. *J Geophys Res.* 94: 15,671–15,685.

An, Y., Gu, Y. J. and Sacchi, M. D., 2007. Imaging mantle discontinuities using least squares Radon transform. *J. Geophys. Res.*, 112, B10303, doi:10.1029/2007JB005009.

Beylkin, G., 1985. Imaging of discontinuities in the inverse scattering problem by inversion of a causal generalized Radon transform. *J. Math. Phys.*. 26, 99–108.

Bina, C.R., and Wood, B. J., 1987. The olivine-spinel transitions: experirnental and thermodynamic. constraints and implications for the nature of the 400 km seismic discontinuity. *J . Geophys. Res.*, 92, 4853-4866.

Bina, C. R. and Helffrich, G., 1994. Phase transition Clapeyron slopes and transition zone seismic discontinuity topography. *J. Geophys. Res.*, 99(B8), 15,853–15,860.

Brandsberg-Dahl, S., de Hoop, M. V., and Ursin, B., 2003. Focusing in dip and AVA compensation on scattering-angle/azimuth common image gathers. *Geophysics*, 68, 232-254.

Burridge, R., de Hoop, M. V., Miller, D., and Spencer, C., 1998. Multiparameter inversion in anisotropic media. *Geophys. J. Int.*, 134, 757-777.

Castle, J.C. and Creager, K.C., 2000. Local sharpness and shear wave speed jump across the 660-km discontinuity. *J. Geophys. Res.* 105, 6191–6200.

Chaljub, E., and Tarantola, A., 1997. Sensitivity of SS precursors to topography on the upper mantle 660-km discontinuity. *Geophys. Res. Lett.* 24, 2613–2616.

Chambers, K., Woodhouse, J. H., and Deuss, A., 2005a. Reflectivity of the 410-km discontinuity from PP and SS precursors. *J. Geophys. Res.* 110(B02301), doi:10.1029/2004JB003345.

Chambers, K., Woodhouse, J. H., and Deuss, A., 2005b. Topography of the 410-km discontinuity from PP and SS precursors. *Earth Planet. Sci. Lett.* 235, 610–622.

Chambers, K., and Woodhouse, J. H., 2006. Investigating the lowermost mantle using migrations of long-period S-ScS data. *Geophys. J. Int.*, 166, 667-678.

Chapman, C. H., 1978. New method for computing synthetic seismograms. *Geophys. J. Int.*, 54, 481-518.

Collier, J., and Helffrich, G. 1997. Topography of the "410" and "660" km seismic discontinuities in the Izu-Bonin subduction zone. *Geophys. Res. Lett.*, v.24, 1535-1538.

Dahlen, F. A., Hungh, S.-H., and Nolet, G., 2000. Fréchet kernels for finite-frequency traveltimes—I. Theory. *Geophys. J. Int.*, 141, 175-203.

Dahlen, F. A., 2005. Finite-frequency sensitivity kernels for boundary topography perturbations. *Geophys. J. Int.*, 162, 525-540.

De Hoop, M. V., Burridge, R., Spencer, C., and Miller, D., 1994. Generalized Radon transform amplitude versus angle (GRT/AVA) migration/inversion in anisotropic media. *Proc SPIE* 2301, 15-27.

De Hoop, M. V., and Bleistein, N., 1997. Generalized Radon transform inversions for reflectivity in anisotropic elastic media. *Inverse Problems*, 13, 669-690.

De Hoop, M.V., and Van der Hilst, R.D., 2005. On sensitivity kernels for wave equation transmission tomography. *Geophysical Journal International*, v. 160, DOI: 10.1111/j.1365-246X.2004.02509.

De Hoop, M.V., Van der Hilst, R.D., and P. Shen, 2006. Wave-equation reflection tomography: annihilators and sensitivity kernels. *Geophysical Journal International*, vol. 167, p. 1332-1352.

De Hoop, M.V., Smith, H., Uhlmann, G, and Van der Hilst, R.D., 2009. Seismic imaging with the generalized Radon transform: A curvelet transform perspective. *Inverse Problems*, v. 25, 025005 (21pp), doi: 10.1088/0266-5611/25/2/025005.

Deuss, A., and Woodhouse, J. H., 2001. Seismic observations of splitting of the mid-transition zone discontinuity in earth's mantle. *Science*, 294, 354–357.

Deuss, A., 2009. Global Observations of Mantle Discontinuities Using *SS* and *PP* Precursors. *Surveys in Geophysics*, Volume 30, Issue 4-5, 301-326.

Deuss, A., Redfern, S. A. T., Chambers, K., and Woodhouse, J. H., 2006. The nature of the 660-kilometer discontinuity in Earth's mantle from global seismic observations of PP precursors. *Science*, 311, 198–201.

Engdahl, E. R. Van der Hilst, R. D., and Buland, R. P, 1998. Global teleseismic Earthquake relocation from improved travel times and procedures for depth determination. *Bull. Seis. Soc. Am*, 88 (3), 722-743.

Fei, Y., van Orman J., Li, J. van Westrenen W., Sanloup, C., Minarik W., Hirose K., Komabayashi, T., Walter, M., and Funakoshi, K., 2004. Experimentally determined postspinel transformation boundary in Mg_2SiO_4 using MgO as an internal pressure standard and its geophysical implications. *J. Geophys. Res.* 103(B02305), doi:10.1029/2003JB002562.

Flanagan, M.P., and Shearer, P.M., 1998a. Global mapping of topography on transition zone velocity

discontinuities by stacking SS precursors. *J. Geophys. Res.*, 103, 2673–2692.

Flanagan, M.P. and Shearer, P.M., 1998b. Topography on the 410-km seismic velocity discontinuity near subduction zones from stacking of sS, sP, and pP precursors. *J. Geophys. Res.*, 103, pp. 21,165–21,182.

Flanagan, M. P., and Shearer, P. M., 1999. A map of topography on the 410-km discontinuity from PP precursors. *Geophys. Res. Lett.*, 26, 549-552.

Frost, D.J., 2003. The structure and sharpness of $(Mg,Fe)_2SiO_4$ phase transformations in the transition zone. *Earth Planet. Sci. Lett.*, 216, 313–328.

Gossler, J., and Kind, R., 1996. Seismic evidence for very deep roots of continents. *Earth Planet. Sci. Lett.*, 138(1-4), 1 – 13.

Grand, S.P., 2002. Mantle shear-wave tomography and the fate of subducted slabs. *Phil. Trans. R. Soc. London*, A 360, 2475–2491.

Gu, Y.J., Dziewonski, A.M. and Agee, C.B., 1998. Global de-correlation of the topography of transition zone discontinuities. *Earth Planet. Sci. Lett.*, 157, 57–67.

Gu, Y.J., and Dziewonski, A.M., 2002. Global variability of transition zone thickness. *J. Geophys. Res.*, 107(B7), doi:10.1029/2001JB000489.

Gu, Y.J., Dziewoński, A.M., and Ekström, G., 2003. Simultaneous inversion for mantle shear velocity and topography of transition zone discontinuities. *Geophys. J. Int.*, 154, 559–583.

Gu, Y. J. and Sacchi, M., 2009. Radon Transform methods and their applications in mapping mantle reflectivity structure. *Surv. Geophys.*, doi:10.1007/s10712.009-9076-0.

Helffrich, G., 2000. Topography of the transition zone seismic discontinuities. *Reviews of Geophys.*, 38, 141–158.

Houser, C; Masters, G; Flanagan, M, Flanagan, M. and Shearer, P., 2008. Determination and analysis

long-wavelength transition zone structure using SS precursors. *Geophys. J. Int.*, Volume: 174, Issue:1, 178-194.

Irifune, T., and Isshiki, M., 1998. Iron partitioning in a pyrolite mantle and the nature of the 410-km seismic discontinuity. *Nature*, 392, 702-705.

Ito, E., and Takahashi, E., 1989. Postspinel transformations in the system Mg_2SiO_4-Fe•SiO_4 and some geophysicailm plications, *J. Geophys. Res.*, 9, 10,637-10,646.

Jeanloz, R., and Thompson A.B., 1983. Phase transitions and mantle discontinuities. *Rev. Geophys.*, 21, 51-74.

Katsura, T., and Ito, E., 1989. The system Mg_2SiO_4–Fe_2SiO_4 at high pressures and temperatures: precise determination of stabilities of olivine, modified spinel, and spinel. *J. Geophys. Res.*, 94, 15663–15670.

Kennett, B. L. N., Engdahl, E. R., and Buland, R. P., 1995. Constraints on seismic velocities in the Earth from travel times. *Geophys. J. Int.*, 122, 108-124.

Lawrence, J.F., and P. M. Shearer, 2008. Imaging mantle transition zone thickness with SdS-SS finite-frequency sensitivity kernels. *Geophys. J. Int.*, 174, 143-158.

Lebedev, S. and Chevrot, S. and van der Hilst, R. D., 2002. Seismic evidence for olivine phase change at the 410- and 660-kilometer discontinuities. *Science*, 296, 1300–1302.

Lebedev, S., Chevrot, S., and Van der Hilst, R.D., 2003. Correlation between the shear-speed structure and thickness of the mantle transition zone. *Phys. Earth Planet. Int.*, 136, 25–40.

Li, B., and Liebermann, R., 2007. Indoor seismology by probing the Earth's interior by using sound velocity measurements at high pressures and temperatures. *Proc. Natl. Acad. Sci.*, 104, 9145-9150.

Ma, P., Wang, P., Tenorio, L., De Hoop, M.V., and Van der Hilst, R.D., 2007. Imaging of structure at and near the core-mantle boundary using a generalized Radon transform: 2. Statistical inference of singularities. *J. Geophys. Res.*, vol. 112, B08303, doi:10.1029/2006JB004513.

Miller, D., Oristaglio, M., and Beylkin, G, 1987. A new slant on seismic imaging: Migration and integral geometry. *Geophysics*, 52, 943-964.

Neele, F., de Regt, H., and Van Decar, J., 1997. Gross errors in upper-mantle discontinuity topography from underside reflection data. *Geophys. J. Int.*, 129, 194–204.

Ringwood, A.E., 1969. Phase transformations in the mantle. *Earth Planet. Sci. Lett.*, 5, 401–412.

Ringwood, A.E., 1975. *Composition and Petrology of the Earth's Mantle* (McGraw-Hill, New York, 1975).

Ringwood, A.E., 1991. Phase transformations and their bearing on the constitution and dynamics of the mantle. *Geochim. Cosmochim. Acta*, 55, 2083–2110.

Rondenay, S., Bostock, M.G., and Fischer K.M., 2005. Multichannel inversion of scattered teleseismic body waves: practical considerations and applicability, in *Seismic Earth: Array analysis of broadband seismograms, edited by A. Levander and G. Nolet, AGU Geophysical Monograph Series*, 157.

Rost, S. and Thomas, C., 2009. Improving seismic resolution through array processing techniques. *Surveys in Geophysics*, Volume 30, Issue 4-5, pp. 271-299.

Saikia, A., Frost, D. and Rubie, D., 2008. Splitting of the 520-kilometer seismic discontinuity and chemical heterogeneity in the mantle. *Science*, 319, 1515–1518.

Schmerr, N., and Garnero, E., 2006. Investigation of upper mantle discontinuity structure beneath the central Pacific using SS precursors. *J. Geophys. Res.*, 111, B08305, doi:10.1029/2005JB004197.

Shearer, P. M., 1990. Seismic imaging of upper-mantle structure with new evidence for a 520-km discontinuity. *Nature*, 344, 121-126.

Shearer, P.M., 1991. Constraints on upper-mantle discontinuities from observations of long-period reflected and converted phases. *J. Geophys. Res.*, 96, 18,147-18,182.

Shearer, P. M., and Masters, T. G., 1992. Global mapping of topography on the 660-km discontinuity. *Nature*, 355, 791-796.

Shearer, P.M., 1993. Global mapping of upper mantle reflectors from long-period SS precursors. *Geophys. J. Int.*, 115, 878-904.

Shearer, P.M., M.P. Flanagan and M.A.H. Hedlin, 1999. Experiments in migration processing of *SS* precursor data to image upper mantle discontinuity structure. *J. Geophys. Res.*, 104, 7229-7242.

Shearer, P.M., 2000. Upper mantle seismic discontinuities, in: Earth's deep interior: Mineral Physics and tomography from the atomic to the global scale. *Geophys. Monogr.*, 117, 115-131.

Shim, S.-H, Duffy, T. S., and Shen, G, 2001. The post-spinel transformation in Mg_2SiO_4 and its relation to the 660-km seismic discontinuity. *Nature*, 411, 571–574.

Spetzler, J. and Snieder, R., 2004. The Fresnel volume and transmitted waves. *Geophysics*, 69, 653-663.

Stixrude, L. and Lithgow-Bertelloni, C., 2005. Mineralogy and elasticity of the upper mantle: Origin of the low velocity zone. *Journal of Geophysical Research*, vol. 110, B03204, 10.1029/2004JB002965.

Stolk, C. C. and De Hoop, M.V., 2002. Microlocal analysis of seismic inverse scattering in anisotropic, elastic media. *Commun. Pure Appl. Math.*, 55 261–301.

Tromp, J., Tape, C., and Liu, Q., 2005. Seismic tomography, adjoint methods, time reversal, and banana-donut kernels. *Geophys. J. Int.*, 160, 195-216; doi: 10.1111/j.1365-246X.2004.02456.x.

Van der Hilst, R.D., De Hoop. M.V., Wang, S.-H. Shim, L. Tenorio, and P. Ma, 2007. Seismo-stratigraphy and thermal structure of Earth's core-mantle boundary region. *Science*, vol. 315, p. 1813-1817.

Wang, P., de Hoop, M. V., van der Hilst, R. D., Ma, P., and Tenorio, L., 2006. Generalized Radon Transform Imaging of the Core Mantle Boundary: I—Construction of Image Gathers. *J. Geophys. Res.*, 111, B1230, doi:10.1029/2005JB004241.

Wang, P., de Hoop, M.V., and Van der Hilst, R.D., 2008. Imaging of the lowermost mantle (D") and the core-mantle boundary with SKKS coda waves. *Geophysical Journal International*, 175, 103-115.

Weidner, D.J., and Wang, Y.S., 2000. Phase transformations: Implications for mantle structure. In: "Earth's *deep interior*", *Karato et al. (Eds), Am. Geoph. Un., Geophys. Monogr.*, 215-235.

Weidner, D., L. Li, W. Durham, and J. Chen, 2005. High-temperature plasticity measurements using sychrotron X-rays. *High-pressure technology for geophysical applications. J. Chen, et al., Editors.* 2005, ELSEVIER Inc.: San diego. 123-136.

Williams, Q. and Revenaugh, J., 2005. Ancient subduction, mantle eclogite, and the 300 km seismic discontinuity. *Geology*, 33, 1–4.

Woodland, A.B. and Angel, R.J., 1997. Reversal of the orthoferrosilite-high-P clinoferrosilite transition, a phase diagram for FeSiO3 and implications for the mineralogy of the Earth's upper mantle. *European Journal of Mineralogy*, 9, 245–254.

Zhao, L., and Chevrot, S., 2003. SS-wave sensitivity to upper mantle structure: Implications for the mapping of transition zone discontinuity topographies. *Geophys. Res. Lett.*, 30(11), doi: 10.1029/2003GL017223.

Zheng, Y., Lay, T., Flanagan, M. P., and Williams, Q., 2007. Pervasive seismic wave reflectivity and metasomatism of the Tonga mantle wedge. *Science*, 11, 316. no. 5826, 855-859.

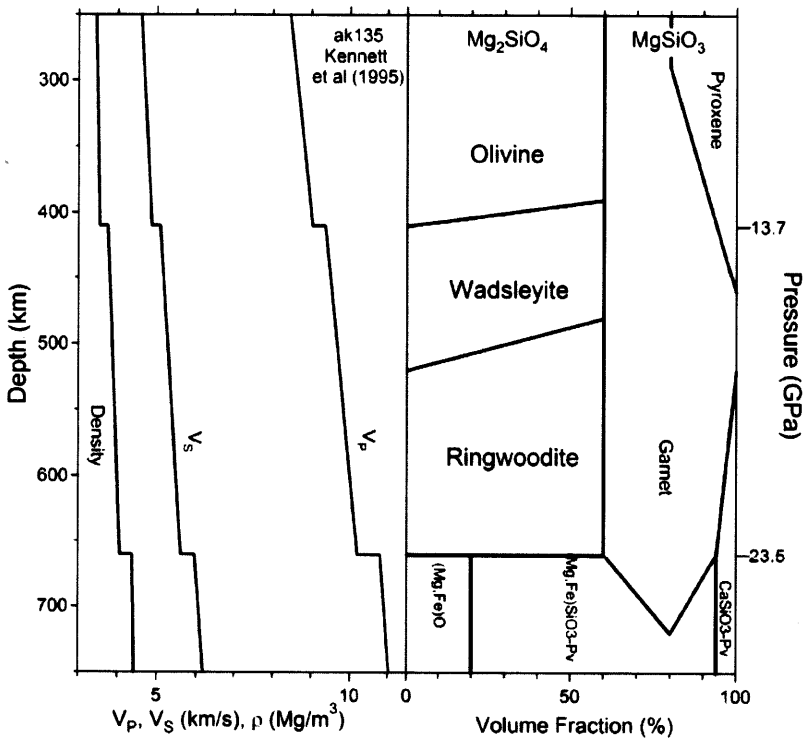

Figure 2-1. (left) *P*- and *S*-wavespeed (and mass density) as function of depth in Earth's mantle between 200 and 800 km depth according to reference Earth model *ak135* (*Kennett et al.*, 1995). (right) Volume fraction of the main mantle constituents in this depth range according the pyrolite model of mantle composition. About 60% of the volume fraction concerns the olivine system, with phase transitions from olivine to wadsleyite near 13.7 GPa (associated with the first order discontinuity in elastic parameters at 410 km in the *ak135* mode), wadsleyite to ringwoodite near 16-18GPa (that is, around 510 km, but notice that there is no corresponding wavespeed or density contrast in the global reference model), and ringwoodite to perovskite and ferropericlase near 23.5 GPa (associated with a change in elastic parameters around 660 km depth). The remaining 40% of the volume fraction mainly concerns silicates in the pyroxene and garnet system.

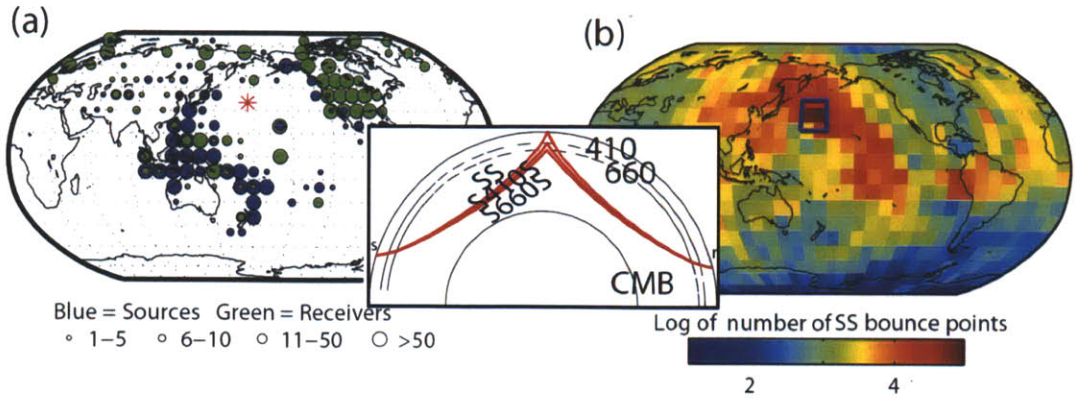

Figure 2-2. (a) Distribution of sources and receivers of the data used in this study. The location of the image gather of Figure 9 is shown by the red asterisk. The size of the blue (green) circle scales with the number of sources (receivers). (b) Global distribution of *SS* bounce points for data with a source-receiver distance of 90°-170°, magnitude above 5.5 and focal depth below 75 km. Sampling density is indicated from red (densest) to blue (least dense). The solid blue rectangle outlines the 20°×20° area in which data is collected. The raypaths of *SS* and its precursors are shown in the middle of the figure. The image point locations, which are near the midpoint of *SS* raypath, are far away from both the sources and receivers.

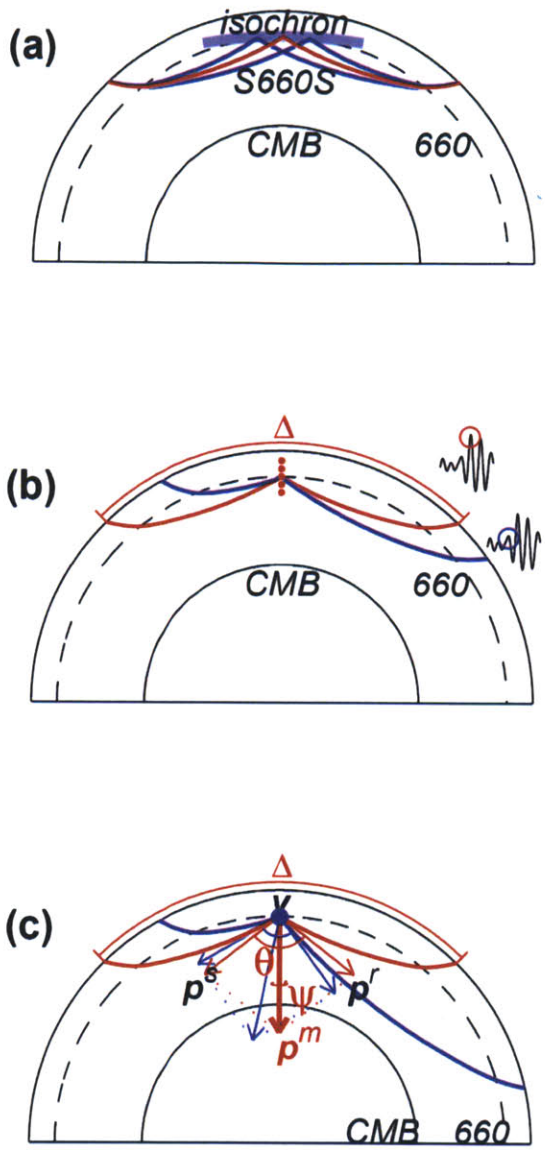

Figure 2-3. Geometry of the GRT. (a) Illustration of an isochron, from which all reflections arrive at the same time. (b) Specular (red) and non-specular (blue) raypaths for a single scattering point. Because *SS* is a mini-max time path, waves that travel non-specular paths may arrive before or after the specular ray. Ray theory uses only specular data (red circle on waveform at right); the full GRT utilizes non-specular energy as well (blue circle). (c) GRT geometry for both specular (red) and non-specular (blue) paths. Unmarked arrows represent slowness vectors p^r and p^s at image point y. Scattering angle θ denotes the angle between the slowness of each leg of the raypath, evaluated at y. The migration dip ν^m describes the isochron normal at y. The scattering azimuth ψ describes the angle between North and the projection of ν^m onto the surface.

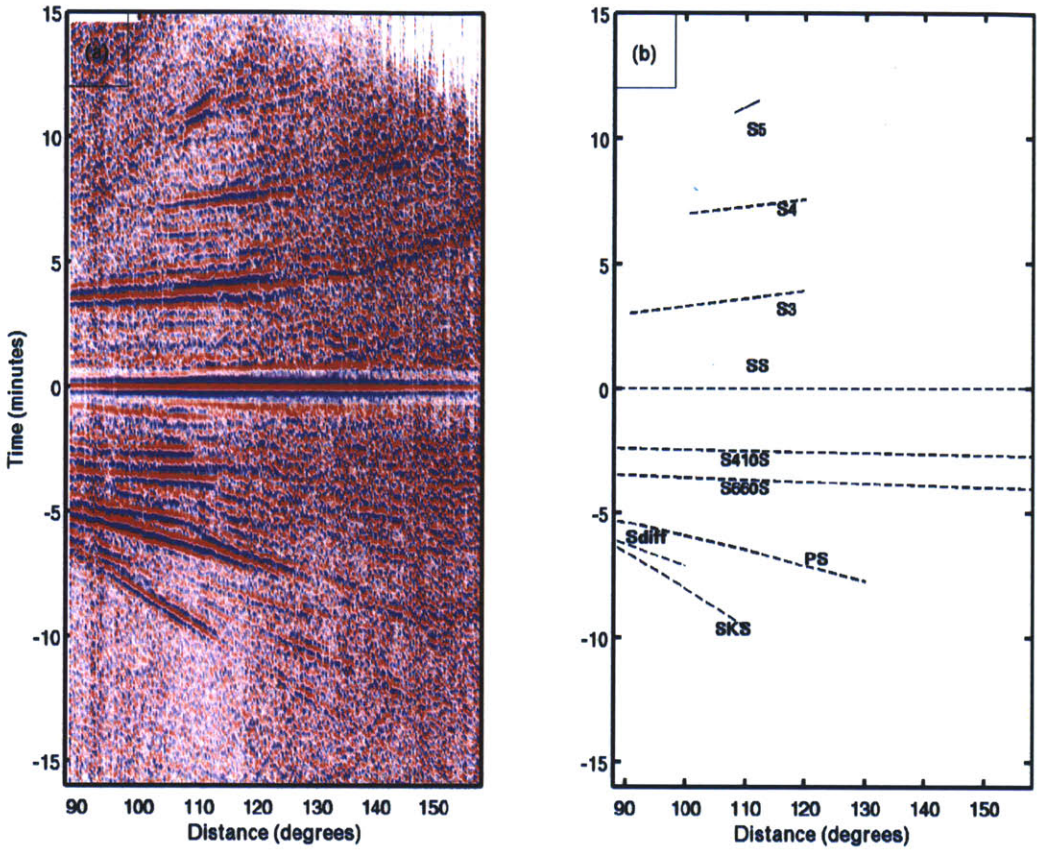

Figure 2-4. (a) Record section of data with reflection points in the study area shown in Figure 2- The stack is relative to the *SS* phase. (b) Corresponding travel time curves (according to *ak135*). We use data beyond 90° (to avoid polarity reversal of *S660S*) up to 170° (to avoid non-specular rays interacting with the outercore). The data has been bandpass filtered between 20-80 s. For this geographic bin (Figure 2), there are relatively few data for epicenter distance larger than 115°; as a result the expression of the precursors is much weaker than in the global stacks (e.g. *Shearer and Masters, 1992*).

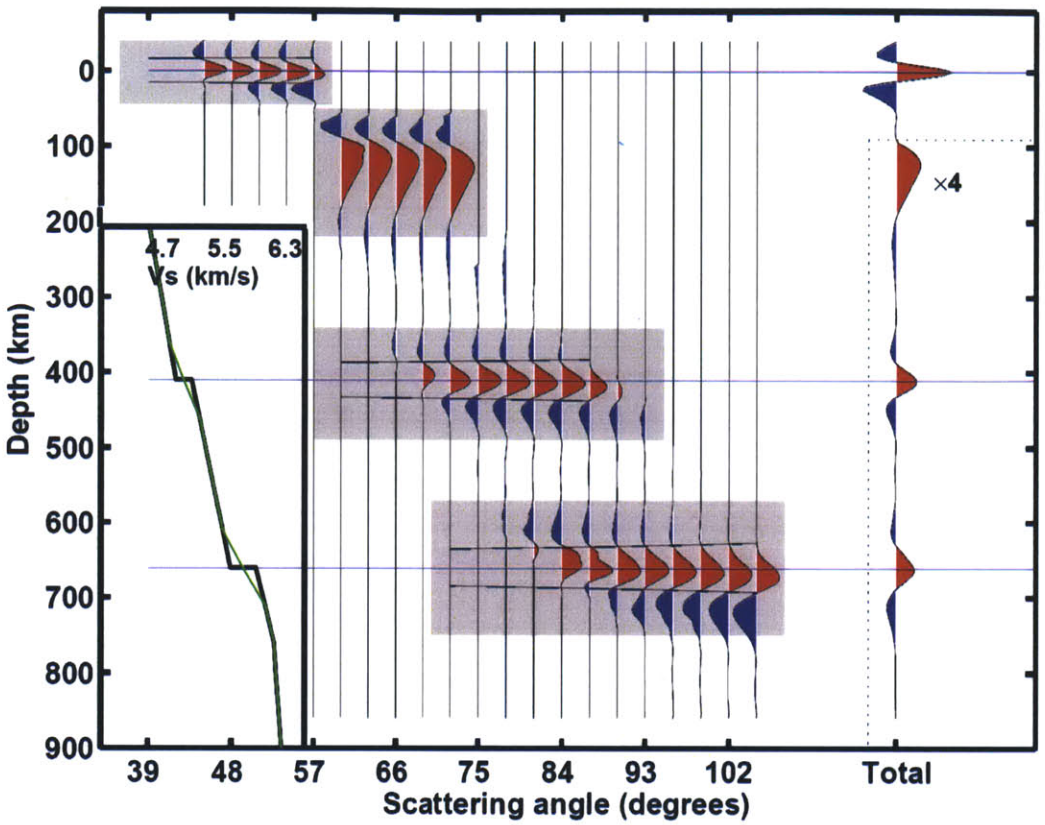

Figure 2-5. GRT applied to synthetic (WKBJ) data with actual source-receiver distribution and focal depth (periods 20-80 s). Traces are normalized so that signal strength cannot be compared across scattering angle. Sidelobes of the surface signal are similar in amplitude to the 410 and 660 signals. The common image gather (right) is amplified (4×) below the dash line. Inset at lower left: The thick dark line represents the original *ak135* velocity model (with first order discontinuities at 410 and 660 km depth, from which the synthetic wavefield is computed; the thin green line represents the smooth model which we used as the background model *c0* for the GRT. (NB because they are replaced by broad gradients, the results do not depend on discontinuity depth and strength of the original *ak135* model.) The structure around 150 km depth is a blow up of one of the sidelobes of the surface reflection *SS*.

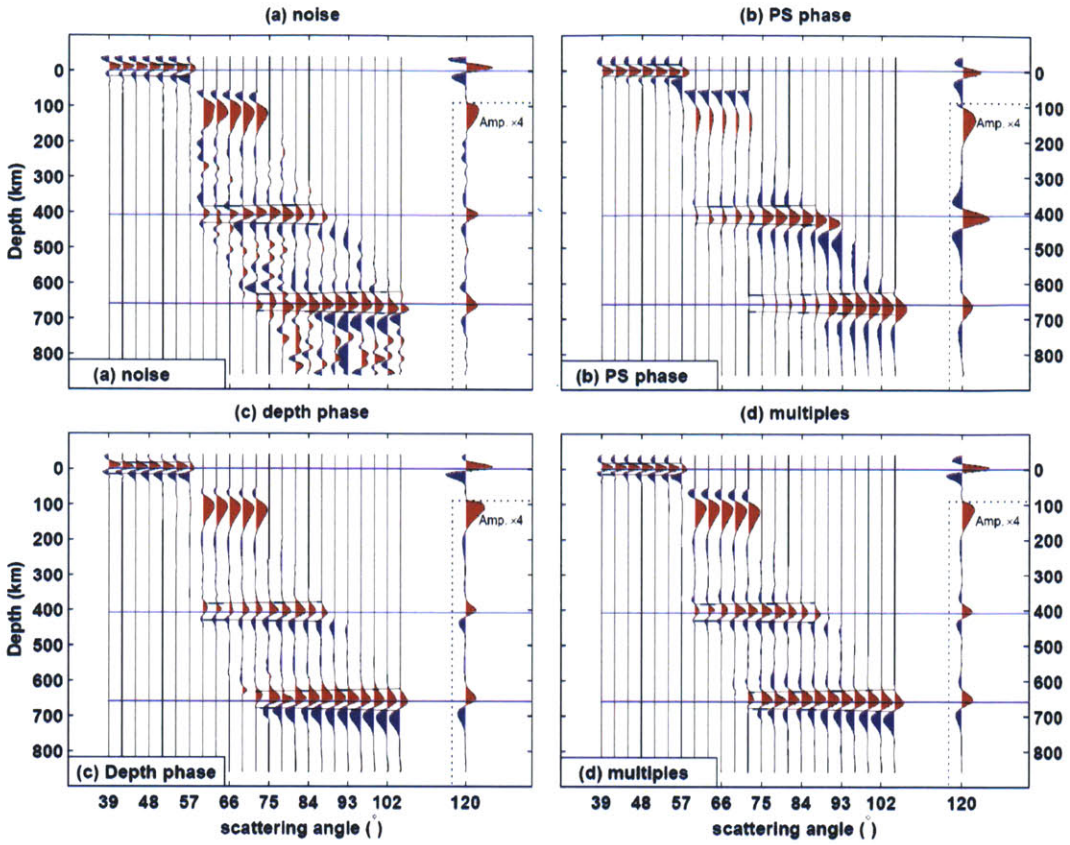

Figure 2-6. Effects on the GRT images of white stationary noise (a), the presence of *P*-to-*S* converted phases (b), presence of depth phases (c), and multiples reverberations between transition zone discontinuities (d). Adding these effects to the synthetics of the *SS*, $S_{410}S$, and $S_{660}S$ has little effect on the GRT image gathers.

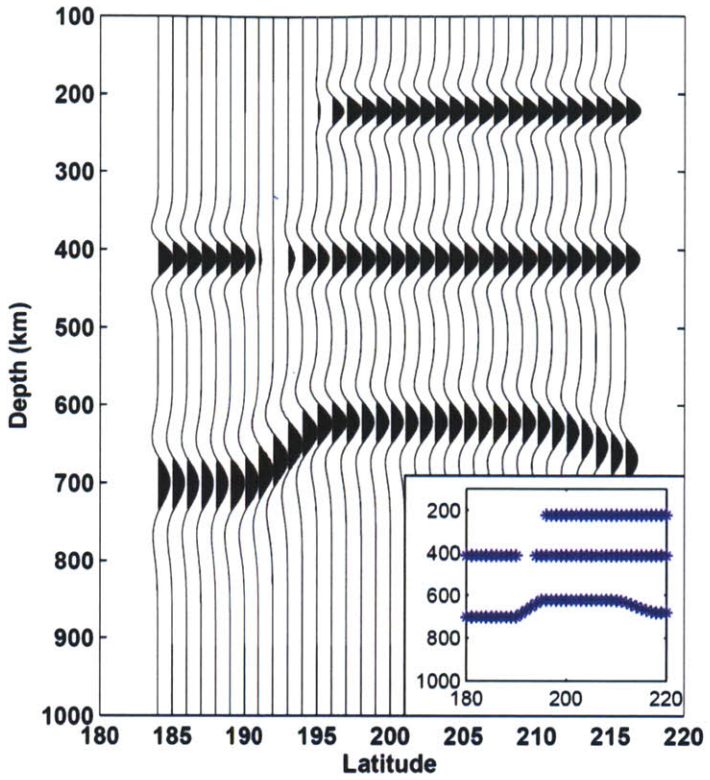

Figure 2-7. Result of inversion with synthetic data to test lateral resolution. The model for which synthetic data is computed (using Born approximation) is plotted in the lower right corner. The input model, which is similar to that used by *Shearer et al.* (1999), consists of a local 220-km reflector, a discontinuous yet flat 410-km discontinuity, and an undulating 660-km discontinuity with both a strong topographic gradient and a smooth change. The GRT result is shown in the main panel. Despite some smearing effects, the major features are well resolved.

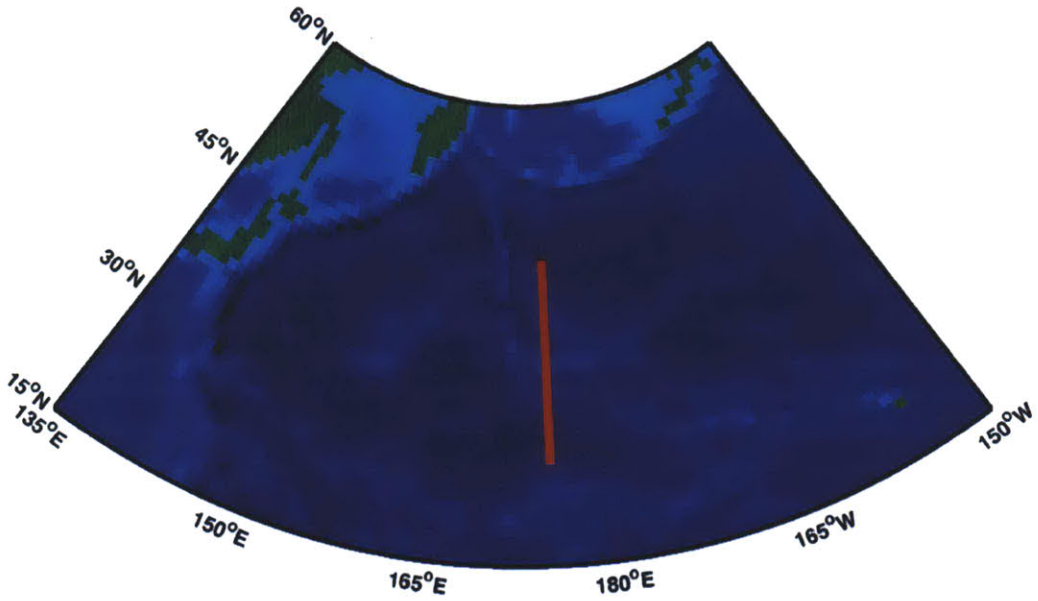

Figure 2-8. The location of the line of section for which images are shown in Figures 10 and 11.

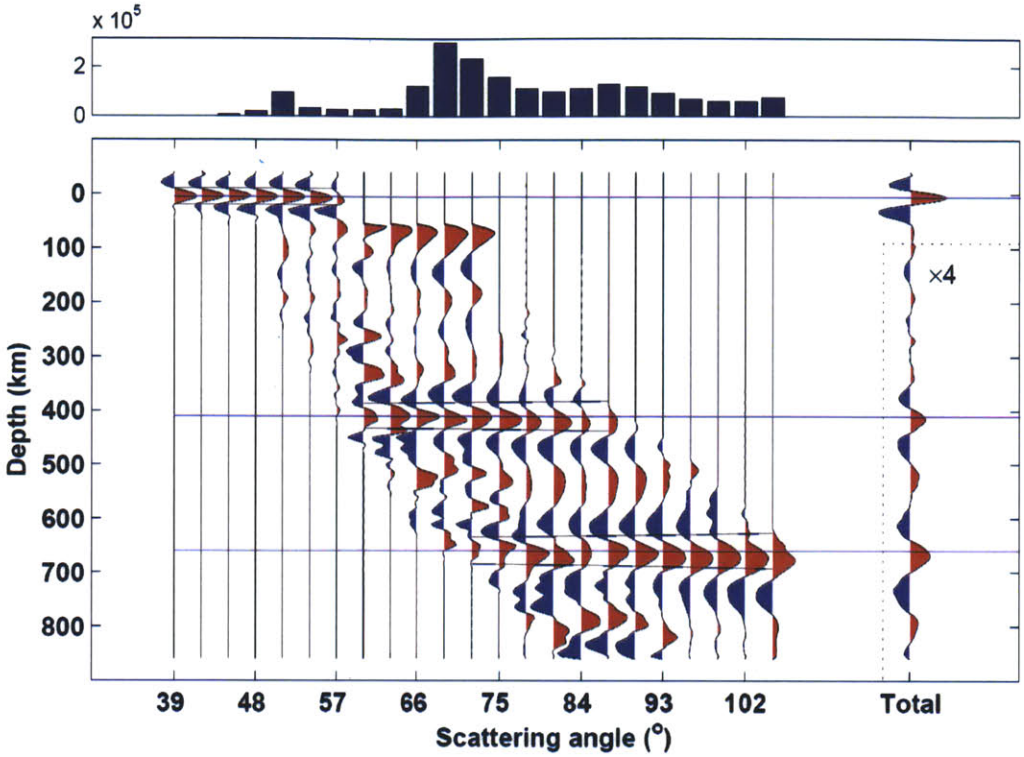

Figure 2-9. Construction of GRT (reflectivity) image (single trace on the right) from 'common image point gathers' for broad-band *SS* data (10-50 s) for a range of opening angles (traces on the left of this panel). The panel above shows the number of data samples used for the computation of the traces at specific θ.

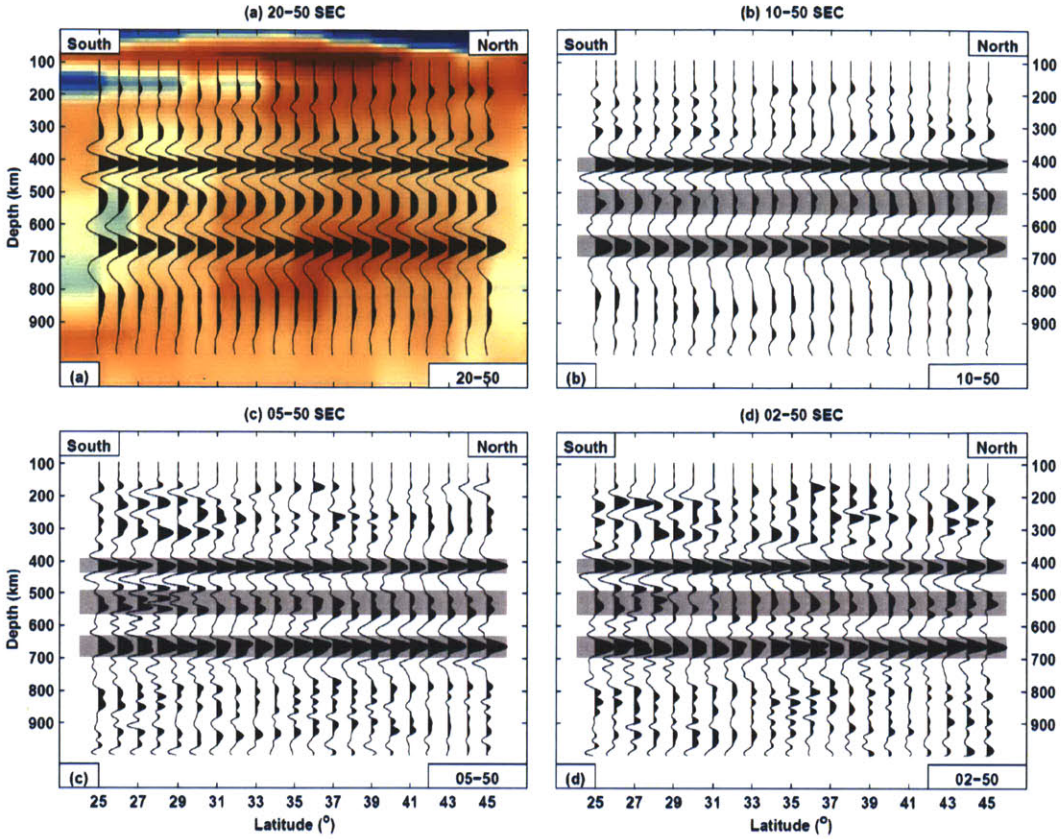

Figure 2-10. Seismic sections of the mantle transition zone in the northern Pacific (see Figure 8 for section location) for different frequencies of the data used. The 2-D section is constructed by lateral juxtaposition of radial reflectivity profiles calculated using equation (5) and the (raw) data associated with the record section in Figure 4, filtered between (a) 20-50 s, (b) 10-50 s, (c) 5-50 s, and (d) 2-50 s. The surface signal is excluded to highlight the weaker structure. Each trace is normalized by its maximum. The '410' and '660' are continuous along the entire length of the section and appear without much change in all the four frequency bandwidths. The '520' is prominent at low frequencies (periods T=20-50 s, panel a) but becomes increasingly more incoherent when shorter period data are included. Background colors in panel (a) depict lateral variations in shear wave speed according to the tomographic model of Grand (2002). In panel (b)-(d) the grey bars indicate the location and width of the pulses associated with the 410, 520 and 660 in the 20-50s period range (panel a).

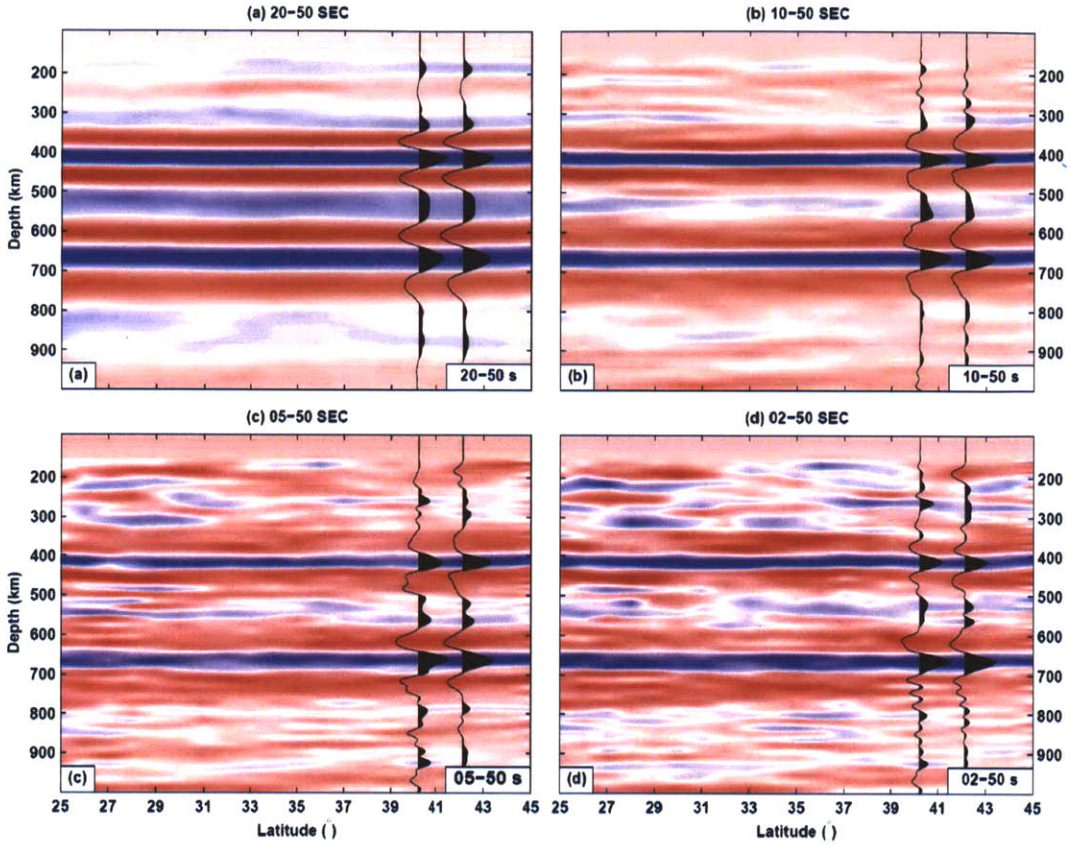

Figure 2-11. Same seismic sections as in Figure 10 but to enhance interfaces (for display purposes only) we interpolated between the traces. To facilitate comparison with the sections of Figure 10, in each panel we also show (for the corresponding period band) the actual GRT image profile at two locations.

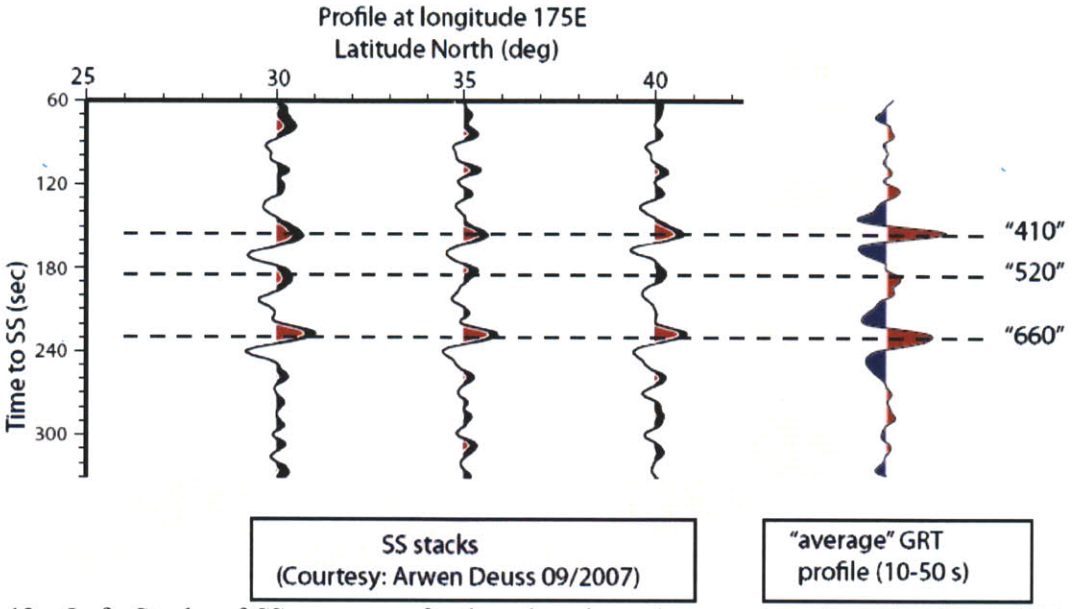

Figure 2-12. Left: Stacks of *SS* precursors for three locations along section shown in Figure 8 (A. Deuss, pers. comm. 2007). Data (T=10-50 s) are stacked over spherical caps with radius of 10° and for a reference distance of 130° (see also *Deuss,* 2009); no crust or 3D mantle correction is applied. Right: 'stack' of the 21 GRT images of Figure 2-10B along the entire section; this stack of the GRT images implies averaging over ~1000 km. The depth is scaled to time to facilitate the comparison.

Chapter 3

Seismic imaging of transition zone discontinuities suggests hot mantle west of Hawaii[†]

Abstract

The Hawaiian hotspot is often attributed to hot material rising from depth in the mantle, but efforts to detect a thermal plume seismically have been inconclusive. To investigate pertinent thermal anomalies we imaged with inverse scattering of SS waves the depths to seismic discontinuities below the Central Pacific, which we explain with olivine and garnet transitions in a pyrolitic mantle. The presence of a 800–2,000 km wide thermal anomaly (ΔTmax~300–400K) deep in the transition zone west of Hawaii suggests that hot material does not rise from the lower mantle through a narrow vertical plume but accumulates near the base of the transition zone before being entrained in flow towards Hawaii and, perhaps, other islands. This implies that geochemical trends in Hawaiian lavas cannot constrain lower mantle domains directly.

3.1 Introduction

An open question in studies of Earth's deep interior concerns mantle plumes, and as the archetype for plume-related hotspot activity Hawaii has long been central to the debate. The canonical view of a narrow thermal plume rising from the lower mantle below the moving Pacific plate (*Wilson, 1963; Morgan, 1971; Davies, 1988; Sleep, 1990; Courtillot et al., 2003*) has been used in studies of Hawaiian lavas (*Hart et al., 1992; Hanano et al., 2010*), plume-plate interaction (*Ribe and Christensen, 1999*), and effects of convective mantle wind on plume morphology and seamount chain development (*Steinberger*

[†]Published as: Q. Cao, R. D. van der Hilst, M. de Hoop, and S.-H. Shim. Seismic imaging of transition zone discontinuities suggests hot mantle west of Hawaii, *Science*, 332, 1068-1071, 2011.

and O'Connell, 1998; Tarduno et al., 2009). The deep-plume paradigm has been questioned, however, and alternative explanations include upwelling from a thermal boundary near the base of the transition zone (*Allègre, 2002*) and shallow mantle processes (*Anderson, 2000*). Tomographic evidence for the existence, location, and depth of origin of the purported plume is still ambiguous (*Grand, 2002; Li et al., 2008; Montelli et al, 2004; Wolfe et al., 2009; Wolfe et al., 2011*; see also Appendix 3.1).

Temperature anomalies associated with a deep plume influence the depth to (pressure induced) mineral phase boundaries, which can be determined from reflections or conversions of seismic waves (*Helffrich, 2000*). Important imaging targets are the olivine-wadsleyite and post-spinel transitions in $(Mg,Fe)_2SiO_4$ near, respectively, 410 and 660 km depth (*Katsura and Ito, 1989*). Due to their opposite Clapeyron slopes, high temperatures would deepen the former and elevate the latter (see appendix 3.2). Receiver functions (*P-to-S* conversions) reveal a thin transition zone southwest of Hawaii (*Li et al., 2000; Collins et al., 2002; Wölburn et al., 2006*) and beneath the Hawaii chain (*Shen et al., 2003*). This suggests high temperatures, but the lateral extent of the anomalies is not constrained because of the small foot-print of seismograph networks on and near the islands.

Transition zone discontinuities can be mapped beyond the reach of receiver functions with reflections – S_dS, with d reflector depth – which arrive as precursors to surface-reflected *SS* waves at sensors far from the study region (Figure 3-1). Conventional methods enhance the weak signals by stacking specular (mirror-like) *SS* reflections across large (10-20° wide) geographical bins (Deuss *et al., 2006; Lawrence and Shearer, 2008; Deuss, 2009; Houser and Williams, 2010; Schmerr et al., 2010*). This averaging yields low spatial resolution, however, and has not yet yielded robust *410* and *660* images beneath Hawaii (see appendix 3.1). Here we use (3D) inverse scattering of the *SS* wavefield, with a method (adapted from hydrocarbon exploration) known as a generalized Radon transform (GRT) (see appendix 3.3). This also exploits data redundancy, but instead of stacking stationary phases over

bins it integrates signal associated with waves scattered from single image points. The feasibility of imaging with *SS* precursors was first demonstrated for an oceanic region far away from known thermal down- and upwellings (*Cao et al., 2010*).

3.2 Methodology and data

We image the transition zone beneath and around Hawaii with ~170,000 broad-band (20-50 s) records of the *SS* wavefield, from ~4,800 earthquakes (magnitude $m_b > 5.2$; focal depth < 75 km) recorded at one or more of a total of ~2,250 seismographic stations around the Pacific (Figure 3-1, see appendix 3.3.1). Data coverage is adequate in most of the study region but degrades toward the southwest (Figure 3-S6C,F). The GRT produces 1-D profiles of elasticity contrasts between 250 and 950 km depth at a 0.5°x0.5° latitude-longitude grid (see appendix 3.3.2 and 3.3.3). These images, which are corrected for 3D mantle heterogeneity (using different tomographic models) and for regional variations in *SS* reflection point depth, constrain interfaces at a radial resolution comparable to that of receiver functions. The closely spaced reflectivity profiles show depth variations (topography) of the *410* and *660* and elucidate structure at other depths that could otherwise be dismissed as noise. We used bootstrap analysis to gain insight into the robustness of the images (see appendix 3.3.5).

3.3 Results

Cross sections through the 3D image volume – for example, across Hawaii (Figure 3-2) – reveal scatter horizons. In addition to reflectors near 410 km and between 650 and 700 km depth, scattering occurs near 350, 500-550, and 800-900 km depth. Most are continuous and have substantial but some appear intermittent or split. We focus here on the traditional boundaries of the transition

In Figure 3-2B we track the *410* and *660* in cross-section, and depth picks for all grid points yield maps discontinuity depth (Figure 3-3A,B), transition zone thickness (Figure 3-3C), and depth correlation (Figure 3-3D).

The depth to *410* varies (on lateral scale of 500-750 km) between 395 and 430 km and the *660* (more smoothly) between 640 and 705 km depth. Below and east of Hawaii (region I) the *660* is slightly shallower than the global average (~650 km). Between Hawaii and 165°W (region II) the *660* is more anomalous (~640 km), which confirms results from P-S conversions (*Li et al., 2000; Collins et al., 2002; Wölburn et al., 2006; Shen et al., 2003*) but extends the anomaly further west than first thought. Between 167-179°W (region III) the *410* reaches 430 km and the *660* appears anomalously deep (~700 km). West of 180° the interfaces are near global average depths (*see appendix*). The regional average depths of *410* and *660* are 413 km and 665 km, respectively, with the latter biased by large values in region III. The transition zone is thin beneath and northwest of Hawaii and thick in region III (Figure 3-3C). The correlation between *410* and *660* is negative in regions I and II and positive in region III (Figure 3-3D).

Two types of artifact can influence image quality and accuracy. First, interface depths will be biased if volumetric wavespeeds differ from the values that we use for travel time calculations (see appendix 3.3.4). This effect is too small to explain the large depth variations across regions II and III, but some trade-off is likely. Spatially coherent depth variations of 10 km or larger are considered meaningful (*Cao et al., 2010*), but for a conservative interpretation the estimates of interface depths are considered upper bounds. Second, sparse sampling (for instance west of Hawaii) can degrade noise reduction and spatial resolution. Visual inspection shows that image gathers (see appendix 3.3.3) are reliable throughout most of the study region, and bootstrapping suggests that the first-order observations in regions I, II, and III are robust at 95% (2σ) confidence level (see appendix 3.3.5). Parts of the deep structures west of Hawaii are, however, at the edge of what is resolved with currently available data.

Even with these uncertainties, the first order observations suggest that Hawaii is located above the eastern margin of a large-scale topographic feature comprising an anomalously deep *410* and *660* and a thick transition zone (region III), surrounded by shallow *660* and a thinner transition zone (regions I, II). This unexpected structural complexity suggests large variations in temperature (and, perhaps, composition) near the upper-lower mantle boundary beneath Hawaii and environ. To estimate in situ mantle temperatures near the top (ΔT_{410}) and bottom (ΔT_{660}) of the transition zone we use pressure-temperature dependencies (that is, Clapeyron slopes Γ) of olivine and garnet transitions in a mantle of pyrolitic bulk composition (see appendix 3.2). Non-pyrolitic compositions are not needed to explain the first-order observations discussed here.

We first interpret the observations in terms of transitions in $(Mg,Fe)_2SiO_4$ olivine: i.e., olivine/wadsleyite (~410 km, $\Gamma 410 \approx 2.5$ MPa/K (*Morishima et al., 1994*)), wadlseyite/ringwoodite (~520 km, $\Gamma 520 > 0$, the Clapeyron slope of the wadsleyite to ringwoodite transition is positive (*Suzuki et al., 2000*) but not well constrained experimentally), and ringwoodite/perovskite+ ferropericlase (post-spinel) (~660 km, $\Gamma p\text{-}sp \approx -2.7$ MPa/K (*Irifune et al., 1998*)). Temperature maps obtained with these slopes (see appendix 3.4) reveal a weak perturbation ($\Delta T410 \approx \Delta T660 \approx 150K$) below and east of Hawaii (region I) but larger anomalies further west. Interpreting the shallow *660* in region II as updoming of the post-spinel boundary yields $\Delta T_{660} \approx 300K$, in accord with previous estimates (*Li et al., 2000; Collins et al., 2002*), whereas the small ΔT_{410} suggests that the broad anomaly is confined to the base of the transition zone. The 3D structure is complicated, however, and further north a deep *410* and shallow *660* suggest high temperatures in the upper mantle beneath the Hawaii chain (*Shen et al., 2003*). The deep *660* (region III) is enigmatic. For $\Gamma_{p\text{-}sp}$ as above, a change in post-spinel depth from 640 700 km implies a temperature difference of ~850 K. Such a large gradient is unrealistic far away from plate margins. The *660* depth could be overestimated if wavespeeds above (below) *660* are lower

(higher) than the tomographically inferred values used for 3D mantle corrections. Some trade-off is likely, but explaining all signal this way requires implausible seismic and (probably) thermal anomalies (see appendix 3.3.4). For realistic values of $\Gamma_{p\text{-}sp}$, ΔT_{660}, and upper mantle velocities, the post-spinel transition does not seem a plausible explanation of the interface near 700 km depth.

Large *410* and *520* depths suggest elevated transition zone temperatures in region III. Multi-anvil experiments have shown (*Weidner and Wang, 1998; Hirose, 2002; Nishiyama and Yagi, 2003*) that at high temperatures different phase relations and Al partitioning increase the (seismic) impedance contrast at post-garnet transitions. Such experiments are challenging, however, and important aspects of the phase relations, such as the magnitude of the positive Clapeyron slope ($\Gamma_{p\text{-}gt}$) and the effects of composition on the location and seismic detectability of the post-garnet transition (relative to post-spinel), are still uncertain (see appendix 3.2). The possibility that the post-garnet transition occurs deeper in hot (and, perhaps, Al_2O_3 rich) mantle than post-spinel in normal mantle has been invoked to explain geographically isolated findings of a deep *660* (*Deuss et al., 2006; Houser and Williams, 2010*), and our images may depict a lateral change from post-spinel (in region II) to post-garnet (in III). Given the possible trade-offs and uncertainties in Clapeyron slope and Al_2O_3 content (in pyrolite), estimating ΔT_{660} at the post-garnet transition is fraught with uncertainty, but $\Gamma_{p\text{-}gt}$=3.0 MPa/K (*Akaogi and Ito, 1999*) would yield and upper bound of 450 K (with a lower bound set by the temperature at the post-spinel transition in region II).

The inference that the mantle near 660 km depth is hot west of Hawaii, over a region that is at least 800 km wide (if restricted to region II) but possibly as broad as 2,000 km (if it includes region III), suggests that hot material accumulates and spreads near the top of the lower mantle and that hotspot volcanism may be fueled by secondary upwellings (*Courtillot et al., 2003; Cserepes and Yuen, 2000*, see appendix 3.5) from the base of the transition zone (Figure 3-4). This is not consistent with tomographic

views of a lower mantle plume southeast of Hawaii (*Wolfe et al., 2009; Wolfe et al., 2011*), but currently available travel time data may not be able to resolve between a continuous plume-like structure and separate anomalies at different depths in the mantle (see appendix 3.1).

3.4 Conclusions and discussions

Discontinuity topography reflects local conditions and cannot, by itself, constrain the origin, longevity, and depth extent of the deep anomaly. However, the temperature contrast and the sustained flux required to feed volcanism at the surface (if, indeed, they are related) indicate that it is not an isolated, ephemeral structure but that it is rejuvenated from below, for instance by a thermal plume or a larger-scale (thermochemical) mantle dome (*Courtillot et al., 2003*). If there is a connection, the transient nature of instabilities rising from the transition zone can help explain irregularities in the evolution (age progression) of the Hawaii-Emperor seamount chain (*Tarduno et al., 2009*). Furthermore, the lateral changes of dominant phase transition systems may influence mass exchange between upper and lower mantle. Depending on the combined effects of the width of the post-garnet transition, the density contrasts at each of the high-temperature transitions (i.e., spinel ↔garnet+magnesiowüstite ↔ perovskite+magnesiowüstite), the value of $\Gamma_{p\text{-}gt}$, and composition, post-garnet transitions may facilitate the formation of secondary upwellings and contribute to the elevated upper mantle temperatures in region III, a positive geoid anomaly, and, perhaps, the richness of bathymetric features away from seamount chains. Finally, any temporary ponding of lower mantle flow at *660* suggests that pipe flow or zonation of mantle plumes (*Hanano et al., 2010; DePaolo and Stolper, 1996; Blichert-Toft and Albarède, 2009; Farnetani and Hofmann, 2009*) must be shallow mantle phenomena, and that isotope signatures of surface lavas cannot be used to map geochemical domains in the lower mantle.

Acknowledgments: This research was supported by grants of the CSEDI (Collaborative Studies of Earth's Deep Interior) and CMG (Collaborative Mathematical Geosciences) programs of the US National Science Foundation. The seismic waveforms used here were all retrieved from the Data Management Center of IRIS (Incorporated Research Institutions for Seismology).

References Cited

Akaogi, M., E. Ito, 1999. Calorimetric study on majorite–perovskite transition in the system $Mg_4Si_4O_{12}$–$Mg_3Al_2Si_3O_{12}$: Transition boundaries with positive pressure–temperature slopes. *Phys. Earth Planet. Inter.*, 114, 129.

Allègre, C.J., 2002. The evolution of mantle mixing. *Philos. Trans. R. Soc. Lond. A*, 360, 2411.

Anderson, D.L., 2000. Thermal State of the Upper Mantle; No Role for Mantle Plumes. *Geophys. Res. Lett.*, 27, 3623.

Blichert-Toft, J., F. Albarède, 2009. Mixing of isotopic heterogeneities in the Mauna Kea plume conduit. *Earth Planet. Sci. Lett.*, 282, 190.

Cao, Q., P. Wang, R. D. van der Hilst, M. V. de Hoop, S.-H. Shim, 2010. Imaging the upper mantle transition zone with a generalized Radon transform of *SS* precursors. *Phys. Earth Planet. Inter.*, 180, 80.

Collins, J. A., F. L. Vernon, J. A. Orcutt, R. A. Stephen, 2002. Upper mantle structure beneath the Hawaiian swell: Constraints from the ocean seismic network pilot experiment. *Geophys. Res. Lett.*, 29, 1522.

Courtillot, V., A. Davaille, J. Besse, J. Stock, 2003. Three distinct types of hotspots in the Earth's mantle. *Earth Planet. Sci. Lett.*, 205, 295.

Cserepes, L., D. A. Yuen, 2000. On the possibility of a second kind of mantle plume. *Earth Planet. Sci.*

Lett., 183, 61.

Davies, G.F., 1988. Ocean bathymetry and mantle convection 1. Large-scale flow and hotspots. *J. Geophys. Res.*, 93, 10467.

DePaolo, D. J., E. M. Stolper, 1996. Models of Hawaiian volcano growth and plume structure: Implications of results from the Hawaii Scientific Drilling Project. *J. Geophys. Res.*, 101, (B5), 11643.

Deuss, A., S. A. T. Redfern, K. Chambers, J. H. Woodhouse, 2006. The nature of the 660-kilometer discontinuity in Earth's mantle from global seismic observations of *PP* precursors. *Science*, 311, 198.

Deuss, A., 2009. Global observations of mantle discontinuities using *SS* and *PP* precursors. *Surv. Geophys.*, 30, 301.

Engdahl, E. R., R. D. Van der Hilst, R. P. Buland, 1998. Global teleseismic earthquake relocation with improved travel times and procedures for depth determination. *Bull. Seismol. Soc. Am.*, 88, 722.

Farnetani, C. G., A. W. Hofmann, 2009. Dynamics and internal structure of a lower mantle plume conduit. *Earth Planet. Sci. Lett.*, 282, 314.

Grand, S.P., 2002. Mantle shear-wave tomography and the fate of subducted slabs. *Philos. Trans. R. Soc. Lond. A*, 360, 2475.

Hanano, D., D. Weis, J. S. Scoates, S. Aciego, D. J. DePaolo, 2010. Horizontal and vertical zoning of heterogeneities in the Hawaiian mantle plume from the geochemistry of consecutive postshield volcano pairs: Kohala-Mahukona and Mauna Kea–Hualalai. *Geochem. Geophys. Geosyst.*, 11, Q01004.

Hart, S.R., E. H. Hauri, L. A. Oschmann, J. A. Whitehead, 1992. Mantle plumes and entrainment: Isotopic evidence. *Science*, 256, 517.

Helffrich, G., 2000. Topography of the transition zone seismic discontinuities. *Rev. Geophys.*, 38, 141.

Hirose, K., 2002. Phase transitions in pyrolitic mantle around 670-km depth: Implications for

of plumes from the lower mantle. *J. Geophys. Res.*, 107, (B4), 2078.

Houser, C., Q. Williams, 2010. Reconciling Pacific 410 and 660 km discontinuity topography, transition zone shear velocity patterns, and mantle phase transitions. *Earth Planet. Sci. Lett.*, 296, 255.

Irifune, T., N. Nishiyama, K. Kuroda, T. Inoue, M. Isshiki, W. Utsumi, K. Funakoshi, S. Urakawa, T. Uchida, T. Katsura and O. Ohtaka, 1998. The postspinel phase boundary in Mg_2SiO_4 determined by in situ X-ray diffraction. *Science*, 279, 1698.

Katsura, T., E. Ito, 1989. The system Mg_2SiO_4-Fe_2SiO_4 at high pressures and temperatures: Precise determination of stabilities of olivine, modified spinel, and spinel. *J. Geophys. Res.*, 94, 15663.

Kennett, B. L. N., E. R. Engdahl, R. P. Buland, 1995. Constraints on seismic velocities in the Earth from traveltimes. *Geophys. J. Int.*, 122, 108.

Lawrence, J., P. M. Shearer, 2008. Imaging mantle transition zone thickness with S_dS - SS finite-frequency sensitivity kernels. *Geophys. J. Int.*, 174, 143.

Li, X., R. Kind, K. Priestley, S. V. Sobolev, F. Tilmann, X. Yuan and M. Weber, 2000. Mapping the Hawaiian plume conduit with converted seismic waves. *Nature*, 405, 938.

Li, C., R. D. van der Hilst, E. R. Engdahl, S. Burdick, 2008. A new global model for P wave speed variations in Earth's mantle. *Geochem. Geophys. Geosyst.*, 9, Q05018.

Montelli R., G. Nolet, F. A. Dahlen, G. Masters, E. R. Engdahl and S. Hung, 2004. Finite-frequency tomography reveals a variety of plumes in the mantle. *Science*, 303, 338.

Morgan, W.J., 1971. Convection plumes in the lower mantle. *Nature*, 230, 42.

Morishima, H., T. Kato, M. Suto, E. Ohtani, S. Urakawa, W. Utsumi, O. Shimomura, T. Kikegawa, The phase boundary between agr- and beta-Mg_2SiO_4 determined by in situ X-ray observation. *Science*, 265, 1202.

Nishiyama, N., T. Yagi, 2003. Phase relation and mineral chemistry in pyrolite to 2200°C under the lower mantle pressures and implications for dynamics of mantle plumes. *J. Geophys. Res.*, 108, 2255.

Ribe, N.M. U. R. Christensen, 1999. The dynamical origin of Hawaiian volcanism. *Earth Planet. Sci. Lett.*, 171, 517.

Schmerr, N., E. Garnero, A. McNamara, 2010. Deep mantle plumes and convective upwelling beneath the Pacific Ocean. *Earth Planet. Sci. Lett.*, 294, 143.

Shen, Y., C. J. Wolfe, S. C. Solomon, 2003. Seismological evidence for a mid-mantle discontinuity beneath Hawaii and Iceland. *Earth Planet. Sci. Lett.*, 214, 143.

Sleep, N. H., 1990. Hotspots and mantle plumes: Some phenomenology. *J. Geophys. Res.*, 95, 6715.

Steinberger, B., R. J. O'Connell, 1998. Advection of plumes in mantle flow: Implications for hotspot motion, mantle viscosity and plume distribution. *Geophys. J. Int.*, 132, 412.

Suzuki, A.; E. Ohtani; H. Morishima; T. Kubo; Y. Kanbe; T. Kondo; T. Okada; H. Terasaki; T. Kato; T. Kikegawa, 2000. In situ determination of the phase boundary between wadsleyite and ringwoodite in Mg_2SiO_4. *Geophys. Res. Lett.*, 27, 803.

Tarduno, J., H.-P. Bunge, N. Sleep, U. Hansen, 2009. The bent Hawaiian-Emperor hotspot track: Inheriting the mantle wind. *Science*, 324, 50.

Weidner, D. J., Y. Wang, 1998. Chemical- and Clapeyron-induced buoyancy at the 660 km discontinuity. *J. Geophys. Res.*, 103, (B4), 7431.

Wilson, J.T. , 1963. A possible origin of the Hawaiian islands. *Can. J. Phys.*, 41, 863–870.

Wolfe C.J., S. C. Solomon, G. Laske, J. A. Collins, R. S. Detrick, J. A. Orcutt, D. Bercovici and E. H. Hauri, 2009. Mantle shear-wave velocity structure beneath the Hawaiian hot spot. *Science*, 326, 1388.

Wolfe C.J., S. C. Solomon, G. Laske, J. A. Collins, R. S. Detrick, J. A. Orcutt, D. Bercovici and E. H.

Hauri, 2011. Mantle P-wave velocity structure beneath the Hawaiian hotspot. *Earth Planet. Sci. Lett.*, 303, 267.

Wölbern, I., A. W. B. Jacob, T. A. Blake, R. Kind, X. Li, X. Yuan, F. Duennebier, M. Weber, 2006. Deep origin of the Hawaiian tilted plume conduit derived from receiver functions. *Geophys. J. Int.*, 166, 767.

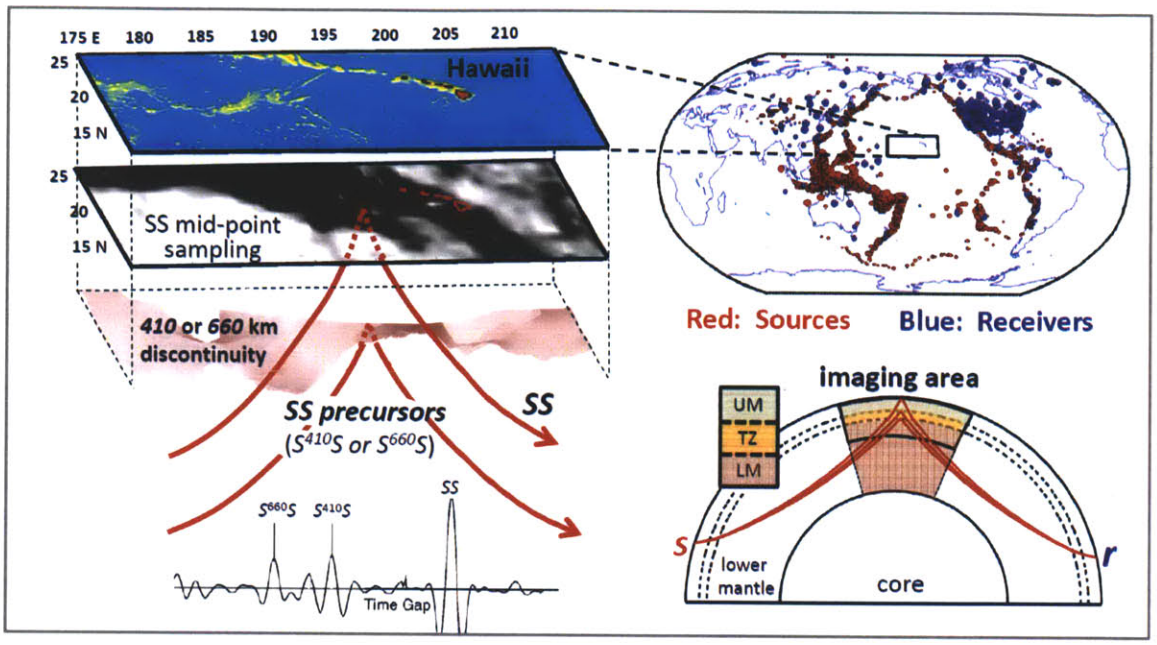

Figure 3-1. Left, top-to-bottom: map of study region (175-214°E; 12-26°N; Mercator projection, perspective view); Geographical distribution of ~170,000 surface mid-points of *SS* waves (the darker, the denser the coverage (Appendix 3.2); Path geometry of underside reflections at the surface (*SS*) and an upper mantle discontinuity ($S^{410}S$ or $S^{660}S$); precursor stack showing signal associated with $S^{660}S$, $S^{410}S$, and *SS* waves (after *Houser and Williams, 2010*). Right, from top to bottom: Geographical distribution of ~4,800 sources (red symbols) and ~2,250 receivers (blue) from which data is used, and which produces the data coverage shown on the left; Schematic view of ray geometry of *SS*, $S^{410}S$, and $S^{660}S$ sampling the upper mantle transition zone below the imaging area (UM=upper mantle, TZ=transition zone; LM=lower mantle).

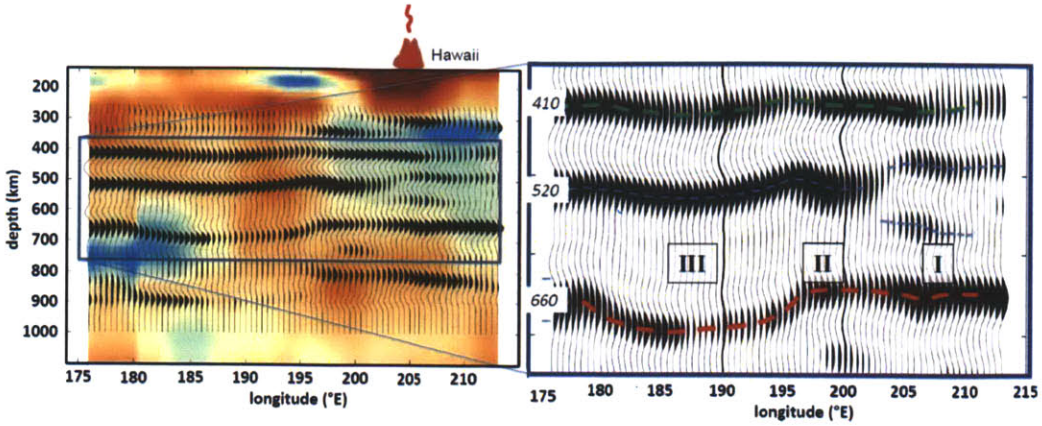

Figure 3-2. Seismic section (E-W) across Hawaii (see Figure 3-3 for section location). Left: seismic image superimposed on tomographically inferred wavespeed variations (*Grand, 2002*). Right: blow up of image between 370 and 760 km depth, along with interpretation of *410* (dashed green line), *520* (blue), and *660* (red) discontinuities. The depth profiles are corrected for 3D mantle heterogeneity (from tomography) and for the depth to the ocean floor where *SS* reflections occur. Inverse scattering does not assume contiguous reflectors (Appendix 3.2), but alignment suggests lateral continuity. Interfaces appear as a pulse with sidelobes, the width of which depends on frequency of the data and the angle at which image points are sampled (*Cao et al., 2010*). Horizontal resolution (which depends on illumination) is estimated to be of the order of a few 100 km in the center of the study region (degrading to ~500 km towards the southwest owing to reduced sampling). I, II, and III mark regions discussed in the main text. The image gathers at 190°E and 200°E (highlighted in section on the right) are discussed in (Appendix 3.3, Figure 3-S7).

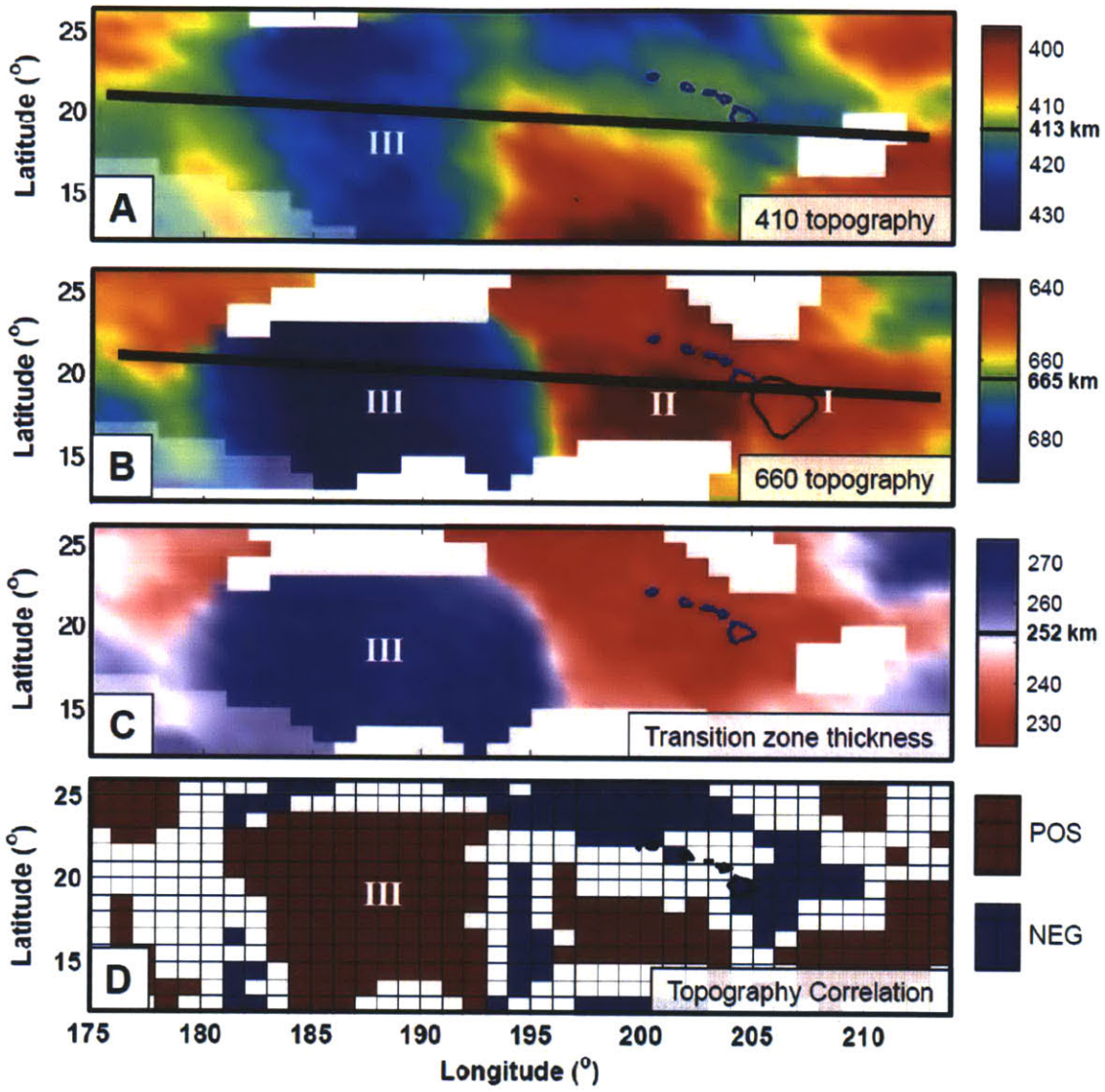

Figure 3-3. Discontinuity depths, transition zone thickness, and depth correlations in the study region. (A) Topographic map of *410* (regional average 413 km) and (B) *660* (regional average 665 km). Fat black solid line depicts location of E-W cross section in Figure 3-2, and thin black line in (B) indicates the location (at 700 km depth) of the mantle plume identified in (*Wolfe et al., 2009*) – see also Figure 3-S2B. I, II, and III mark the regions discussed in the main text. (C) The difference between *410* and *660* depths suggests that a relatively thin transition zone (passing through Hawaii) surrounds a thick transition (between 180-195°E, Region III). (D) Correlation between *410* and *660* depth variations (in regions where *410* and *660* topography exceeds 2.5 and 5 km, respectively). Interface depths are (weakly) negatively correlated beneath Hawaii but conspicuous positive correlation appears in Region III. In (A-C) regions where the *410* or *660* could not be identified unambiguously are left blank, and light shading indicates areas of relatively poor data coverage.

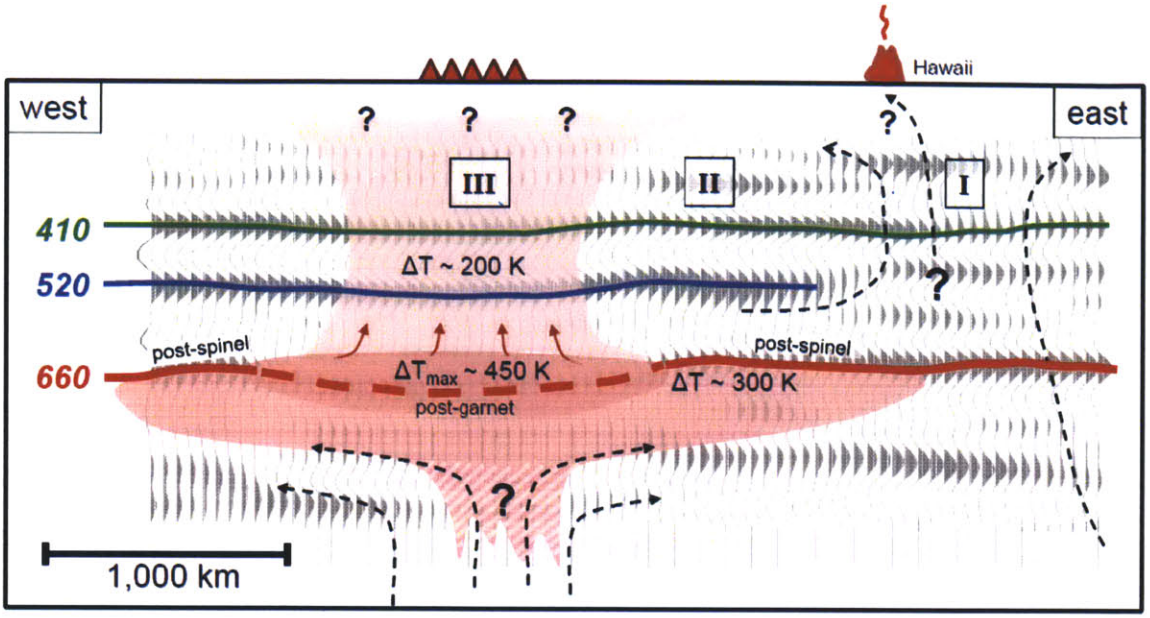

Figure 3-4. Cartoon of broad anomaly near base of the transition zone west of Hawaii, superimposed on a scattering image (Figure 3-2). Green, blue, and red lines depict interfaces near 410, 520, and 660 km depth. The deep *410* and *520* west of Hawaii suggest higher-than-average temperatures ($\Delta T_{410} \approx 200K$) in the upper mantle and transition zone, but with current data coverage we cannot distinguish between a large single anomaly and multiple smaller ones. Updoming of the *660* beneath region II is consistent with elevation of post-spinel transition in hot mantle regions (with $\Delta T_{660} \approx 300$ K), whereas deepening to ~700 km beneath III (red dashed line) may indicate change of dominant transition system to garnet (with $\Delta T_{660,\,max} \approx 450$ K). The positive Clapeyron slope of the latter may aid flux of lower mantle material into the transition zone (thin red arrows). Pathways of flow from the deep anomaly to Earth's surface are not resolved by the data used, but Hawaii volcanism may result from upwellings from the (edge of the) broad anomaly (for instance just east of Hawaii, region I, Figure 3-3).

Appendix 3.1: Non-unique views on mantle structure beneath Hawaii

Comparisons of independently derived models suggest that from currently available travel time tomography and SS precursor stacking results there is no consensus yet on the existence, shape, and location of a plume-like thermal upwelling beneath Hawaii.

Estimating variations in volumetric wavespeed and depths to upper mantle interfaces beneath Hawaii is difficult because of the large distance to regions with abundant seismicity (that is, the sources for imaging) and the small footprint of seismograph networks on and near Hawaii. As a result, sampling is relatively sparse and *P*- and *S*-waves from teleseismic earthquakes arrive at Hawaii along steep propagation paths. Travel time tomography is then prone to smearing along steep and narrow ray bundles: the data may only sample parts of what could be structures of (much) larger lateral extent, and as a result of smearing separate (slow) anomalies at different depths may appear as continuous structures. Figure 3-S1 illustrates non-unique views on mantle structure beneath Hawaii (*Li et al., 2008; Wolfe et al., 2009*). Depending on the data used the slow anomaly is mapped at different locations with respect to Hawaii, from west (Figure 3-S1A) to southeast (Figure 3-S1B) of the site of present-day hotspot activity at the surface.

Cross sections through these models reveal "plume like" structures at different locations and dipping in opposite directions (Figure 3-S2). Our P wave model (*Li et al., 2008*) suggests slow wavespeeds west of Hawaii, for instance, in region II, and the implied elevated temperature is qualitatively consistent with the imaging results presented here. The *P*-wave anomaly has the appearance of a continuous conduit dipping deep into the lower mantle, but this could be an artifact because resolution is poor in the downdip direction (*Li et al., 2008*).

Interface imaging with precursors to the surface reflected *SS* wave, which reflect at upper mantle discontinuities, is not dependent on seismographs in the study region (Figure 3-1), but geographical

sampling by such underside reflections is uneven in the Central Pacific and rather sparse west of (see Figure 3-1 and Figure 3-S6C). Moreover, approaches that involve regional stacks of stationary phases (that is, the ray-theoretical, mirror-like spectacular reflections) over geographical bins assume that the depth to and elastic properties of the interface is constant within the bin over which the data are stacked (Figure 3-S6A). Typical bin sizes are 10°-20° (*Deuss, 2009*), which implies averaging of topography over 1,000-2,000 km. Combination of sparse sampling and the averaging over large bins yields smooth representations of interface topography. Even at low resolution, however, the maps of discontinuity depth – or the thickness of the transition zone inferred from them – differ between studies, as illustrated in Figure 3-S3 for two different renditions of transition zone thickness (*Lawrence and Shearer, 2008; Deuss, 2009*).

Appendix 3.2: Phase diagrams

Figure 3-S4 summarizes the main phase relationships in a pyrolitic mantle composition. Previous studies assigned complex seismic structures near the base of the mantle transition zone to the post-garnet transition (*Deuss et al., 2006; Houser and Williams, 2010*), but these findings were geographically isolated and could not be put in context of geodynamical processes. Moreover, substantial uncertainties exist near the depths of the post-garnet and post-spinel transitions (*Weidner and Wang, 1998; Hirose, 2002; Nishiyama and Yagi, 2003*), which is important for our interpretation for the topography at the base of the mantle transition zone.

An earlier study assumed that the depth of the post-garnet transition is within the range for the of the post-spinel transition (*Weidner and Wang, 1998*). Although this was investigated by later studies (*Hirose, 2002; Nishiyama and Yagi, 2003*), due to the experimental difficulties with multi-anvil experiments over 24 GPa neither the location of the post-garnet transition with respect to the

transition nor the Clapeyron slope of the post-garnet transition are well constrained. Moreover, the location of the post-garnet transition depends on aluminum (Al_2O_3) content whereas that of the post-spinel transition does not, and even a small increase in Al_2O_3 stabilizes garnet and thus increases depth of the post-garnet transformation. It is thus likely that the post-garnet transition in hot and, in particular, Al_2O_3 rich mantle occurs at a greater depth than the post-spinel transition in normal mantle, but due to the experimental uncertainties and effects of composition it is difficult to invert topography into temperature. This calls for mineral physics studies on phase relation at the pressure-temperature conditions of the transition zone with a range of different Al_2O_3 content.

Figure 3-S5 illustrates the relationships between temperature perturbations and depth to phase boundaries for different styles of convective flow across the mantle transition zone. If the thermal anomalies are the same throughout the transition zone (Figure 3-S5A,B) then anti-correlation between depth variations of the *410* and *660* are expected because of the opposite slopes of the associated phase transitions in the olivine system (Figure 3-S5C). If, however, flow across the transition zone is more complicated, such anti-correlation may not appear. Indeed, deflection of upwellings (Figure 3-S5D) and downwellings (Figure 3-S5E) at the upper-lower mantle boundary could produce much longer wavelength topography of *660* than *410,* thus removing the appearance of anti-correlation. This boundary layer effect has been inferred for downwellings and our current study shows that it may also occur for upwellings.

Appendix 3.3: Data and Methodology – Inverse Scattering

We refer to Cao et al. (*Cao et al., 2010*) for a detailed description of the method and tests of resolution and effects of interfering phases and multiple reverberations. Here we describe only the main We note that for illustration purposes we use (minimum phase) top-side reflections (with non-specular

energy arriving in the coda of the main phase), but the principles are the same for (mixed phase) underside reflections (with non-specular energy arriving as precursors to the main phase).

Appendix 3.3.1: Data selection and processing

With the ever increasing volumes of modern data sets, scrutiny of individual records is not always practical. As in exploration imaging, our approach relies on the noise reducing capabilities of large data sets. By accounting for scattering in 3D, the GRT uses this data redundancy to extract coherent signal from a large number of seismic traces. However, we only use data that passes carefully designed (automated) data selection and quality control criteria.

From the Data Management Center (DMC) of the Incorporated Research Institutions for Seismology (IRIS) we retrieve broadband waveforms for *SS* waves with midpoints in a 30° ×50° area from 5° to 35°N and 170° to 220°E. The data selection criteria are similar to those used by Cao *et al.*. We select data with epicenter distance between 90° and 170°, source magnitude m_b > 5.2 and focal depths less than 75 km. We extract time windows containing SS proper and precursors due to scattering in the transition zone. Data file header information is updated with hypocenter parameters from the EHB catalog (*Suzuki et al., 2000*). Then we check (and, if needed, correct) polarization, deconvolve the instrument response, rotate the data to radial and transverse direction, and then use a 4-pole Butterworth filter to bandpass the data between 20 and 50 s. A Hilbert transform is applied to the traces followed by normalization of amplitude with respect to *SS*.

To mitigate effects of noise and different source wavelets, we carried out principal component analyses. First we shifted all the traces from the same event based on relative delay times using multichannel cross-correlation over a window containing the *SS* arrival. Traces associated with average

cross-correlation values less than 0.5 are discarded. Then we extract the first eigenvector from the matrix formed by the array of remaining traces. This vector approximates the source wavelet and is deconvolved from the traces. Upon imaging each trace is weighed with the corresponding cross-correlation value in order to suppress the influence of noisy traces.

Appendix 3.3.2: Basic principles of GRT and conventional SS stacking

Traditional imaging of upper mantle discontinuities with *SS* underside reflections – see (*Deuss, 2009*) for a recent review – follows the process of a primitive of time migration and involves stacking of main phases after 'normal move out' correction (which accounts for differences in offset, or epicentral distance). Assuming lateral invariance of the interface (in spherical geometry) one typically averages over midpoints in large spatial bins (Figure 3-S6A). Subsequently, the time image is subjected to a time-to-depth conversion – using a 1-D reference (or 3D tomographic) model – to obtain an image in (radial) depth. Because any lateral variations will be averaged across a bin, interface depth anywhere in the bin will be biased towards the part that is best illuminated by the data. In Figure 3-S6A, for example, the image over the deeper part of the undulating reflector (gray dashed line) will be biased to shallow depth because only that part is 'sampled'.

Inverse scattering is based on diffraction and does not identify specular reflections. It also exploits data redundancy, but instead of regional stacking of (move-out corrected) specular reflections (Figure 3-S6A,B) it involves stacking of signal associated with scattered waves (Figure 3-S6D,E) that sample image points at different directions (*Cao et al., 2010*).

In forward sense, δu is signal at reflection time t from source to the image point to receiver and its strength depends on the elasticity contrast (Δc) at that point, and on source characteristics and

propagation effects: $\delta u = F\Delta c$, with F the operator that maps model parameters to data. Upon inversion, the GRT maps data samples (denoted by δu) to isochrons, which are surfaces that connect points in the subsurface with constant reflection time t for a given source-receiver pair. The isochron represents the sensitivity kernel corresponding to inverse scattering, which contains the imprint of the Fresnel zone of finite frequency waves. If the data consists of reflections off piecewise smooth reflectors, such as the discontinuities in the transition zone, the main contribution to inverse scattering occurs at stationary raypaths or specular reflections (*Cao et al., 2010*).

With the GRT we estimate elasticity contrasts at a 3D grid of image points. At each grid point, the contribution from a data sample δu_i is given by $(F^*F)^{-1} F^*\delta u_i$, where F^* is the adjoint of F, that is, the imaging operator, and $(F^*F)^{-1} F^*$ is the inverse scattering operator – where $(F^*F)^{-1}$ corrects for source and contrast source radiation patterns and illumination. The total contrast, Δc, is then obtained by integration (stacking) over all (weighted) data samples (Figure 3-S6E): $\Delta c = \sum (F^*F)^{-1} F^*\delta u_i$. Through $(F^*F)^{-1} F^*$ the main contribution comes from stationary (specular) ray pairs.

The contribution to the elasticity contrast (Δc) at an image point will be small if either the signal at time t or the data sensitivity is small. This is the case for an image point that is not near a scatterer (or reflector) – for instance, image point II in Figure 3-S6D (with small signal at the corresponding reflection time, marked by green box) – or which is not well sampled by data (that is, if the image point is far from the specular point). On the other hand, the contribution to contrast Δc will be large if the signal (δu) and the sensitivity ($(F^*F)^{-1} F^*$) are both large. This will be the case for an image point at or near a reflector that is well sampled by the data used.

The spatial resolution is controlled by the Rayleigh-diffraction limit (not by the Fresnel zones of the associated waves) and depends on the available frequencies and on the range of migration dips, that is the angles at which isochrons intersect at the image point (which, in turn, depends on source-receiver

distribution). Low frequencies will blur the contrast (within the Rayleigh diffraction limit) and small ranges of migration dip will produce smearing along isochrons (*Cao et al., 2010*).

The distribution of (stationary phase) midpoints in the study region is uneven and decreases to near zero southwest of Hawaii (Figure 3-S6C). This suggests that with traditional regional stacking and currently available data it is difficult to produce robust images of transition zone discontinuities far west of Hawaii. Since inverse scattering exploits signal associated with scattered waves (and not just specular reflections), the effective data coverage that can be exploited to constrain interface depth (Figure 3-S6F) is better than in case of stacking of specular reflections. This enables imaging, albeit with lower spatial resolution (Appendix 3.2), in regions west of Hawaii (such as Region III in our study, Figure 3-2 and 3-3), which are poorly sampled by stationary phases (Figure 3-S6C). However, signal associated with the stationary pair must be contained in the data (integration) in order to generate accurate images of a reflector.

Appendix 3.3.3: Image Gathers and 3D image volume

The GRT exploits data redundancy through construction of images of the same point in the sub-surface for a wide range of scatter angles; integration in the angle domain then generates 1D profiles of reflectivity as function of depth, or the GRT image, $\Delta c(z)$, and lateral juxtaposition of these profiles produces 2D seismic sections or 3D image volumes (*see appendix*). Figure 3-S5 illustrates this process – and presents so called common image point gathers and associated GRT images – for locations in region II and III along the seismic section of Figure 3-2.

For each image gather at a specific geographic location we consider data samples from all seismic records, but scattering near the specular point contributes most to the image (because that is where

sensitivity is largest – see Appendix 3.2, above) and must be included to generate an accurate image of the reflector.

We calculate reflectivity $\Delta c(z)$ for image points at 2 km depth intervals, and 1D reflectivity profiles are calculated on a 0.5°×0.5° (longitude, latitude) grid. The construction of the 3D image volume for the mantle volume under study (from 175-214°E and 10-26°N and 200-950 km depth) thus involves computation of Δc at almost a million image points from a total of ~170,000 broadband records. In Figure 3-S7 the total number of seismic traces used as a function of scattering angle is shown (as a histogram) above the image gathers. The image in region II (Figure 3-S7A) is constrained by data over a wider range of scatter angle than the image in region III (Figure 3-S7B). Indeed, for the latter, many of the traces considered in the integration are associated with small weights (Appendix 3.2) and contribute little to the final image gather. This suggests, qualitatively, that the lateral resolution (related to the range of migration dips, or angles at which isochrones intersect) is better in region II than in region III. (NB. Radial resolution, which is a function of available frequencies and scatter angles, with smaller angles providing better radial resolution (*Cao et al., 2010*), is similar in region II and III.)

We note also that the current implementation of GRT is largely kinematic; that is, we consider travel times and geometrical spreading but ignore effects of elastic focusing (due to 3D heterogeneity) on wave amplitudes. As a result the true amplitudes of the reflectivity contrasts are not well constrained. Full dynamic corrections are a target of future research.

Appendix 3.3.4: Corrections for 3D structure and trade-off with wavespeeds

Upon construction of image gathers we correct travel times for 3D mantle heterogeneity using

tomographically inferred wavespeed variations. In the current implementation we use a first order perturbation, that is, we calculate time differences accrued along raypaths calculated in the 1D reference model *ak135* (*Kennett et al., 1995*) and do not trace propagation paths in 3D. We correct for structure along the entire ray, not just in the transition zone region. For 3D corrections we considered several tomographic models. The results shown here are corrected for heterogeneity using the model by Grand (*Grand, 2002*), but the effects of the choice of model is small compared to the large topography that is visible in, for instance, Figure 3-2 and 3-3. We note, however, that subtle distortions of pulse shapes, including minor splitting, fall within the uncertainty of true wavespeed variations.)

However, tomography is known to represent a smoothed and muted depiction of actual wavespeeds, and propagation speeds in Earth's interior that are substantially different from the tomographically inferred values would influence the images. If the range of angles considered in GRT image reconstruction is sufficiently large, a local move out correction can be applied to update the local wavespeed and avoid pulse distortion and depth bias. This is not done here. Consequently, we must consider the possibility of trade-off between volumetric wavespeed variations and location of scatter points.

The type of trade off depends on how the inversion is set-up. The transit time Δt between two interfaces depends on wavespeed v and distance between the interfaces h: $\Delta t=\Delta h/v$. A shallow interface and low wavespeeds can thus yield the same Δt as a deep interface and high wavespeeds. The case considered here is different, however, and this is illustrated for a slow anomaly in Figure 3-S8. If the wavespeed above the interface under consideration is less than the reference values used (that is, the 1D model and the 3D tomographic perturbations) the surface reflected *SS* wave will be delayed relative to the precursor, which does not see the wavespeed anomaly (Figure 3-S8B). But subsequent

alignment on *SS* will transfer the time shift to the precursor, which upon time-depth conversion with fixed velocity will give the appearance of larger interface depth (Figure 3-S8C). Interface depth would also be overestimated if a substantial high wavespeed anomaly beneath the interface of interest is only sampled by the precursor (*SdS*) and not *SS* (Figure 3-S8D).

For realistic wavespeed anomalies, these depth biases are small, however, compared to the large depth variations inferred from the images (e.g., Figure 3-2 and 3-3). Moreover, attributing the deep interface in Region III produces inconsistent depth anomalies for the *410* and *520* discontinuities.

Let us consider three possibilities. (i) Suppose that the deep *410* in region III is an artifact due to the presence of an upper mantle ($z < 410$ km) anomaly that is slower than assumed in our background wavespeed model (that is, *ak135* + 3D perturbations from tomography). The 5% anomaly that is needed to remove the downwarp of the *410* in Region III would move the *660* upward (from almost 700 km, Figure 3-3) to a depth of 675 km. This is still anomalously deep (and some 35 km deeper than the interface in nearby regions, e.g., region II). Moreover, a 5% wavespeed perturbation should be considered an upper bound because an unperturbed *410* is inconsistent with the thermal perturbation that such a wavespeed anomaly would imply (unless the entire anomaly would be caused by composition, volatiles, or melt), and smaller values would render a deeper *660*. (ii) Suppose that the *660* in region III is, in fact, the post-spinel boundary and that its anomalous depth is due to the use of incorrect mantle wavespeeds. This would require that (on average) the upper mantle and transition zone to be (at least) 6% slower (and several hundred degree hotter than average if the perturbation is largely thermal), more if *660* is to be shallower-than-average in the presence of the implied high temperatures. Such strong perturbations (over such a large region) are unrealistic, and would – moreover – result in an upwarp of the *410* and *520,* which is opposite of what is observed and of what one would expect in such a hot upper mantle and transition zone. (iii) Suppose that the deep *660* is an

artifact due to the presence of a fast anomaly in the top of the lower mantle. In order for it to be sampled on by *S660S* and not *SS* (Figure 3-S8D) it would have to have a small lateral extent, which is inconsistent with the width of the *660* depression in Figure 3-2, and it would have to be very strong in order to produce enough time difference.

We conclude that it is unlikely that the inferred topographies are all due to trade-offs with (incorrect) wavespeeds in the background medium. Some trade-off is likely to occur, however, and the values of depth variations (and the inferred temperature perturbations) given in the main text should be considered an upper estimate of the true values.

Appendix 3.3.5: Robustness of images

Cao *et al.* investigated the effect of noise, interfering seismic phases, and multiple scattering near source of receiver, and reverberations within the transition zone. They also conducted an experiment with synthetic data to demonstrate that the data considered in that study was sufficient to resolve complex discontinuity structures. To obtain at least a quantitative assessment of uncertainty and resolution, we have – for the line of section presented in Figure 3-2 – estimated confidence levels by means of a bootstrap analysis. For this purpose we conducted the inversion on 10 data sets (of the same size) produced by sampling with replacement of the original data, and then estimating standard deviations. The results for 1σ and 2σ are shown in Figure 3-S9. At 1σ (~68%) confidence, all anomalies are robust (Figure 3-9A) but at 2σ (~95%) confidence one begins to see the effects of poor data coverage west of Hawaii (Figure 3-S6C,F). In particular, the short wavelength variations in depth to the *520* between 196-202° and the eastern part of the deep *660* (between 186-197°) in Region III are robust at 68% (1σ) but not at 95% (2σ) confidence level.

Appendix 3.4: Temperatures near 410 and 660 km depth

Because the depth to the post-spinel transition is relatively insensitive to composition (see above, Appendix 3.2), we use the Clapeyron slopes to estimate temperature at the parts of the transition that we interpret as the post-spinel transition. Based on experimental results, changes in Al and/or Fe content within the reasonable level for the mantle could not deepen the post-spinel boundary sufficiently to explain the observed depth (~700 km) of the 660 discontinuity in region III for plausible temperatures. Estimating temperatures from the depth to the post-garnet transition is more difficult because of the effect of aluminum (and, potentially, iron) on the transition pressure (see above, appendix 3.2).

For a given Clapeyron slope we can convert the topographic maps presented in Figure 3-6A, B to maps of temperature variations near 410 and 660 km depth in the mantle transition zone (Figure 3-S10). For this we assume that the pressure-temperature relationships are linear and that the Clapeyron slopes are constant and independent of temperature. For the olivine to wadsleyite transition (near 410 km depth) we use a slope of +2.5 MPa/K (*Morishima et al., 1994*) and for the ringwoodite to Mg-perovskite + ferropericlase (post-spinel) transition we consider three different values (-1, -2, and -3 MPa/K), but the themperature estimates given in the main text are for a post-spinel slope of -2.7 MPa/K (*Irifune et al., 1998*). The slope for post-garnet is uncertain (see previous section) and no attempt was made to produce a geographical map of temperature variations based on this transition.

Figure 3-S10A reveals that the temperature near the top of the transition zone is higher-than-average east of Hawaii, north and northwest of Hawaii, and, in particular, far west of Hawaii, roughly between 180° and 195°E, where we estimate the temperature near 410 km depth to be up to 250K hotter than average. Near the base of the transition zone the uplift of the post-spinel boundary suggest thermal anomalies of 80-240K east of Hawaii (for the largest and smallest slopes,

respectively) and from 260-800K west of Hawaii (between 197 and 204°E). In this region, a slope of -2.7MPa/K yields a thermal anomaly of ~300K.

Even further west, between 180° and 195°E, the *660* is anomalously deep, and interpretation of a deep post-spinel transition would suggest temperatures of at least 500K (for a slop of -3 MPa/K) and up to 1600K colder than average (for a slope of -1 MPa/K). A slope of -2.7 MPa/K would yield temperatures that are up to 700 K lower than average. Such anomalies, and the implied lateral temperature gradients, are implausible given the large distance of the study area to known (active) plate boundary processes (such as subduction of oceanic lithosphere).

Appendix 3.5: Ponding and and secondary upwellings

Mantle upwellings readily produce 'pancaking' – or 'ponding' – in media with depth dependent viscosity and an endothermic phase transition (*Cserepes and Yuen, 2000*). Figure 3-S11 displays a snap-shot of numerical modeling carried out using the CitcomCU code with Newtonian rheology. The code has the ability to take into account of the latent heating from phase changes and from adiabatic and viscous heating. This calculation considered isochemical convection for incompressible fluids with depth- and temperature-dependent viscosity, as well as depth-dependent thermal expansivity. For depth- and temperature-dependent viscosity, the non-dimensional viscosity is given by:

$$\eta(T,r) = \eta_r \exp\left(A(1.0 - T)\right)$$

where η_r is 1/30 between 100 km and 670 km depths and 1 otherwise, and $\boldsymbol{A}$ is the non-dimensional activation energy (here, A=6.90776, which gives rise to 10^3 viscosity variations from the surface to CMB). The temperature T is normalized with respect to the temperature contrast across the cell. The calculation domain is a two-dimension rectangle of equal height and width. The surface and CMB are isothermal and free-slip, while thermally insulating and free-slip boundary conditions are used for the

side boundaries. The density jumps across *410* and *660* are both 7.8%, and the Clayperon slopes are +3 MPa/K for *410* and -3 MPa/K for *660.* The width of both phase transitions is set to be 3.5 km.

With these parameters, ponding near the endothermic phase changes and one or more secondary upwellings rising from it to the surface are readily produced. Our imaging results and interpretation in terms of post-spinel and post-garnet transitions, call for flow simulations across an interface with lateral variation of the dominant phase transition systems (and different signs of the associated Clapeyron slopes) across a hot mantle region. This is a target of future research.

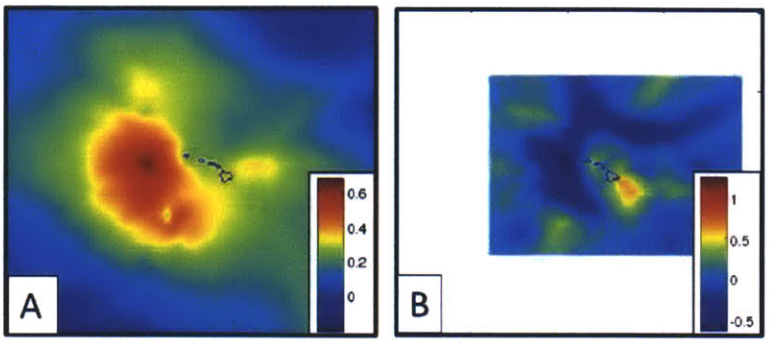

Figure 3-S1(3-5). Tomographically inferred wavespeed variations near 700 km depth beneath Hawaii. (A) P speed variations from global travel time tomography (*Li et al., 2008*), (B) S speed inferred from travel times from an array of land and seafloor seismographs on and around Hawaii (*Wolfe et al., 2009*). The range (in % deviation from the reference model used) is given in lower right corner of each panel.

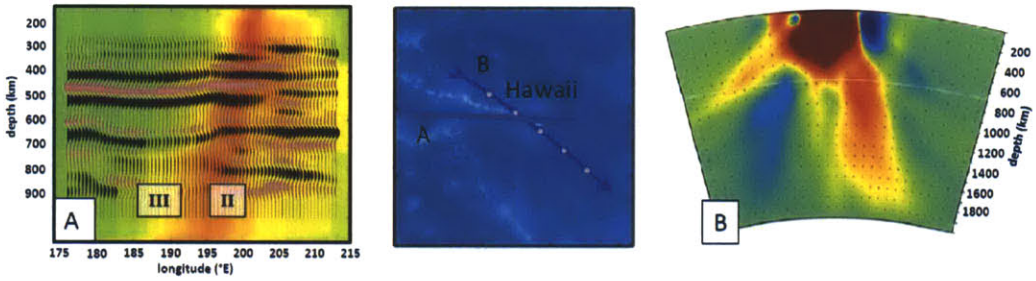

Figure 3-S2(3-6). Vertical mantle sections (A) through a global P-wave model (*Li et al., 2008*) superimposed on the seismic section of Figure 3-2 and (B) a regional S wave model (*Wolfe et al., 2009*). Difference in location and orientation of the low wavespeed anomaly are mostly due to the use of different data sets and illustrate the non-uniqueness of tomographic models in this region. In (A) a plume-like low wavespeed anomaly coincides with region II, where *660* is shallow and *520* deep. Resolution in down-dip direction is poor, however, and mantle structure further away from Hawaii (for instance region III, where *660* is anomalously deep) is not well sampled by the P data used by (*Li et al., 2008*). In (B) the lower mantle slow anomaly occurs near what we refer to as region I.

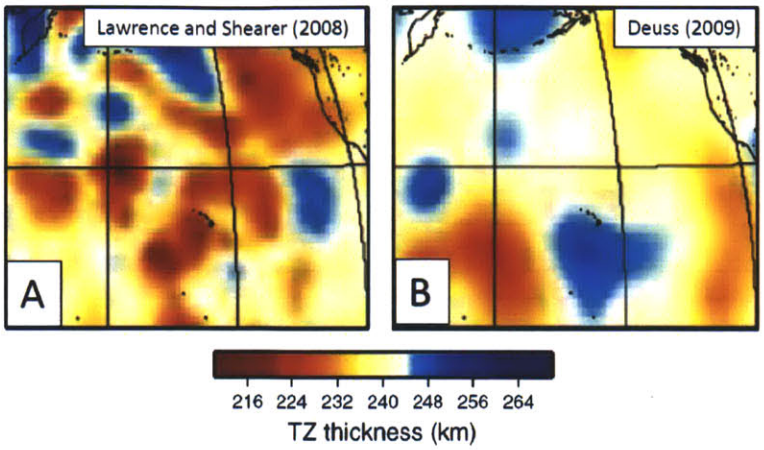

Figure 3-S3(3-7). Comparison of transition zone thickness inferred from regional stacks of *SS* precursor data for studies (*Lawrence and Shearer, 2008; Deuss, 2009*) using different data selection criteria, processing (e.g., frequency windows, corrections for mantle heterogeneity), bin size, and sensitivity kernels (e.g, ray theory or finite frequency kernels).

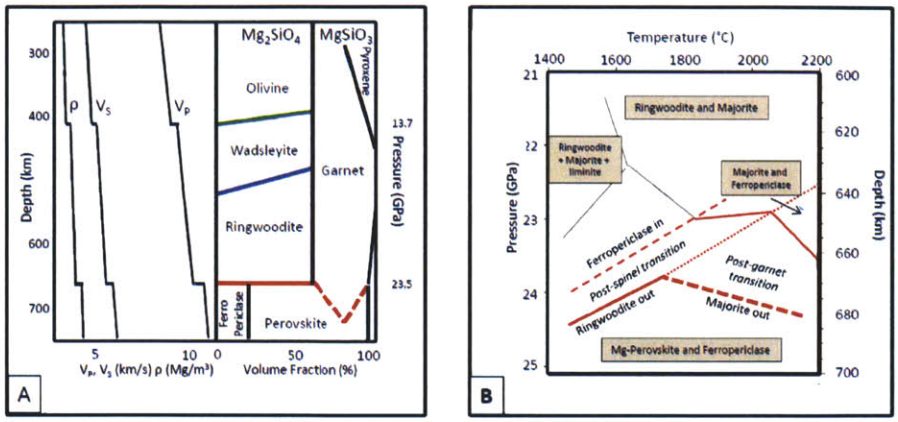

Figure 3-S4(3-8). Phase diagrams for pyrolitic mantle composition. (A): Left, *P*- and *S*-wavespeed (and mass density ρ) as function of depth in Earth's mantle between 200 and 800 km depth according to reference Earth model *ak135* (*Engdahl et al., 1998*). Right: Volume fraction of the main mantle constituents. The olivine system comprises ~ 60% of the volume fraction, with phase transitions from olivine to wadsleyite near 13.7 GPa (associated with the 410 km discontinuity in *ak135*), wadsleyite to ringwoodite near 16-18 GPa (that is, around 520 km depth), and ringwoodite to perovskite + ferropericlase near 23.5 GPa (near 660 km depth). The remaining 40% of the volume fraction concerns silicates in the pyroxene and garnet system, with the post-garnet transition occurring up to ~730 km depth (NB Al enrichment will stabilize garnet; in basalt, for instance, the post-garnet transition could be as deep as 800 km). (B) (After *Deuss et al., 2006; Houser and Williams, 2010*): Schematic phase relationships in olivine and garnet systems near 600 to 700 km depth. Between 1400 and 1700°C Mg-perovskite forms from the post-spinel transition (negative Clapeyron slope) over a narrow depth interval. At temperatures in excess of 1800°C Mg-perovskite forms over a wider depth interval from the breakdown of majorite garnet (positive Clapeyron slope). However, the thickness of the transition can be significantly decreased by partitioning of Al. Ca-perovskite is also present in all phase fields.

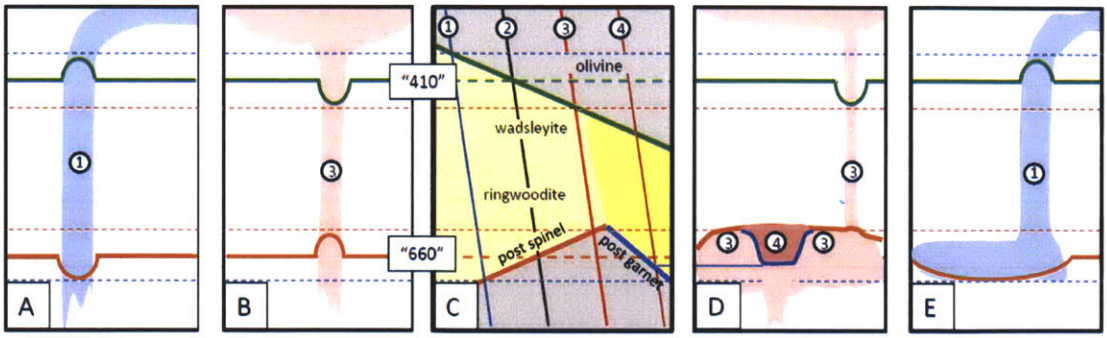

Figure 3-S5(3-9). Relationships between trajectories of mantle flow and depths to mineral phase boundaries. Left: in vertical cold slabs (A) or hot plumes (B) the depths to the *410* and *660* km discontinuities are anti-correlated because of opposite Clapeyron slopes (Γ) of the olivine-wadsleyite and post-spinel transitions (C). Center: relevant phase transitions in pyrolite (see also 3-S3). Green line depicts the olivine to wadsleyite transition ($\Gamma>0$), orange the post-spinel transition (ringwoodite to perovskite and ferropericlase; $\Gamma_{p\text{-}sp}<0$), and blue the post-garnet transition (majorite to Mg-perovskite; $\Gamma_{p\text{-}gt}>0$). The average geotherm (②) yields transitions near reference depths of 410 and 660 km; higher temperatures (③) deepen the *410* and elevate the *660*; and at even higher temperatures (④), post-garnet transitions may form the main (seismic) contrast. (See also 3-S3 of the Supplementary Materials.) Right: Deflection of hot upwellings (D) or subducted lithospheric slabs (E) increases the wavelengths of depth variations of the *660* compared to the *410* and destroys the correlation between them. In (D) the temperature may locally become high enough (in ④) to make post-garnet the dominant phase transition.

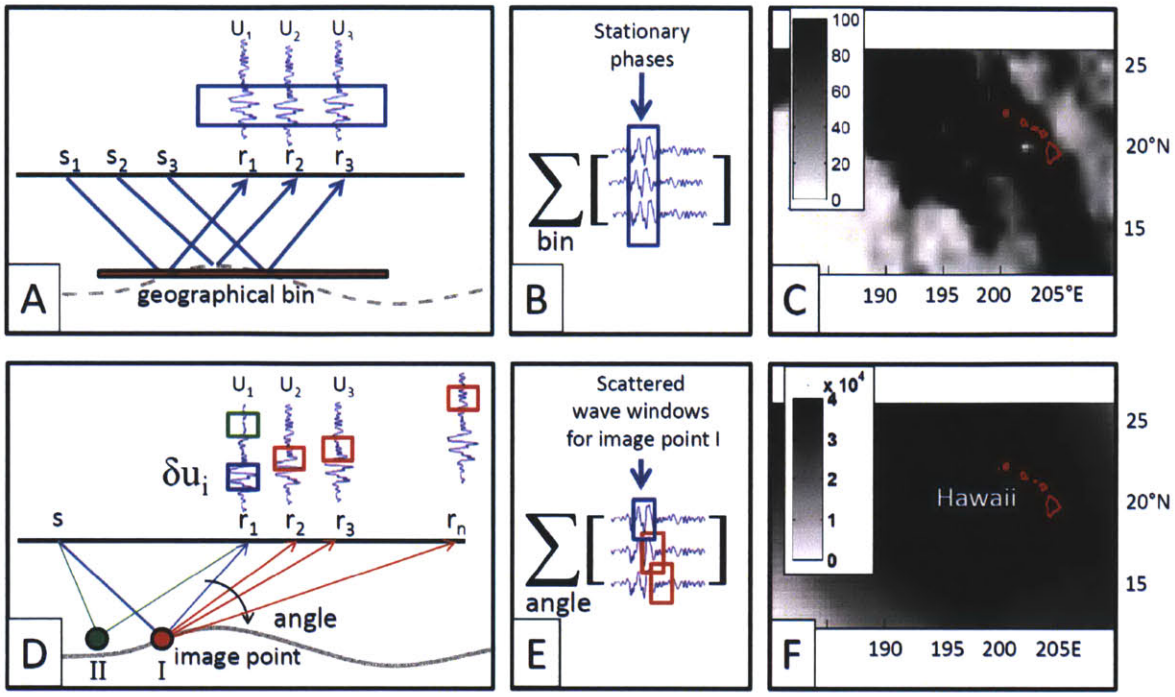

Figure 3-S6(3-10). Illustration of the main differences between traditional stacking over geographical bins (A-C) and inverse scattering, which involves integration of data windows that sample a single image point from different directions (D-E). (A) Common midpoint reflections in a geographical bin (red bar) over which depth and elastic properties of interface are assumed constant. Any topography (gray dashed line) will be averaged over bin. (B) Stacking or averaging over midpoints in a bin of displacement records (u_i) after move out correction. (C) Geographical distribution in study region of *SS* midpoints in study region. The sampling that can be used with this method is very uneven and degrades rapidly in NE and SW directions away from Hawaii. (D) Depending on offset, waves scattered at image point (I) arrive can arrive close to the main phase (blue box) or in the coda after the main arrival (red boxes). Vice versa, data in the blue and red windows contain information about scattering point I. No assumption is made about the lateral extent of reflectors. Green lines are non-specular paths from image point II, away from a reflector, and the associated signal (green box) is small. (E) Signal from image point I is enhanced by stacking (integration) over all data windows that contain information about that same image point and which sample the image point from different directions. This can include data associated with specular reflections (blue ray/box) as well as non-specular scattering (red rays/boxes). (F) Geographical distribution of the number of data windows δu that contribute to image gathers (Figure 3-S5) at the 0.5°x0.5° (lat, lon) grid. The sampling that is exploited by inverse scattering is spatially much more evenly distributed than the sampling of SS bounce points (panel C).

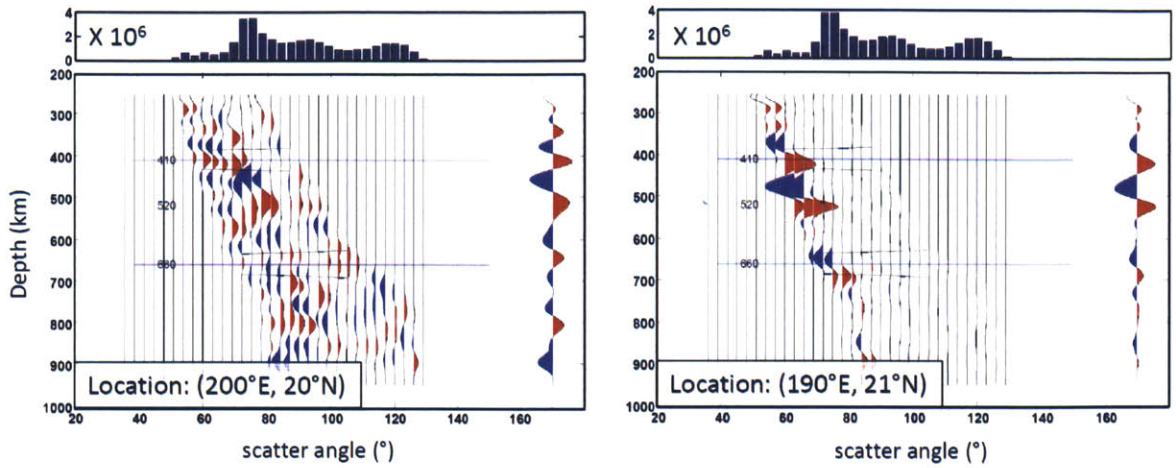

Figure 3-S7(3-11). Image gathers for a point in region II (200°E, 20°N), left, and region III (190°E, 21°N), right. Reflectivity profiles for the same image point are calculated for a range of scatter angles (see *Cao et al., (2010)* for definitions and more detailed descriptions) and the stack of these common image point gathers produces the GRT image shown on the right. The histograms at the top of each image gather indicate the number of data samples (δu) that are used for the calculation at each scatter angle. The total number of seismic traces used for the construction of the GRT image (or radial reflectivity profile) at each (lon, lat) grid point is contoured in Figure 3-S6F.

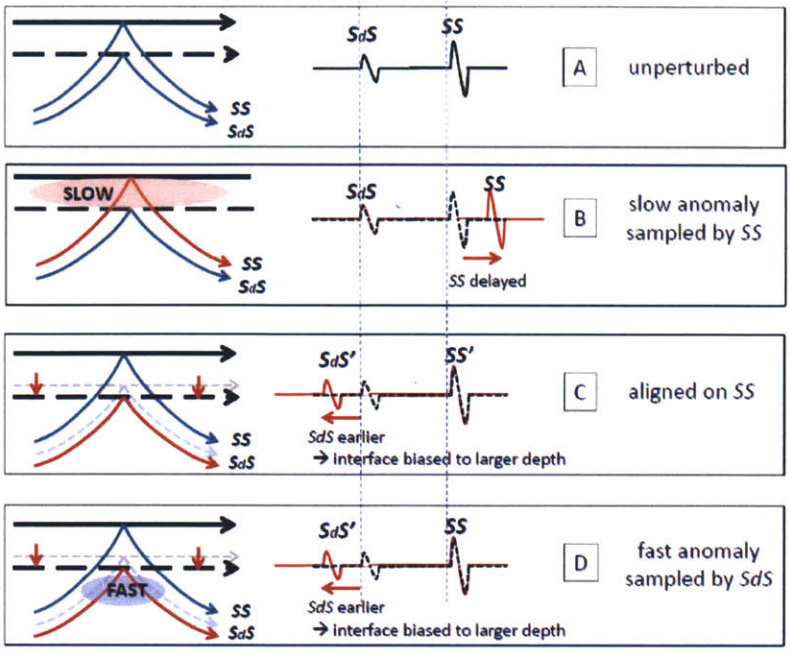

Figure 3-S8(3-12). Trade-off between volumetric wavespeed and imaged interface depth for the case of imaging with *SS* precursors and alignment on *SS*. (A) Unperturbed reference situation. (B) Upper mantle wavespeeds that are slower than in the 1- and 3D models used could lead to overestimation of interface depths after alignment on *SS* (C). A fast anomaly below the interface of interest could also lead to overestimation of interface depth (D). These effects can explain some pulse distortion (e.g. minor "splitting") but not, for realistic wavespeed perturbations, the large depth variations inferred in our study.

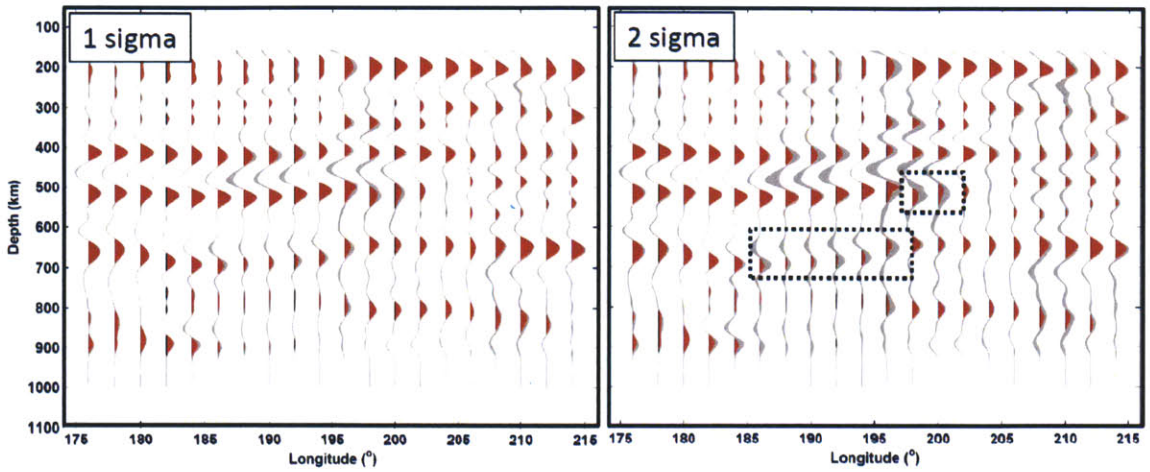

Figure 3-S9(3-13). GRT image profiles for latitude 20° (red) and the 67 % (1 σ) and 95% (2 σ) confidence level (gray shading around the image profiles). The confidence level at each image point is calculated by bootstrap method by sampling with replacement of the original dataset.

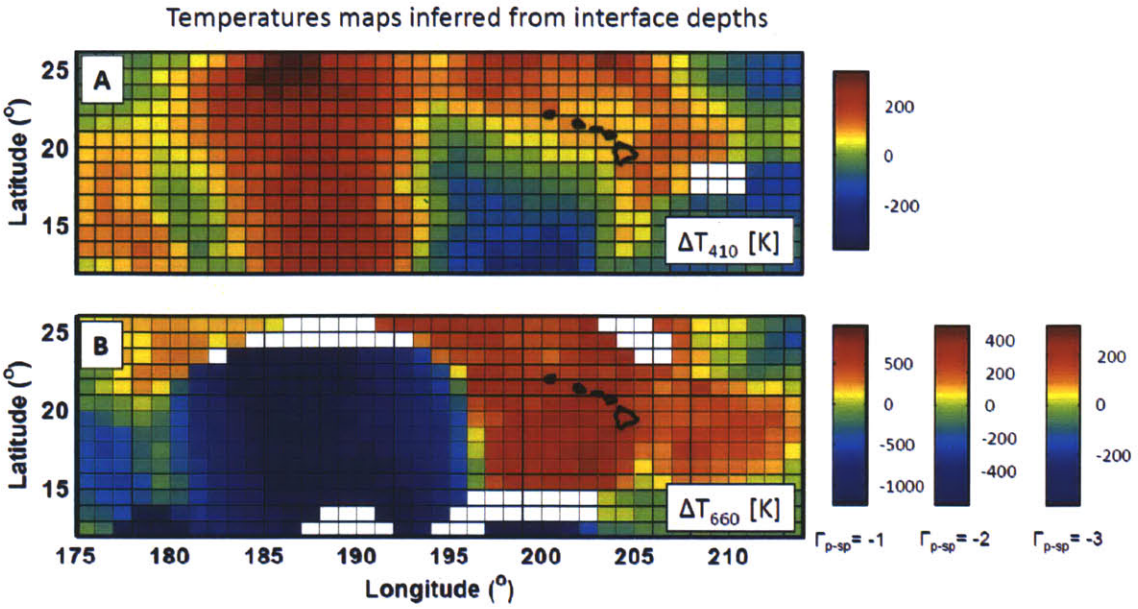

Figure 3-S10(3-14). Temperature maps at the top of the mantle transition zone (A) and the top of the lower mantle (B) inferred from the depth variations of the *410* and *660* km discontinuities as imaged with inverse scattering of *SS* waves (Figure 3-4A, B). For the depth (or pressure) to temperature variations we use Clapeyron slopes of +2.5MPa/K for the *410* and values from -1 to -3 MPa/K for the *660.* In view of uncertainties in phase relations and effects of composition (in particular aluminum content) on Clapeyron slope and relative depth of the post-garnet transition we only show temperature maps for data based on the olivine system.

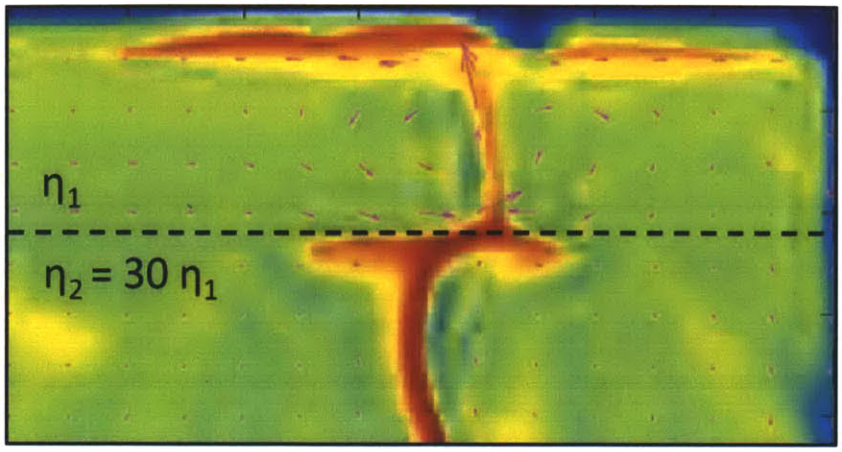

Figure 3-S11(3-15). Snapshot of numerical simulation of convective flow from high to low (Newtonian) viscosity across an endothermic phase change (dashed line). The viscosity and mass density contrasts at the dashed line are η_2/η_1=30 and 7.8%, respectively, and the Clapeyron slope is -3 MPa/K. This modeling was part of collaborative research with B. H. Hager at MIT, and the numerical code CitcomCU was generously made available by S. Zhong at University of Colorado, Boulder.

Chapter 4

Geodynamical modeling of plume interaction with the mantle phase transitions

Abstract

The dynamic evolution of mantle plumes is studied in a mantle with an exothermic phase change at 410 km depth and an endothermic phase change at 660 km depth. Both zero and nonzero dissipation numbers are considered. In the modeling process, plumes can start spontaneously from the core-mantle-boundary (CMB), with different strengths. Our modeling reveals a variety of plumes that are different from the traditional mushroom type plume. Due to the effect of the endothermic phase change at 660 km depth the horizontal scales of the topography of the 410 km and 660 km phase boundaries can be different so that simple anti-correlation between the topographies no longer exists. Our results suggest complex material exchange and heat transfer process across the 660 km phase boundary, which might imply that geochemical trends in hotspot surface lavas cannot constrain lower mantle domains directly.

4.1 Introduction

The mantle plume hypothesis was proposed in 1970s to explain hotspots at the Earth's surfaces, which are characterized by higher temperature, topographic swells, and massive volcanism, such as Hawaii (*Morgan, 1972*). The hypothesis proposes that hot mantle upwellings in the form of cylindrical conduits, which are named "mantle plumes", may rise up all the way from the core-mantle boundary

(CMB) and lead to the observed age-progression of the seamounts as the plates moves by. Numerical simulations of the Earth's mantle convection show that hot upwellings can form naturally from thermal boundary layers (e.g. CMB) as a result of Rayleigh-Taylor instabilities. With support from both numerical simulations and lab experiments (*Sparrow et al., 1970; Whitehead and Luther, 1975; Olson and Singer,1985; Griffiths and Campbell ,1990; Albers and Christensen, 1996; Farnetani,1997*), mantle mantle plumes have been widely invoked to explain flood basalts on the earth's surface, the isotopic signature of ocean island basalts, the topography of the swells and plateaus that often accompany volcanic hotspots, although there are still debates about the existence of plumes (*Anderson, 2000*).

In the canonical models, a plume is pictured as a thin cylindrical upwelling of hot materials with a mushroom-shaped head, rising from the core mantle boundary (*Morgan, 1972; McKenzie et al., 1983; Allegre et al., 1985*). However, in global seismic tomography, undisputed evidence for plume-like slow velocity anomalies extending from lithospheric depths into the lowermost mantle is still lacking. This might be caused by the fact that imaging the presumed long narrow structure of mantle plumes may fall beyond the resolving power of traditional seismic tomography (*Nataf, 2000*). But recent geodynamic modeling studies show that, in more realistic Earth's model, plumes may not look like what is described in the classical "mushrooom" shape model (e.g. *Tackley et al., 1993, 1994; Courtillot et al., 2003; Steinberger and O'Connell, 1998, 2000; Steinberger, 2000; Antretter et al., 2002, 2004; Tarduno Tarduno et al., 2003; Steinberger et al., 2004; O'Neill et al., 2003, 2005; Steinberger and Antretter, 2006*). First, the plumes will interact with the phase boundaries, in particular, the ringwoodite to perovskite and magnesiowustite (or ferropericlase) phase transition at around 660 km depth. This phase transition is endothermic (*Ito and Takahashi, 1989*) and is expected to have a strong inhibition effect on on the mass flux across 660 km depth, that is, it tends to inhibit hot materials like plumes from rising up and cold materials like subducted slabs from penetrating down (see *Christensen (1995)* for a review). This inhibition might produce ponds of hot materials spreading beneath the 660 km phase

boundary (*Samuel and Farnetani, 2003; Tackley, 2008*). Second, plumes may be tilted and distorted by the large-scale convection in the mantle. So the location where we observe the hotspot might not be the location of plume root in the deep mantle (*Steinberger, 2004; Tarduno, 2009*). All these studies picture the plumes in different and more complicated ways than simple head-and-tail mushroom shape model. On the other hand, simple mush-room type models of plume are widely used to interpret the chemical and isotopical heterogeneity of hotspot lavas (*Farnetani and Hofmann, 2009; Blichert-Toft et al.,2003*).

If one wants to study plume dynamics in realistic Earth's mantle environment, the effect of the phase transitions cannot be ignored. Upper mantle phase transitions have long been recognized to play an important role in mantle convection (*Gurnis and Hager, Nature, 1988; Machetel and Weber,1991; Tackley et al., 1994; Honda et al., 1993; Solheim and Peltier, 1994*). Two of the most important phase transitions, olivine to wadsleyite at around 410 km (referred to as the 410 discontinuity in seismology) and ringwoodite to perovskite and magnesiowustite (or ferropericlase) at around 660 km (referred to as the 660 discontinuity in seismology) have Clapeyron slopes of opposite signs. The 410 discontinuity is exothermic and hence has positive Clapeyron slope, that is, larger pressure (deeper depth) for higher temperatures; 660 discontinuity is endothermic and hence has negative Clapeyron slope, that is, smaller pressure (shallower depth) for higher temperature (*Bina and Helffrich, 1994*). During the phase change from low pressure phase to high pressure phase, heat will be released at the 410 km discontinuity, but will be absorbed at the 660 km discontinuity. An endothermic phase change tends to retard motions across this phase transition in a convecting mantle, while an exothermic phase change will facilitate material exchanges across the phase boundary. Many seismology and geodynamical modeling studies have been devoted to investigate whether or not subducted lithospheric plates can penetrate through the mantle transition zone at around 660 km. It is now widely accepted that this endothermic phase transition can result in periodic piling up of cold slabs and intermittent penetration at 660 km depth in the Earth's mantle (*Christensen and Yuen, 1984; Zhong and Gurnis, 1995; Van der Hilst et al., 1991*).

The interaction of hot upwellings (i.e. plumes) with phase transitions does not seem to have profound influences on the global convection pattern (*Tackley, 1993, 1994*). However, this interaction is important for the studies of the plumes themselves, their surface expression at hotspots, and the associated geological and geochemical processes. Numerical studies have been performed to study the interaction of plumes with phase transition, using more and more realistic physical assumption about the Earth, such as depth-dependent viscosity and thermal expansivity and temperature dependent viscosity (*Nakakuki et al., 1994; Steinbach and Yuen, 1997; Davies, 1995; Schubert et al., 1995*). Modeling suggests that for low Rayleigh numbers, the endothermic 660 phase boundary is partially penetrable for hot upwellings (*Nakakuki, 1994; Davies, 1995*). Some studies report that a 'second asthenosphere' may develop under 660 km phase boundary, which may give rise to 'mid-mantle plumes' ascending from the 660 km phase boundary (*Cserepes and Yuen,2000*). Courtillot et al. (2003) identified three types of hot spots: (1) primary hot spots, which are hot spots resulting from a single, narrow plume that origins from deep lower mantle; (2) secondary hot spots, originating from the top of a large scale hot province, so-called "plume farms", which is often observed to be lying underneath the 660 km phase transition in numerical simulations (Sleep, 1990; Clouard and Bonneville, 2001), and (3) tertiary hot spots of lithospheric origin.

In recent years, progress has been made in seismology (Shearer *and Masters, 1992; Shearer, 1993; Gossler and Kind, 1996; Flanagan and Shearer, 1998; Gu et al., 1998; Flanagan and Shearer, 1999; Gu and Dziewonski, 2002; Lebedev and van der Hilst, 2002, 2003; Chambers et al., 2005a, b; Deuss et al., 2006; Deuss, 2007; Schmerr and Garnero, 2006; An et al., 2007; Rost and Thomas, 2009*) with constraining the topography of phase boundaries, e.g. the 410 km and 660 km discontinuities, which can be used to constrain the local temperature profiles and hence infer the existences and origin of mantle plumes. This also provides the opportunity to compare geodynamic plume models with seismic images of transition zone beneath hotspots in order to constrain the Earth's properties. Geodynamical

modeling can provide important insight into the morphologies and dynamics of the plumes, which will help the detection of plumes in seismic images (e.g. transition zone discontinuity topographies). At least we need to have an idea of what a plume should look like in order to identify the possible plume-related signatures in seismic images. On the other hand, given a qualitative plume model, seismic observations may help identify implausible parameter spaces in geodynamical modeling and put further constrains on important properties of mantle convection.

In **Chapter III** of this thesis (also published in *Science, 332, 1068-1071, 2011*), we present 1°×1° topography maps of 410 and 660 km phase boundaries underneath an 40°×15° area surrounding the Hawaii hotspot. Using a recently developed high-resolution seismic imaging technique, the generalized Radon transform, we can detect the lateral variations of the phase boundary topographies at the scale of several hundred kilometers, which is comparable to the diameter of the presumed plume conduit (*Nataf, 2000*). Our seismic images show that, the lateral scale of the 660 km phase boundary topography, is several times that of the 410 km phase boundary topography. Also, the geographic location where we observed the largest depression of the 410 km phase boundary (which indicates hot thermal anomaly) is not the location where we observed the largest uplift of 660 km phase boundary. These features of the 410 and 660 km phase boundary topographies cannot be explained by the existence of a canonical mushroom type plume directly underneath the Hawaii hotspot.

In this Chapter, we simulate the evolution process of mantle plumes in a realistic mantle environment (that is, with ambient mantle flows and without fixing the heat source at Core-Mantle Boundary), with emphasis on the interaction between plumes and the phase transition. We will discuss the seismic expression of mantle plumes on the phase boundary topographies, as well as other general properties of plumes, such as the morphology and temperature of plumes. In fact, much of the ambiguity in the interpretation of the seismic images for possible plumes has its root in answering the basic question: what should a deep-rooted mantle plumes look like? Most of the previous geodynamical

studies of plumes invoked a heated patch to trigger plume initiation, even if the existence, the location, size, and strength of such a presumed patch is unknown. Here we take a different approach: first, we let the convection program run until it has reached a quasi-stationary state. Second, we amplify a selected spontaneous plume from a quasi-stationary state by multiplying its temperature with a range of different factors in order to create plumes of different strength. Third, we let our amplified plumes rise in a mantle wind induced by setting the initial temperature environment to be a quasi-stationary state, and we observe how the plumes evolve and, especially, how they interact with the phase boundaries. We hope that by moving beyond the traditional assumptions and experiment settings we obtain more realistic pictures of plume dynamics so that we can bridge the gap between geodynamically consistent plume models and the plume images (or their thermal imprints on phase boundaries) inferred from seismology.

4.2 Mathematical description

The governing equations for thermal convection in an incompressible fluid with an infinite Prandtl number include the equations for conservation of the mass, momentum and energy. There will be additional terms introduced by the inclusion of phase transitions in the equations. In the conservation of momentum equation, buoyancy forces arise both from density differences due to thermal expansion and from density differences from phase transitions. Also in the conservation of energy equation, latent heating released by phase transitions should be included. So we need a consistent way of modeling the percentage of phase changes at certain pressure and temperature. The following formulation for phase transitions is adapted from *Christensen and Yuen (1985)*, and follows the same nondimensionalization of *Leng and Zhong (2008)*.

First we define a phase function Γ. Γ describes the relative fraction of the heavier phase and hence should take values between 0 and 1. It is a function of pressure p and temperature T. Γ = 1 means it only contains the heavier phase and Γ = 0 means it only contains the lighter phase. We take Γ = 0.5 at the transition pressure p_t determined from mineral physics experiments, which depends on the temperature T via the Clapeyron slope γ. With p_0 the zero-degree transition pressure, we write:

$$p_t = p_0 + \gamma T .$$

Then we define the "excess pressure" π by

$$\pi = p - p_t = p - p_0 - \gamma T ,$$

and take Γ as a function of π:

$$\Gamma(\pi) = \frac{1}{2}\left(1 + tanh\frac{\pi}{\rho_0 g w}\right),$$

where w is defined as the width of the phase transition; ρ_0 is the reference density at T=0.

To determine the buoyancy force, we need the density profile taking into account the effect of phase transition, which can be determined according to

$$\rho = \rho_0\left(1 - \alpha T + \frac{\Gamma\Delta\rho_{ph}}{\rho_0}\right),$$

where α is the coefficient of thermal expansion and $\Delta\rho_{ph}$ is the density contrast between two phases.

Next we need to incorporate latent heating of phase transitions in our energy conservation equation. The total latent heating per unit mass released in the process of phase change is:

$$q_L = \gamma\frac{T\Delta\rho_{ph}}{\rho_0^2}.$$

The latent heat released per unit volume during the transition is given by

$$Q_L = \rho_0 q_L \frac{D\Gamma}{Dt},$$

where $D/Dt = \partial/\partial t + u_i\,\partial/\partial x_i$ is the material derivative.

The energy conservation equation is as follows:

$$\rho_0 T\frac{DS}{Dt} = \frac{\partial}{\partial x_i}\left(k\frac{\partial T}{\partial x_i}\right) + \tau_{ij}\frac{\partial u_i}{\partial x_j} + \rho_0 H\,.$$

Using the thermodynamic relations between *S*, *T* and *P*, and plugging q_L into the representation of Q_L, the energy conservation equation can be modified as:

$$\rho_0 C_p\frac{DT}{Dt} - \alpha T\frac{Dp}{Dt} - \frac{\gamma T\Delta\rho_{ph}}{\rho_0}\frac{D\Gamma}{Dt} = \frac{\partial}{\partial x_i}\left(k\frac{\partial T}{\partial x_i}\right) + \tau_{ij}\frac{\partial u_i}{\partial x_j} + \rho_0 H\ ,$$

where τ_{ij} is the deviatoric stress tensor and u_i are the velocity components. *H* is the internal heating per unit volume. C_p is the specific heat at constant pressure.

We non-dimensionalize the equations with the following characteristic values:

$$x_i = dx_i',\quad u_i = \frac{\kappa_0}{d}u_i',\quad T = \Delta T T' + T_s,\quad T_s = \Delta T T_s',\quad \rho = \rho_0\rho',$$

$$t = \frac{d^2}{\kappa_0}t',\quad H = \frac{H'\kappa_0\Delta T C_{p\_0}}{d^2},\quad \eta = \eta_0\eta',\quad p = \frac{\eta_0\kappa_0}{d^2}p',\quad \alpha = \alpha_0\alpha',$$

$$C_p = C_{p\_0}C_p',\quad k = k_0 k',$$

where symbols with primes are dimensionless; $d, \kappa_0, \Delta T, T_s, \rho_0, t, \eta, \eta_0, \alpha_0, g_0, C_{p\_0}, k_0$ are mantle thickness, reference thermal diffusivity, temperature contrast across the cell, surface temperature, reference density, time, viscosity, reference viscosity, reference coefficient of thermal expansion, constant of gravity, reference specific heat at constant pressure, and reference thermal conductivity, respectively. The reference thermal diffusivity is defined as

$$\kappa_0 = k_0/(\rho_0 C_{p\_0})\ .$$

The dimensionless governing equations are as follows:

$$(u_i)_{,i} = 0\,,$$

$$-p_{,j}\delta_{ij} + \tau_{ij,j} - Ra\left(1 + P\frac{d\Gamma}{d\pi}\right)T\delta_{i3} = 0\ ,\text{and}$$

$$\left(1 + Di\frac{P^2}{R_\rho}\frac{d\Gamma}{D\pi}\right)\frac{DT}{Dt} + \left(1 + P\frac{d\Gamma}{d\pi}\right)DiTu_3 = -\nabla^2 T + \frac{Di}{Ra}\tau_{ij}u_{i,j} + H\,,$$

where $Ra = \alpha g \rho_0 \Delta T h^3 / k_0 \eta_0$ is the Rayleigh number; $Di = \alpha g h / C_p$ is the dissipation number; $P = \Delta \rho \gamma / \rho^2 \alpha g h$ is the phase boundary number; $R_\rho = \Delta \rho / \rho \alpha \Delta T$ is the density ratio.

4.3 Model Setup

We only consider isochemical thermal convection for incompressible fluids with depth- and temperature-dependent viscosity, as well as depth-dependent thermal expansivity. The relevant parameters are given in Table 1. Our calculation domain is a two-dimensional rectangle of equal height and width. The surface and CMB are isothermal and free-slip, while for side boundaries we use thermally insulating and free-slip boundary conditions. Thermal expansivity decreases by a factor of 5 from surface to the CMB. Our model has the ability to take into account of latent heating from the phase changes, adiabatic heating, and viscous heating. For depth- and temperature-dependent viscosity, the non-dimensional viscosity is given by:

$$\eta(T, r) = \eta_r \exp\big(A(1.0 - T)\big),$$

where η_r is 1/30 between 100 km and 660 km depths and is 1 otherwise, A is the non-dimensional activation energy. For this study, A = 6.90776, which gives rise to 10^3 viscosity variation from the surface to CMB.

The system of partial differential equations is solved with a finite element code CitcomCU (*Moresi and Gurnis, 1996; Leng and Zhong, 2006*). The numerical grid is refined near the thermal boundary layers. In this study we start the plumes in a "steady" state of the mantle. For high Rayleigh number convection, a time-invariant steady state does not exist, so we are aiming at statistically steady state over time (quasi-stationary state or stationary state, for short). We start the convection with some random perturbation imposed on linear temperature distribution with depth, and we then run over 50,000 time steps until the model reached the stationary state. Subsequently, we pick a plume that just

rose spontaneously from the CMB in a stationary state and multiply the temperature field in the plume with different coefficients P in order to simulate plumes of different strength. Finally, we start the convection again and our amplified plumes keep rising, but with higher temperatures. In this way we can introduce the influence of the ambient mantle convection in studying the evolution of plumes. The quasi-stationary state consists of piling of subducted slabs above 660 km discontinuity and big overturns caused by the avalanches of the piled slabs. This will cause long-term drifts between smaller and larger upper/lower mantle temperature contrast. We will investigate two end member cases in the following section.

Table 1. Physical Parameters and Constants

Quantity	**Symbol**	**Value**
Rayleigh number	Ra	1×10^6
Mantle thickness	d	2800 km
Surface thermal expansivity(coefficient of thermal expansion)	α_0	$5\times 10^{-5}/K$
Thermal diffusivity	κ_0	10^{-6} m^2/s
Density	ρ	3300 kg/m^3
Specific heat	C_p	1200 $J/(kg\bullet K)$
Gravitational acceleration	g	9.8 m/s^2
Surface temperature	T_s	273 K
CMB temperature	ΔT	2300 K
Olivine-spinel phase change		
Clayperon slope	γ_1	$3MPa/K$
Density change	$\Delta\rho_{ph1}/\rho$	7.8%
Phase transition width	w_1	3.5 km
Spinel-Pervoskite phase change		
Clayperon slope	γ_2	-3 MPa/K
Density change	$\Delta\rho_{ph2}/\rho$	7.8%
Phase transition width	w_2	3.5 km

*Thermal expansivity decreases by a factor of 5 from the Earth's surface to the CMB.

4.4 Results

4.4.1 Primary plume and Secondary plume

First we study a typical example, with a starting plume as shown in Figure 4-1a (initial starting time 0 Myr). The plume temperature has been multiplied by a factor of 2.0 (P=2.0). The history of the plume evolution is briefly summarized as follows, and illustrated by the snapshots shown in Figure 4-1- The heat anomaly we introduced produced large buoyancy in the cell (Figure 4-1a). The material right above the plume head had an upgoing velocity across the 660 km boundary, which means that material passed through the 660 km boundary ahead of the arrival of the plume head. The plume head continued to rise until it hit the 660 km boundary (Figure 4-1b). Because its buoyancy was high enough, part of the plume head could pass across the 660 km boundary, so we can see a secondary plume emerging right above 660 km (Figure 4-1c). The secondary plume has a structure similar to that of the primary plume, except for the plume conduit, which was about half of that in the lower mantle. This is caused by the lower viscosity in the upper mantle, which is 1/30 of the viscosity in the lower mantle in this model. (Because the difference between the plume temperature and the environment temperature is so large, the criterion we used to determine the conduit is not critical.) Due to the low viscosity, the materials tended to move faster, and hence it had smaller conduit. The hot plume created a high temperature (i.e. low viscosity) channel here. The surrounding materials at the bottom of the upper mantle began to converge to this channel and rose up. The secondary plume hit the surface and plume head spread around underneath the surface (Figure 4-1d). However, in the lower mantle, the total buoyancy of the primary plume head decreased because it lost part of the materials to the upper mantle. It stopped supplying the secondary plume when there was not enough buoyancy gathered beneath the transition zone. As a result, the plume conduit of the secondary plume became thinner and weaker (Figure 4-1e), while at the same time, the plume head of the primary plume gathers beneath the 660 km

and became larger. A new secondary plume emerged to the right of the primary plume conduit (Figure 4-1f), which might be caused by the growing buoyancy gathered underneath the 660 km, or because material in the upper mantle was heated by the primary plume head. The secondary plume diffused much faster than the primary plume in the lower mantle (Figure 4-1g), due to the lower viscosity in the upper mantle. In the lower mantle, the plume conduit diffused faster than plume head (Figure 4-1h,i), possibly because of its smaller diameter and lower temperature.

In this numerical experiment we observed two types of secondary plume. The first kind was created when the primary plume initially passed through the 660 km phase boundary. After the temperature of this secondary plume in the upper mantle decreased, there was still a layer of ponding hot materials underneath the 660 km phase boundary (Figure 4-1e). This ponding of hot materials gave rise to a new secondary plume to the right of the primary plume.

4.4.2 Comparison between different plume strengths

The scenarios when we multiplied the plume temperature by 1.2 and 1.5 are shown in Figure 4-2- When we amplified the temperature of the plume by a factor of 1.2, the plume head continued to rise and the tail of plume was lengthened. When the plume head hit the 660 km phase boundary it stopped rising and began spreading out around the center of the plume. There was a small stream of hot material (i.e. a secondary plume) rising from top of the transition zone. However, the hot anomaly became invisible before it reached the surface. The residual of the plume head stayed beneath the transition zone for long time, while at the same time, part of the primary plume conduit diffused (Figure 4-2c).

When we amplified the temperature of the plume by a factor of 1.5 the plumes rose and hit the 660 phase boundary (similar to the P=1.2 case). Then it began to spread and there was a stream of hot materials rising from the center of the plume conduit and rose all the way to the top of the surface, but

quickly diffused. The residual of the plume head also spread underneath the transition zone but it is hotter than those in the P=1.2 case (Figure 4-1f). It was also noticed that the plume conduit in the lower mantle is greatly tilted in both cases (Figure 4-1b,c,e,f), due to the existence of large scale advection in the lower mantle.

Recall that in the P=2.0 case, the rising and the hitting process of the primary plume was similar to the previous cases. But the first secondary plume, which finally reached and spread underneath the surface, was much stronger in P=2.0 case than the secondary plume in the P=1.2 and P=1.5 cases. For P=2.0 the plume conduit of the first secondary plume was at first located at the center of the primary plume and then the conduit of the second secondary plume migrated to the right of the center. The residual of the second secondary plume stayed underneath the surface while its temperature was decreasing. Meanwhile, there was still a continuous plume conduit and plume ponding in the lower mantle (Figure 4-1h,i).

4.4.3 Larger upper/lower mantle temperature contrast

Figure 4-3 shows a different plume and steady state scenario to start with. This plume is taken from a scenario when a substantial amount of cold slabs piled up above the transition zone and the slabs were about to leak into the lower mantle. So the upper mantle was colder than in the previous case. Although different starting plumes have different shapes and different starting temperature distributions, our tests (not shown here) show that the behavior of plumes are very similar if the upper/lower mantle temperature contrast is similar, no matter the size and shapes of the plumes. In this section we study the plume evolution process when the upper/lower mantle temperature contrast is large. We only show the P=2.0 case, because the plume in the other two cases (P=1.2 and P=1.5) was in essence a "weaker" version of P=2.0 case as we observed.

The processes of primary plume rising, interface interaction, and secondary plume generation were

very similar compared to the previous starting plume. However, there was no longer a larger plume head residual ponding underneath the 660 km phase boundary (Figure 4-3a,b) as in the former case with smaller upper/lower mantle temperature contrast. All the hot materials directly went through the 660 km barrier. This is because the upper mantle temperature was lower in this case, so the plume head got greater buoyancy once it hit the boundary. The buoyancy dragged all material up into the upper mantle, without leaving any hot materials ponding beneath the 660 km phase boundary. We also observe that secondary plumes tended to emerge more frequent at the edge of the smaller plume head, which we suspect is the result from the larger horizontal temperature gradient at the edge.

4.4.4 Including adiabatic cooling effect

In all of the above cases we set the dissipation number to 0. That is, we ignore the viscous and adiabatic heating in our calculations. To make the energy conservation equation consistent we also need to ignore the latent heating effect because the dissipation number is zero. Here we perform similar experiments using dissipation number (Di) 0.5.

Figure 4-4 shows several snapshots taken from the simulation. We note that the cold rings around the plume head are numerical artifacts. Because the transition from hot plume to surrounding mantle is very sharp, the finite element algorithm used here will give rise to oscillations around the plume head, which show up as the cold rings. The algorithm is robust enough to prevent oscillations from propagating, but the existence of the cold rings will cool the plume head. With zero dissipation, this effect only has minor influence on the evolution of plumes. However, if the dissipation number is large the plume temperature decreases as it ascends from the CMB, as shown later. Then the extra cooling from the numerical-artificial cold rings can greatly shorten the lifetime of plumes. So we did several resolution tests until the result does not change as we increase the resolution.

Most of the phenomena we discussed above in the zero dissipation number case (e.g., plume morphology, ponding) also occurred here. There are also some unique features owing to the inclusion of extra heating effects. The thin plume conduit dissipated quickly as the plume rose (Figure 4-4d). By the time the plume head reached the 660 km phase boundary, part of the plume conduit was almost cooled to the ambient mantle temperature. Because it was hotter than the conduit, the plume head gathered enough buoyancy to overcome the 660 km phase boundary and could thus rise to the surface (Figure 4-4e). Figure 4-5 shows the temperature of the hottest part in the plume head, with different starting temperatures. It is observed that higher temperature plumes cooled faster than lower temperature ones. In the P=2.0 case, the plume head cooled to half of its initial value. In the end, the plume head temperature with different starting temperatures all converged to almost the same value (around 1.0) at 660 km. It is not shown in this figure, but worth pointing out that as the plume came across the phase boundary there was a small temperature increase in the plume head, owing to the latent heating effect.

4.5 Implications for the interpretation of seismic images of plumes

4.5.1 Hot spot on the surface and mantle plume from deep mantle

For a long time people tended to believe that hotspots should be linked to stationary, nearly vertical mantle plumes, and that hotspots should be fixed relative to each other. Plumes have thus been used to define a reference frame for plate motions. However, our studies show that the underlying assumption may not be true in the presence of large-scale mantle convection, which confirms the findings of previous studies (*Steinberger and O'Connell, 1998, 2000; Tarduno et al., 2003; Steinberger et al., 2004; Steinberger and Antretter, 2006*). The evolution of plumes is influenced by the ambient mantle

flow. The root of plume is not necessarily right beneath the hotspot. Even without considering the plume-lithosphere interaction, the hotspot is likely to be the surface expression of the secondary plume emerging from the base of upper mantle. The lateral location of the secondary plume may not necessarily coincide with the location of primary plumes giving rise to it (some of our results show that secondary plumes re-generated by the ponding of hot materials underneath 660 km phase boundary tended to emerge from the edge of the primary plume). Also, there is a migration of the plume conduit of the secondary plume, embedded in the low-viscosity upper mantle. This extra degree of freedom makes the mapping of geochemical observation of hotspot lavas to the deep mantle geochemical reservoir indirect. In this regard it is important to know if the secondary plume was generated either by a leak of the plume head under transition zone (which means materials exchange between upper/lower mantle) or by the thermal instability at the bottom of the upper mantle caused by heating by ponding hot materials underneath 660 km. These two different possibilities will give fundamentally different geochemical interpretation for the hotspot lavas.

4.5.2 Big plume head (ponding) underneath 660 km phase boundary and implications for the topography of 660 km discontinuity

Just as subducted slabs can pile up above the 660 km phase boundary (e.g., *Van der Hilst et al., 1991; Fukao et al., 1992*) plumes may stagnate, or pond beneath the transition zone. A plume head ponding beneath the 660 km is likely to outlive the plume conduit, even when the plume is no longer connected to the surface. Also, there are weak plumes that do not penetrate the transition zone and hence do not reach the surface. In this scenario the plume heads pond underneath the 660 km phase boundary. If the plume head reaches the Earth's surface, the thin plume conduit will quickly lose heat (either owing to the ambient mantle flow or to adiabatic cooling) in the upper mantle, so it becomes invisible tomographically, while the plume head and tail in the lower mantle stay for a longer time period and

wander around with the ambient mantle flow. The pond of plume material underneath 660 km phase boundary is probably too thin to be resolved by traditional seismic tomography, but its effect on the topography of 660 km phase boundary may be resolvable with modern imaging technology (e.g., *Cao et al.,* 2011). The size of the plume conduit is several hundred kilometers, but the size of the stagnant plume head may be on the order of several thousand kilometers.

In our latest seismic imaging study of the transition zone underneath the Hawaii hotspot (see **Chapter III** of the thesis) we found a 800-2000 km wide hot anomaly in the 660 km discontinuity to the west of Hawaii. This is much larger than the diameter of plume conduits estimated from geodynamical modeling studies. Previous seismic studies of the global topographies of 410 and 660 km discontinuities show that global anti-correlation of 410 and 660 km discontinuities, as expected from the opposite Clapeyron slopes, is not evident (*Gu et al., 1998; Gu and Dziewonski, 2002; Shearer, 1993*). Our geodynamical modeling of plumes suggests that because of ponding of hot materials below the 660 km phase boundary the lateral scale of the uplift in 660 km discontinuity is much larger than that of the depression in 410 km discontinuity. Besides the difference in the lateral scale of the topography, the shifting of the secondary plume position with respect to the primary plume also implies that, the geographic locations with the maximum depression of the 410 km discontinuity may not necessarily be the locations with the maximum elevation of 660 km discontinuity.

4.6 Conclusions and future work

This paper tries to answer the question: "What should a plume look like in the real Earth?" Our geodynamical modeling with realistic estimates of the Earth's parameters suggest that upwellings may be quite different from the canonical mushroom type plume. This has significant implications for the topographies of the phase boundary and the estimation of mass and heat transport across the phase boundary. Based on the mushroom type plume model, scientists predicted that the scale of the 410 and

660 km discontinuities topography should be comparable and that there should be some degree of anti-correlation of the topographies in a plume. However, this picture no longer exists in some of our modeling results. In the upper mantle we also observed secondary plumes triggered by a primary (lower mantle) plume. Whether such a secondary plume is triggered by the heating of the primary plume (without substantial mass transport across the discontinuity) or is formed by material transport through the phase boundaries has significant implication for resolving the mystery in the interpretation of isotopical signatures of hotspot lavas.

For this study, we include the effects of only two phase transitions (olivine to wadsleyite transition and ringwoodite to perovskite and ferropericlase (magnesiowüstite) transition (also referred to as the post-spinel transition)). There are other phase transitions that may occur in depth range of the transition zone, for instance, wadsleyite to ringwoodite at ~520 km depth and post-garnet at ~700 km depth. Investigating the influence of such additional phase transitions on mantle flow across the transition zone is a target of future research. In particular, post-garnet transitions that may occur near the same depth as the post-spinel transition – as demonstrated experimentally (*Weidner and Wang, 1998; Hirose, 2002; Nishiyama and Yagi, 2003*) and for which seismological evidence has begun to appear (e.g., *Duess et al., 2006; Cao et al., 2011*) – probably have a positive Clapeyron slope (*Akaogi and Ito, 1999*), which suggests that they could facilitate material exchanges and to some extent prevent the ponding of plume materials underneath the transition zone. Their net dynamical effect depends, however, on the density contrasts of the various phase transitions involved, which are not yet well known.

References Cited

Albers, M., U. R. Christensen, 1996. The excess temperature of plumes rising from the core mantle boundary. *Geophys. Res. Lett.*, 23, 3567–70.

Allegre, C. J., and D. L. Turcotte, 1985. Geodynamic mixing in the mesosphere boundary layer and the origin of oceanic islands. *Geophys. Res. Lett.*, 12, 207-210.

Akaogi, M. and E. Ito, 1999. Calorimetric study on majorite–perovskite transition in the system $Mg_4Si_4O_{12}$–$Mg_3Al_2Si_3O_{12}$: Transition boundaries with positive pressure–temperature slopes. *Phys. Earth Planet. Inter.*, 114, 129.

An, Y., Y. J. Gu, and M. D. Sacchi, 2007. Imaging mantle discontinuities using least squares Radon transform. *J. Geophys. Res.*, 112, B10303, doi:10.1029/2007JB005009.

Anderson, D. L., 2000. Thermal state of the upper mantle: no role for mantle plumes. *Geophysical Research Letters*, 27, 22, 3623-3626.

Antretter, M., B. Steinberger, F. Heider, and H. Soffel, 2002. Paleolatitudes of the Kerguelen hotspot: New paleomagnetic results and dynamic modeling. *Earth Planet. Sci. Lett.*, 203, 635–650.

Antretter, M., P. Riisager, S. Hall, X. Zhao, and B. Steinberger, 2004. Modeled paleolatitudes for the Louisville hotspot and the Ontong Java Plateau. in *Origin and Evolution of the Ontong Java Plateau, edited by G. Fitton et al., Geol. Soc. Spec. Publ.*, 229, 21–30.

Bina, C. R. and G. Helffrich, 1994. Phase transition Clapeyron slopes and transition zone seismic discontinuity topography. *J. Geophys. Res.*, 99(B8), 15,853–15,860.

Blichert-Toft, J., D. Weis, C. Maerschalk, A. Agranier, F. Albarède, 2003. Hawaiian hot spot dynamics as inferred from the Hf and Pb isotope evolution of Mauna Kea volcano. *Geochem. Geophys. Geosyst.*, 4, No.5.

Cao, Q., P. Wang, R. D. Van der Hilst, M. V. De Hoop, and S.-H. Shim, 2010. High-resolution

imaging of upper mantle discontinuities with a generalized Radon Transform of SS precursors. *Physics of Earth and Planetary Interiors*, 180, 80-91.

Cao, Q., P. Wang, R. D. Van der Hilst, M. V. De Hoop, and S.-H. Shim, 2011. Seismic imaging of transition zone discontinuities suggests hot mantle west of Hawaii. *Science*, 332, 1068-1071.

Chambers, K., J. H. Woodhouse, and A. Deuss, 2005a. Reflectivity of the 410-km discontinuity from *PP* and *SS* precursors. *J. Geophys. Res.*, 110(B02301), doi:10.1029/2004JB003345.

Chambers, K., J. H. Woodhouse, and A. Deuss, 2005b. Topography of the 410-km discontinuity from *PP* and *SS* precursors. *Earth Planet. Sci. Lett.* ,235, 610–622.

Christensen, U. R., and D. A. Yuen, 1985. Layered convection induced by phase transition. *J. Geophys. Res.*, 90, 10291-10300.

Christensen, U., 1995. Effects of Phase Transitions on Mantle Convection. *Annual Review Of Earth And Planetary Science*, 23, 65-88.

Christensen, U. R. and D. A. Yuen, 1984. The interaction of a subducting lithospheric slab with a chemical or phase boundary. *J. Geophys. Res.*, 89. 4389-4402.

Clouard, V. and A. Bonneville, 2001. How many Pacific hotspots are fed by deep-mantle plumes?, *Geology*, 21, 695-698.

Courtillot, V., A. Davaille, J. Besse, J. Stock, 2003. Three distinct types of hot spots into the Earth's mantle. *Earth Planet. Sci. Lett.*, 205, 295.

Cserepes, L. and D. A. Yuen, 2000. On the possibility of a second kind of mantle plume. *Earth Planet. Sci. Lett.*, 183, 61–71.

Davies, G. F., 1995. Penetration of plates and plumes through the mantle transition zone. *Earth Planet Sci. Lett.*, 133, 507–516.

Deuss, A., S. A. T. Redfern, K. Chambers, and J. H. Woodhouse, 2006. The nature of the 660-kilometer discontinuity in Earth's mantle from global seismic observations of *PP* precursors. *Science*, 311, 198–201.

Deuss, A., 2007. Seismic observations of transition zone discontinuities beneath hotspot locations. Special Papers of the Geological Society of America, 430, *Plates, plumes and Planetary Processes edited by Foulger, G. R. and D. M. Jurdy*, 121-136.

Farnetani C., 1997. Excess temperature of mantle plumes: the role of chemical stratification across D''. *Geophys. Res. Lett.*, 24, 1583–86.

Farnetani, C. and A. W. Hofmann, 2009. Dynamics and internal structure of a lower mantle plume conduit. *Earth and Planetary Science Letters*, 282, 314-322.

Flanagan, M. P., and P. M. Shearer, 1998. Global mapping of topography on transition zone velocity discontinuities by stacking *SS* precursors. *J. Geophys. Res.*,103, 2673– 2692.

Flanagan, M. P., and P. M. Shearer, 1999. A map of topography on the 410-km discontinuity from *PP* precursors. *Geophys. Res. Lett.*, 26, 549-552.

Fukao, Y., M. Obayashi, H. Inoue, M. Nenbai, 1992. Subducting slabs stagnant in the mantle transition zone. *J. Geophys. Res.*, 97, 4809-4822.

Gossler, J., and R. Kind, 1996. Seismic evidence for very deep roots of continents. *Earth Planet. Sci. Lett.*, 138, 1– 13.

Griffiths, R. E., I. H. Campbell, 1990. Stirring and structure in mantle starting plumes. *Earth Planet. Sci. Lett.*, 99,66–78.

Gu, Y., A. M. Dziewonski, and C. B. Agee, 1998. Global de-correlation of the topography of transition zone discontinuities. *Earth Planet. Sci. Lett.*, 157, 57–67.

Gu, Y. J. and A. M. Dziewonski, 2002. Global variability of transition zone thickness. *J. Geophys. Res.*

107(B7), doi:10.1029/2001JB000489.

Hirose, K., 2002. Phase transitions in pyrolitic mantle around 670-km depth: Implications for upwelling of plumes from the lower mantle. *J. Geophys. Res.*, 107, (B4), 2078.

Honda, S., D. A. Yuen, S. Balachandar, D. M. Reuteler, 1993. Three-dimensional instabilities of mantle convection with multiple phase transitions. *Science*, 259, 1308-1311.

Ito, E., and E. Takahashi, 1989. Postspinel transformations in the system Mg_2SiO_4–Fe_2SiO_4 and some geophysical implications. *J. Geophys. Res.*, 94(B8), 10,637–10,646.

Lebedev, S., S. Chevrot, and R. D. van der Hilst, 2002. Seismic evidence for olivine phase change at the 410- and 660-kilometer discontinuities. *Science*, 296, 1300–1302.

Lebedev, S., S. Chevrot, and R. D. Van der Hilst, 2003. Correlation between the shear-speed structure and thickness of the mantle transition zone. *Phys. Earth Planet. Int.*, 136, 25–40.

Leng, W., and S. J. Zhong, 2006. Viscous heating, adiabatic heating and energetic consistency in compressible mantle convection. *Geophys. J. Int.*, 173, 693-702.

Machetel, P., and P. Weber, 1991. Intermittent layered convection in a model mantle with an endothermic phase change at 670 km. *Nature*, 350, 55-57.

McKenzie, D.P., and R. K. O'Nions, 1983. Mantle reservoirs and oceanic island basalts, *Nature*, 301. 229-231.

McNutt, M.K., 1998. Superswells. *Rev. Geophys.*, 36. 211-244.

Morgan, W.J., 1972. Deep mantle convection plumes and plate motion. *Am. Assoc. Petrol. Geol. Bull.*, 56, 203-213.

Moresi, L., and M. Gurnis, 1996. Constraints on the lateral strength of slabs from three-dimensional dynamic flow models. *Earth Planet. Sci. Lett.*, 138, 15–28.

Nakakuki, T., H. Sato, H. Fujimoto, 1994. Interaction of the upwelling plume with the phase and chemical boundary at the 670 km discontinuity: effect of temperature-dependent viscosity. *Earth Planet Sci. Lett.*, 121, 369–384.

Nataf, H.-C., 2000. Seismic Imaging of Mantle Plumes. *Annual Review of Earth and Planetary, Science*, 28, 391-417.

Nishiyama, N., and T. Yagi, 2003. Phase relation and mineral chemistry in pyrolite to 2200°C under the lower mantle pressures and implications for dynamics of mantle plumes. *J. Geophys. Res.*, 108, 2255.

Olson, P., H. A. Singer, 1985. Creeping plumes. *J. Fluid Mech.*,158, 511–31.

O'Neill, C., D. Müller, and B. Steinberger, 2003. Geodynamic implications of moving Indian Ocean hotspots. *Earth Planet. Sci. Lett.*, 215, 151–168, doi:10.1016/S0012-821X (03)00368-6.

O'Neill, C., D. Müller, and B. Steinberger, 2005. On the uncertainties in hot spot reconstructions and the significance of moving hot spot reference frames. *Geochem. Geophys. Geosyst.*, 6, Q04003, doi:10.1029/2004GC000784.

Rost, S. and C. Thomas, 2009. Improving seismic resolution through array processing techniques. *Surveys in Geophysics*, 30, Issue 4-5, 271-299.

Samuel, H. and C. G. Farnetani, 2003. Thermochemical convection and helium concentrations in mantle plumes. *Earth Planet. Sci. Lett.,* 207, 39-56.

Schmerr, N., and E. Garnero, 2006. Investigation of upper mantle discontinuity structure beneath the central Pacific using *SS* precursors. *J. Geophys. Res.*, 111, B08305, doi:10.1029/2005JB004197.

Schubert, G., C. Anderson, P. Goldman, 1995. Mantle plume interaction with an endothermic phase change. *Geophys. Res. Lett.*, 100, 8245–8256.

Shearer, P. M., and G. Masters, 1992. Global mapping of topography on the 660-km discontinuity.

Nature, 355, 791– 796.

Shearer, P. M., 1993. Global mapping of upper mantle reflectors from long-period *SS* precursors. *Geophys. J. Int.*,115, 878–904.

Sleep, N. H., 1990. Hotspots and mantle plumes: some phenomenology. *J. Geophys. Res.*, 95, 6715-6736.

Solheim, L. P., and W. R. Peltier, 1994. Avalanche effects in phase transition modulated thermal convection: a model of Earth's mantle. *J. Geophys. Res.*, 99. 6997-7018.

Steinbach V. C., and D. A. Yuen, 1997. Dynamical effects of a temperature- and pressure-dependent lower-mantle rheology on the interaction of upwellings with the transition zone. *Phys. Earth Planet. Sci.*, 103, 85–100.

Steinberger, B., 2000. Plumes in a convecting mantle: Models and observations for individual hotspots. *J. Geophys. Res.*, 105, 11,127–11,152.

Steinberger, B., and R. J. O'Connell, 1998. Advection of plumes in mantle flow: Implications for hotspot motion, mantle viscosity and plume distribution. *Geophys. J. Int.*, 132, 412–434.

Steinberger, B., and R. J. O'Connell, 2000. Effects of mantle flow on hotspot motion, in *The History and Dynamics of Global Plate Motions, Geophys. Monogr. Ser., vol. 121, edited by M. A. Richards, R. G. Gordon, and R. D. van der Hilst*, 377–398, AGU, Washington, D. C.

Steinberger, B., R. Sutherland, and R. J. O'Connell, 2004. Prediction of Emperor-Hawaii seamount locations from a revised model of plate motion and mantle flow. *Nature*, 430, 167-173.

Steinberger, B., and M. Antretter, 2006. Conduit diameter and buoyant rising speed of mantle plumes: Implications for the motion of hot spots and shape of plume conduits. *Geochem. Geophys. Geosyst.*, 7, Q11018, doi:10.1029/2006GC001409.

Tackley, P. J., D. J. Stevenson, G. A. Glatzmaier, G. Schubert, 1993. Effects of an endothermic phase

transition at 670 km depth in a spherical model of convection in the Earth's mantle. *Nature*, 361, 699-704.

Tackley, P. J., D. J. Stevenson, G. A. Glatzmaier, G. Schubert, 1994. Effects of a multiple phase transitions in a 3D spherical model of convection in the Earth's mantle. *J. Geophys. Res.*, 99, 15877-15901.

Tackley, P. J., 1995. On the penetration of an endothermic phase transition by upwellings and downwellings. *Journal* of *Geophysical Research, 100*, 15477-15488.

Tackley, P. J., 2008. Layer cake or plume pudding? *Nature Geoscience*, Vol 1 No 3, 157-158.

Tarduno, J. A., R. A. Duncan, D. W. Scholl, R. D. Cottrell, B. Steinberger, T. Thordarson, B. C. Kerr, C. R. Neal, F. A. Frey, M. Torii and C. Carvallo, 2003. The Emperor Seamounts: Southward motion of the Hawaiian hotspot plume in Earth's mantle. *Science*, 301, 1064–1069.

Tarduno, J., H-P. Bunge, N. Sleep, U. Hansen, 2009. The Bent Hawaiian-Emperor Hotspot Track: Inheriting the Mantle Wind. *Science*, 324. no. 5923, 50 – 53.

Van der Hilst, R., R. Engdahl, W. Spakman, G. Nolet, 1991. Tomographic imaging of subducted lithosphere below northwest Pacific island arcs. *Nature*, 353, 37-43.

Weinstein, S. A., 1993. Catastrophic overturn of the Earth's mantle driven by phase changes and internal heat generation. *Geophys. Res. Lett.*, 20, 101-104.

Weidner, D. J. and Y. Wang, 1998. Chemical- and Clapeyron-induced buoyancy at the 660 km discontinuity. *J. Geophys. Res.*, 103, (B4), 7431.

Whitehead J. A., D. S. Luther, 1975. Dynamics of laboratory diapir and plume models. *J. Geophys. Res.*,80,705–17.

Zhao, W., D. A. Yuen, S. Honda, 1992. Multiple phase transitions and the style of mantle convection. *Phys. Earth Planet. Inter.*, 72, 185-210.

Zhong, S. and M. Gurnis, 1995. Mantle convection with plates and mobile faulted plate margin. *Science*, 267, 838- 843.

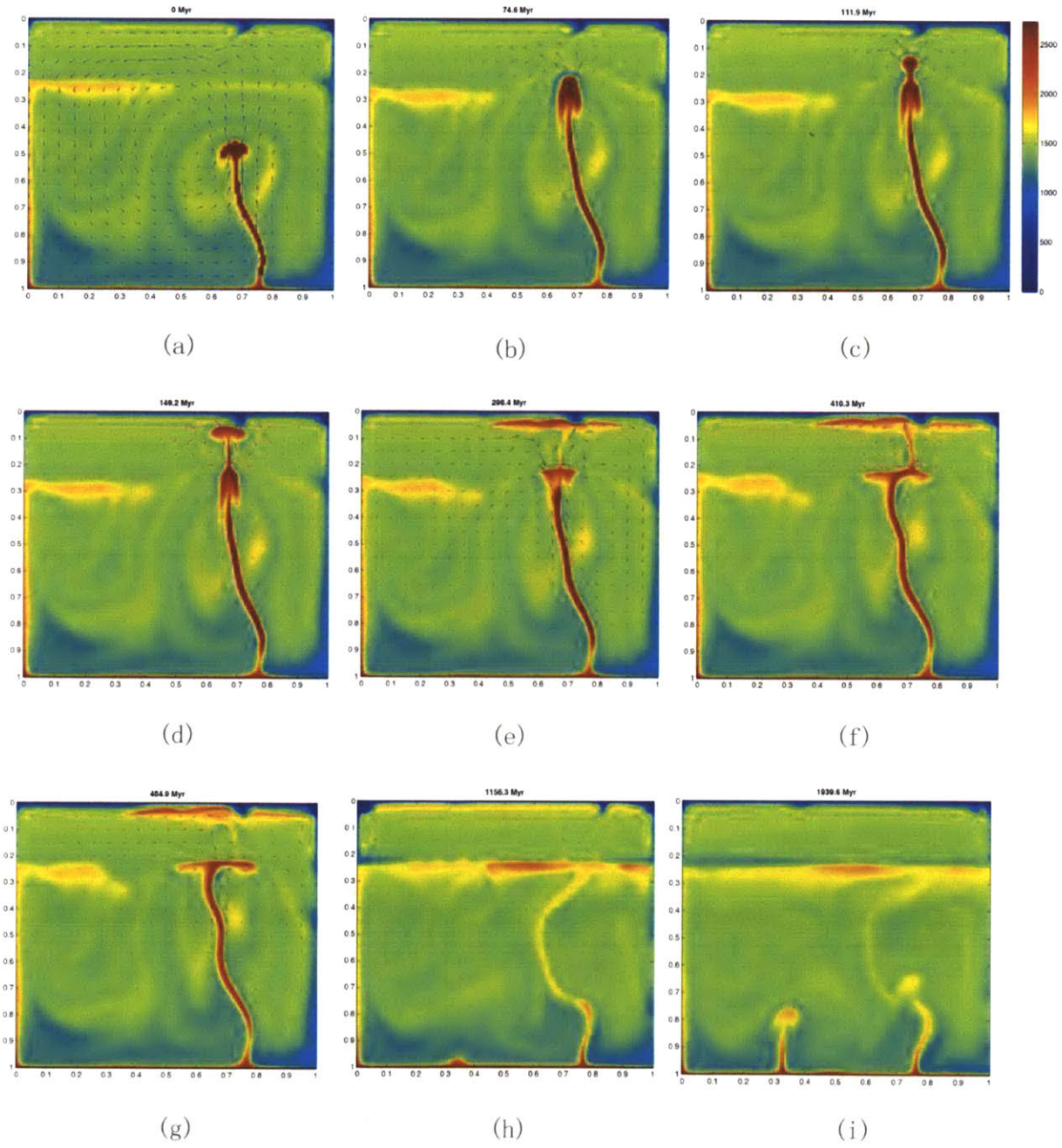

Figure 4-1. Snapshots for the plume evolution process after amplifying the temperature in a start plume by a factor of 2.0 (P = 2.0). The temperature field is shown by colors. Arrows show the velocity field. The time is shown in the title. The initial time starting the plume is set to be 0 and relative time with respect to the initial time is used. A detailed description can be found in section 4.4.1.

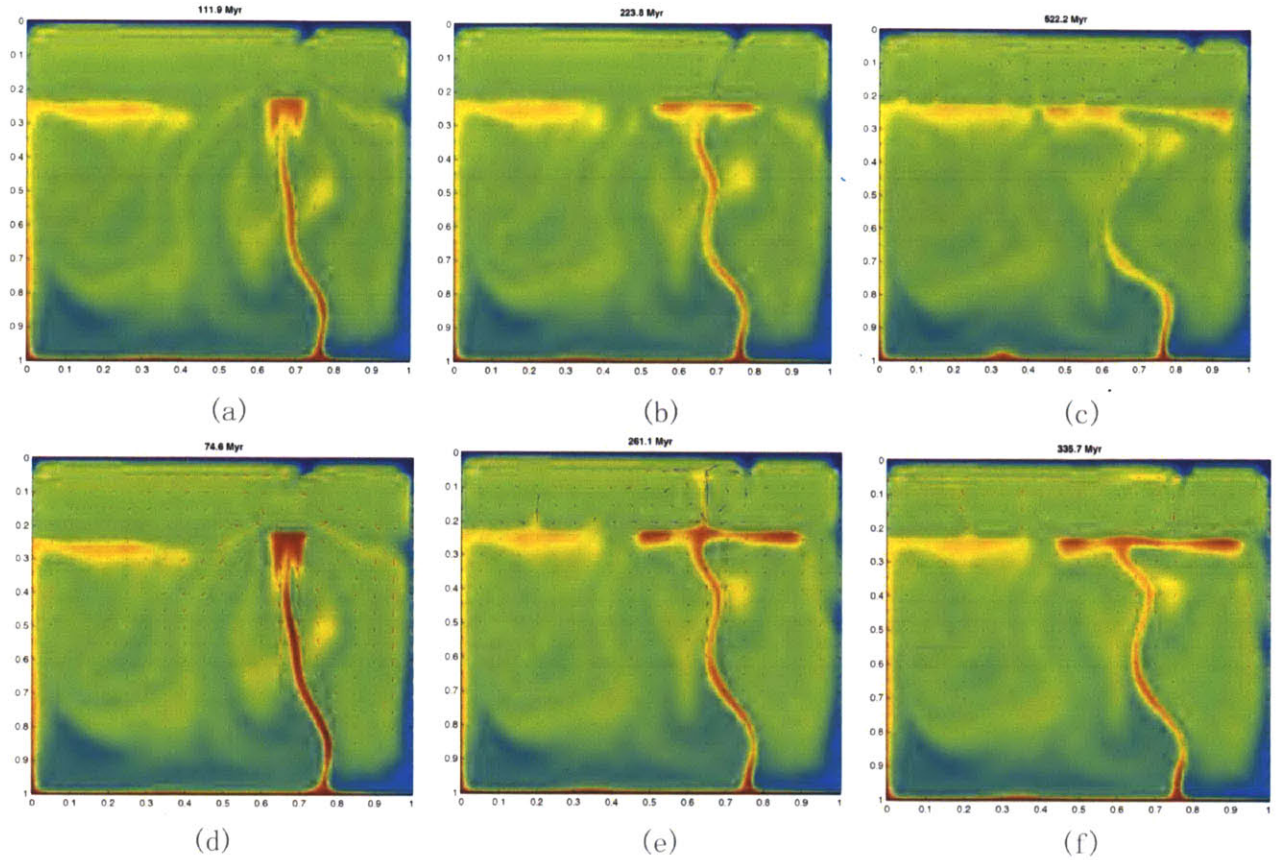

Figure 4-2. The snapshots for the evolution of plumes with different strengths (amplification factors) from Figure 4-1- Upper row: Three snapshots for P = 1.2; lower row: three snapshots for P = 1.5. Descriptions can be found in section 4.4.2.

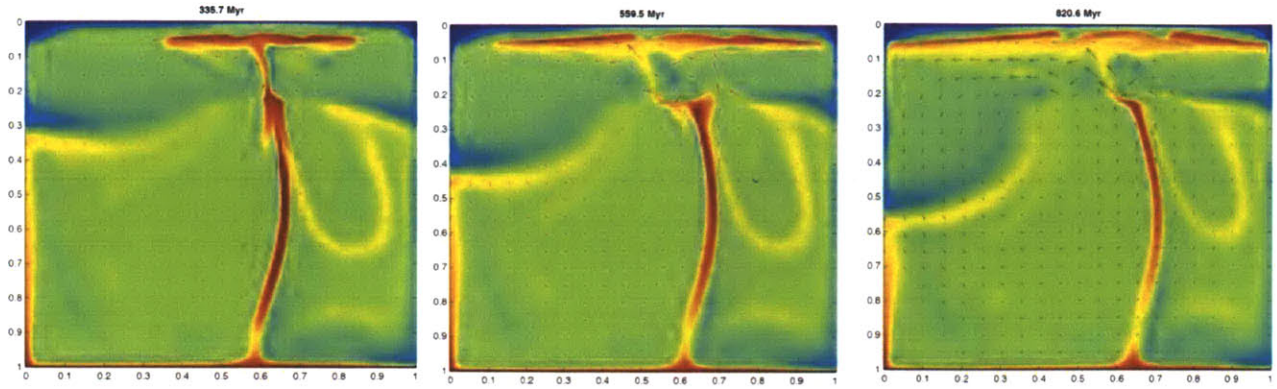

(a) (b) (c)

Figure 4-3. The evolution process for a plume starting in a mantle temperature profile with larger upper/lower mantle temperature contrast. The plume is started in quasi-steady state. There are pilings of cold slabs above the transition zone, which lower the average temperature of the upper mantle. The amplifying factor P is taken to be 2.0.

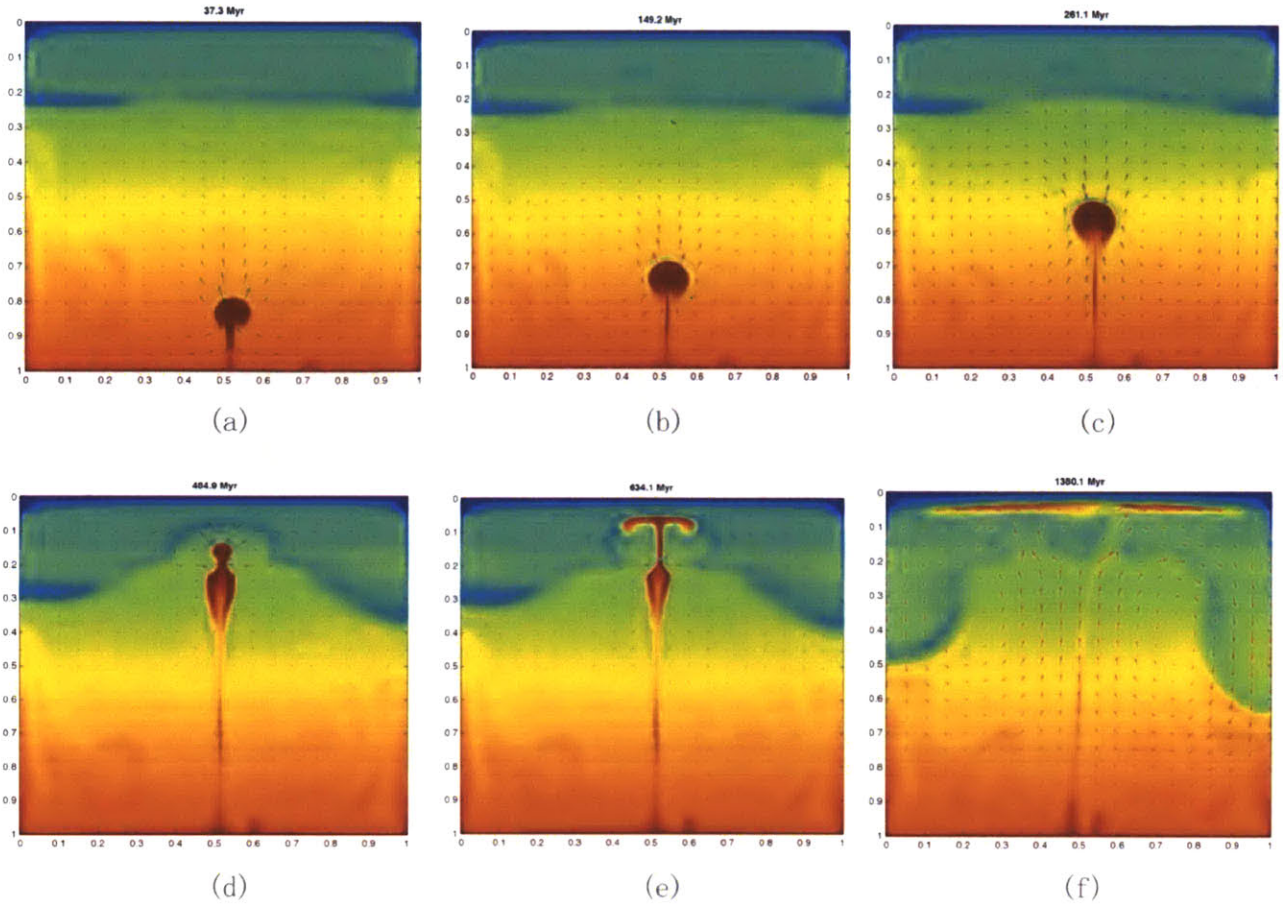

Figure 4-4. Plume evolution process when adiabatic cooling effect is taken into account. The dissipation number is set to be 0.5, while all the other parameters are kept the same. A quasi-steady state is reached before we amply the temperature of start plume by a factor of P = 2.0.

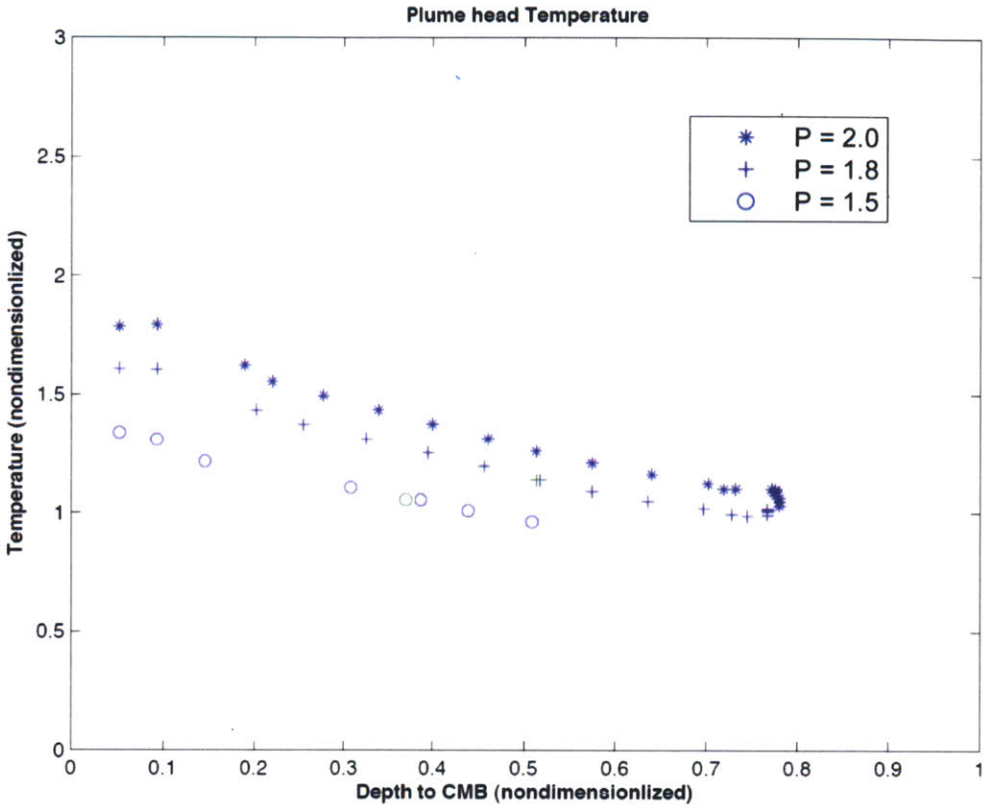

Figure 4-5. The maximum plume head temperature (vertical axis) as the plume head ascended from the core-mantle boundary (CMB). Horizontal axis is the distance of plume head from the CMB. We only recorded the temperature until the plume head reached 660 km depth (660 km is around 0.8 after non-dimensionalization with mantle thickness). Three types of data are for three different starting temperatures (i.e. different amplifying factors for the start plume) P=1.5, 1.8, 2.0.

Chapter 5

Preliminary seismic images of the upper mantle transition zone beneath northwest Pacific subduction systems

Abstract

Subduction zones are key components of Earth's dynamic system. Taking advantage of the rapidly increasing global seismic networks, we apply the generalized Radon transform to study the transition zone discontinuities in the Kuril subduction zone. Our imaging results show that, the 660' topography deepens in the slab that is penetrating directly into the lower mantle according to tomography images. In the region with a stagnant slab on top of the lower mantle, we found broadening of 660' at both edges of the slab. No corresponding uplift of 410' is found at the slab location indicated by tomography results. However, a shallow 410' is found at the continental side of the subduction zone. We also updated the image profiles in **Chapter II** and **Chapter III** using the recently increased dataset. The similarity between the new and old image profiles demonstrates the robustness of our imaging algorithm.

5.1 Introduction

Cold downwellings in the form of subducting lithospheric slabs and hot upwellings in the form of hot mantle plumes may be the two complementary components of mantle convection. Subduction zones represent perhaps the most tectonically complicated regions on the Earth, and although the morphologies of subducting slabs have been relatively well characterized by seismic tomography (e.g. see a recent review by *Fukao et al., 2001*), many questions remain unanswered about the mineralogy,

water content, and dynamic process of subduction zones (*Bercovici and Karato, 2003; Hacker et al., 2003a, b; Richard et al., 2006*).

In **Chapter III** of this thesis we used the generalized Radon transform to study the transition zone structures beneath the Hawaii hotspot, which reveals a more complicated thermal and dynamical picture of the Earth than previously thought. In this chapter we apply the same technique to study the transition zone discontinuities underneath the subduction zone system. These discontinuities, believed to be caused by pressure-induced mineral phase transitions, occur at different depths when the temperature or chemical composition changes across geographic regions. Therefore, by detecting, measuring the topography of, and characterizing the properties of these discontinuities seismically, important information can be inferred about the mineralogical and geodynamical state of subduction zones.

The Kuril subduction zone in the northwest Pacific, formed by the subduction of the Pacific lithosphere beneath the Sea of Okhotsk (~ 8.2 cm/year, according to *Demets, 1992*), has been the subject of many seismological studies (e.g., *Jordan, 1977, Van der Hilst et al., 1991; Fukao et al., 1992; Van der Hilst and Seno, 1993; Fukao et al., 2001; Miller et al., 2004; Li et al., 2006*). The style of seismicity and subduction process varies along the trench. To the north, the slab sinks steeply and seems to penetrate into the lower mantle. Southward, the dip angle of subduction gradually decreases and parts of the slabs appear stagnant on top of the 660 km discontinuity. There are also global studies of the transition zone discontinuities using common midpoint stacking (CMP stacking) of *SS* and *SS* precursors waveforms covering this area (see section 2.1). Most studies find a consistent thickened transition zone in the subduction zones of the Pacific ring, where the thickness can vary by up to 10 km (*Flanagan and Shearer, 1998; Gu et al., 2003; Houser et al., 2008; Lawrence and Shearer, 2008; Deuss, 2009*). However, due to the inherent averaging of the topographies of discontinuities when applying CMP over geographic caps as large as 20° in diameter (this value varies among studies), the resolution

of the results in these studies is on the scale of several thousand kilometers. Small scale transition zone structures related to the subducting slabs may be overlooked.

Because of the rapid growth of global seismic networks and the availability of large numbers of broadband seismograms, the sampling of *SS* bounce points near the subducting slabs in the northwest Pacific has been greatly improved in recent years (Figure 5-1). This development may enable high-resolution studies of mantle transition zone discontinuities using the GRT method in this area. While our main imaging focus is the Kuril subduction zone, we reconstruct the image profiles shown in **Chapter II** and **Chapter III** by including the latest global seismic waveform dataset (up to June 2011).

5.2 Data selection and processing

We retrieve all the broad-band global seismic network waveform data with midpoints falling in the North hemisphere (and recorded between January 1990 and June 2011) from the Data Management Center (DMC) of the Incorporated Research Institutions for Seismology (IRIS). To balance the trade-off between the number of the data that can be utilized for GRT to suppress the noise and the quality of the dataset, we use a slightly looser data selection criterion compared to our previous two studies (*Cao et. al. 2010*, *Cao et al. 2011*). We select records from events with body-wave magnitudes greater than 5.0. Only events with focal depths less than 100 km are used to minimize the effects of depth phases. For records with epicentral distances from 90° to 170°, we extract time windows containing *SS* proper and precursors due to scattering in the transition zone. The seismic records are band-pass filtered with a 4-pole Butterworth filter with corner periods at 20 s and 50 s. We use hypocenter parameters from the EHB catalog (*Engdahl et al., 1998*) to correct for event parameters in the seismograms. The polarity of each trace is checked to ensure that the *SS* phase has positive polarity and reversed if necessary. Then we deconvolve the instrument response, rotate the data to radial and

transverse direction. The traces are Hilbert transformed and normalized with respect to the *SS* pulse, which is picked automatically from the time window around the *SS* theoretical traveltime. We align each seismogram with respect to the *SS* theoretical traveltime, so the timeline in the seismogram reflects only the travel time differences between *SS* proper and other arrivals.

After these preprocessing procedures, the waveforms are subjected to a signal-to-noise (SNR) selection criterion (with SNR defined as the ratio of peak amplitude of SS proper signal to the maximum amplitude of the whole window containing *SS* proper and precursors, 40s before $S_{200}S$ and 40s after *SS*). Seismic traces with signal-to-noise ratios smaller than 1/4 are discarded. For the reasons explained in *Cao et al.* (2010), for a given image point, we restrict the dataset that enters into the computation of images to records associated with rays with a specular reflection within a certain distance (here 10°) of the image point. A cosine weighting function is applied to the traces with distances from 5° to 10° to damp possible influences of interfering phases in the time window. We also make travel time corrections using the 3D tomography model developed by *Grand (2002)*.

5.3 Preliminary imaging results across the Kuril subduction zone

We have computed the 3D GRT images of the transition zone structures beneath the entire North hemisphere, including both continents and oceans, from over ~1,600,000 traces of seismograms recorded at global seismic networks. Here, we first show two great-circle sections across the Kuril subduction zone; their locations are depicted in Figures 5-1 and 5-2 as dashed lines. These two sections are in the well-sampled areas of *SS* bounce points (Figure 5-1a,b). The data coverage is especially good in the middle region of the two lines, where the lines cross the subduction system. Figure 5-2 shows the seismicity events between January 1990 and June 2011 in the entire area. At the Kuril trench, there is a clear order in the distribution of earthquakes according to the focal depth: deeper earthquakes tend

to appear to the west of shallower earthquakes, as expected from westward subduction. We also observe that, in the northern part of the Kuril subduction zone, deep seismicity (>300 km) occurs further into the interior of the Eurasian plate. Tomographically inferred wavespeed variations (MITP08, as shown in the background of Figures 5-3 and 5-4) show that the subducting slab penetrates the transition zone and sinks directly into the lower mantle in the northern part, while in the southern part the slab appears stagnant in the transition zone.

Figure 5-3 shows the GRT images for the blue section in Figure 5-2. In total, 63 radial reflectivity profiles are juxtaposed to form a 2D west-east seismic section from (60°N, 110°E) to (42°N, 172°E). The great circle distances between neighboring profiles are the same in Figures 5-3 and 5-4. Large-amplitude, laterally continuous 410' and 660' signals show up along the entire 2D section, near depths of 410 km and 660 km (red dashed lines in Figure 5-2), respectively. Weaker signals appear near a depth of 520 km. The 520' signals are simple and laterally continuous from 135°E to 172°E, while to the west of 135°, the signals begin to split. The topographies of 410' and 660' can be seen more clearly in the right panel, which enlarges the depth range from 350 to 750 km. The 660' topography is close to 660 km in most of the section (±2 km), while between 150°E and 165° there is a deepening of 660' to ~668 km depth. The location of the deepened 660' is in accordance with the tomography wavespeed model in background (MITP08, by *Li et al., 2008*). It is worth pointing out that the wavespeed variations that we plotted in the background are for a P-wavespeed model, i.e., not the S-wavespeed model (*Grand, 2002*) that we used for traveltime correction. This independence implies that the deepening of 660' here is not an artifact from traveltime correction. In a normal-to-cold mantle, the 660 km discontinuity is often attributed to the post-spinel transition. This phase transition has a negative Clapeyron slope (*Ringwood, 1975; Ita and Stixrude, 1992; Weidner and Wang, 2000; Li and Liebermann, 2007*), and hence occurs at a greater depth if there is a cold thermal anomaly. Therefore, our observation is consistent with the existence of a cold slab at this depth of the transition zone.

However, the lateral extent of the topography deepening is larger than that of the high speed anomaly in the background tomographic wavespeed model. The 410' topography is enigmatic. There is an uplift of the topography at around 150°E, to ~410 km, and to the east, the topography seems almost flat (at~ 415 km) with a slight increase since 165°E (to 417 km). From 110°E to 150°E, the topography is mostly shallower (~422 km) than average, while there is an uplift at around 137°E. If only temperature is taken into account, this shallowing of 410 km discontinuity suggests that the temperature at 410 km is colder at the eastern part of the section compared to the western part, because of the positive Clapeyron slope of the 410' (*Katsura et al., 2004*). There are also laterally continuous signals appearing at depths of around 350 and 850 km, although the amplitude of these signals varies along the section.

Figure 5-4 shows another 2D west-east section across the southern part of the subduction zone from (53°N, 110°E) to (33°N, 172°E), as shown by the black line in Figure 5-2. Tomography images in the background suggest a stagnant slab (blue part in the background) in the transition zone of this area. Similar to Figure 5-3, we observed strong laterally continuous 410' and 660' signals along the entire 2D section. The 520' signals are more laterally continuous compared to those in Figure 5-3. No splitting of 520' is observed, while there is a broadening of the 520' signals at around 132°E and 150°E. We did not pick the topography of 660' in this section, due to a sudden change in the width of the 660' signals at the edge of the cold region indicated by the tomography results. The width of the 660' from 128°E to 135°E and from 146°E to 158°E is almost twice the width of the 660' signal inside the cold region, which makes it difficult to compare topographies. Again, the tomography results shown in the background differ from the tomography model we used to make the 3D traveltime correction, so the change in the 660' signals is not an artifact from traveltime correction using tomography model. The width of 660' signals decreases west of 120°E and east of 160°E. The 410' has a V-shape topography, with the deepest locations at around 138°E (to ~424 km). The topography gradually increases to ~410 km to the east and to ~414 km to the west. If we interpret the 410' topography in terms of temperature

change in the section, then the hottest region in this section is between 130°E and 144°E. Finally, compared to Figure 5-3, the signal near 850 km depth splits at more locations.

5.4 Imaging results compared with Chapter II and Chapter III

To ensure compatibility with our previous results, we repeated the computation of the image profiles shown in Figure 2-10a and Figure 3-2, using the most recently updated dataset including the latest seismic events up to June 2011. The comparison between old and new images is shown in Figure 5-5. There are some second order feature changes: e.g., an increase in the amplitude of 520' in Figure 5-2b compared to Figure 5-2a, clearer splitting of 520' in Figure 5-5d compared to Figure 5-5c, and more laterally continuous signals at around 300 km in Figure 5-5d compared to Figure 5-5c. However, most of the first order observations stay unchanged (e.g. 410' and 660' topography, 520' splitting). In the latest study, we use looser data selection rules (see section 5.2), so the number of data entering into each image point has been increased considerably. This test shows that, in the areas with sufficient data coverage, our GRT imaging method is robust.

5.5 Discussions and conclusions

In this chapter, we present preliminary results of GRT imaging in the Kuril subduction zone. The images we obtained are promising, although some features are difficult to interpret at present. In the northern part of the subduction zone, where the slab penetrates directly into the lower mantle, according to tomography inversion results, we observed a deepening of 660' in and near the slab. In the southern part of the Kuril subduction zone, we observed a broadening of the 660' signals at both edges of the subducting slabs compared to the 660' signals inside and far away from the slab. The 410' topography in both sections is unexpected. No corresponding uplift of 410' signals is observed inside

the slab inferred from tomography. However, underneath the continental side of the subduction zone, deepening of 410' is observed in both sections, indicating a hotter anomaly at 410 km depth compared to the other part of the subduction zone if only thermal effect plays a role.

References Cited

Bercovici, D. and S. Karato, 2003. Whole mantle convection and the transition-zone water filter. *Nature*, 425, 39-44.

Cao, Q., P. Wang, R. D. van der Hilst, M. de Hoop, and S.-H. Shim, 2010. Imaging the upper mantle transition zone with a generalized Radon transform of SS precursors. *Physics of Earth and Planetary Interiors*, 180, 80-91.

DeMets, C., 1992. Oblique convergence and deformation along the Kuril and Japan trenches. *J. Geophys. Res.-Solid Earth*, 97, 17615-17625.

Deuss, A., 2009. Global Observations of Mantle Discontinuities Using *SS* and *PP* Precursors. *Surveys in Geophysics*, 30 (4). 301-326.

Engdahl, E. R., R. D. Van der Hilst, and R. P. Buland, 1998. Global teleseismic Earthquake relocation from improved travel times and procedures for depth determination. *Bull. Seis. Soc. Am*, 88 (3), 722-743.

Flanagan, M. P., and P. M. Shearer, 1998. Global mapping of topography on transition zone velocity discontinuities by stacking of SS precursors. *J. Geophys. Res.*, 103(B2), 2673–2692

Fukao, Y., M. Obayashi, H. Inoue, and M. Nenbai, 1992. Subducting slabs stagnant in the mantle transition zone. *J. Geophys. Res.*, 97, 4809-4822.

Fukao, Y., S. Widiyantoro, and M. Obayashi, 2001. Stagnant slabs in the upper and lower mantle transition region. *Rev. Geophys.*, 39, 291–323.

Gu, Y., A. M. Dziewonski, and G. Ekström, 2003. Simultaneous inversion for mantle shear wave velocity and topography of transition zone discontinuities. *Geophys. J. Int.*, 154:559–583.

Hacker, B. R., G. A. Abers, and S. M. Peacock, 2003. Subduction Factory 1. Theoretical mineralogy, density, seismic wave speeds, and H_2O content. *J. Geophys. Res., 108* (B1), 2029, doi:10.1029/2001JB001127.

Hacker, B. R., S. M. Peacock, G. A. Abers, and S. D. Holloway, 2003. Subduction Factory 2. Intermediate-depth earthquakes in subducting slabs are linked to metamorphic dehydration reactions. *J. Geophys. Res., 108* (B1), 2030, doi:10.1029/2001JB001129.

Houser, C., G. Masters, M. Flanagan, P. Shearer, 2008. Determination and analysis of long-wavelength transition zone structure using *SS* precursors. *Geophys. J. Int.*, 174:178–194.

Jordan, T. H., 1976. Lithospheric slab penetration into lower mantle. *Transactions American Geophysical Union*, 57, 962-962.

Jordan, T. H., 1977. Lithospheric slab penetration into lower mantle beneath Sea of Okhotsk. *Journal of Geophysics-Zeitschrift Fur Geophysik*, 43, 473-496.

Lawrence, J., P. Shearer, 2008. Imaging mantle transition zone thickness with *SdS-SS* finite-frequency sensitivity kernels. *Geophys. J. Int.*, 174:143–158.

Li, C., R. D. van der Hilst, and M. N. Toksöz, 2006. Constraining P wave velocity variations in the upper mantle beneath Southeast Asia. *Phys. Earth Planet. Inter.*, 154, 180–195.

Li, C., R. D. Van der Hilst, E. R. Engdahl, and S. Burdick, 2008. A new global model for P-wavespeed variations in Earth's mantle. *Geochemistry, Geophysics, Geosystems*, vol. 9, Q05018, doi:10.1029/2007GC001806.

Miller, M. S., B. L. N. Kennett, and G. S. Lister , 2004. Imaging changes in morphology, geometry, and physical properties of the subducting Pacific plate along the Izu- Bonin-Mariana arc. *Earth Planet. Sci. Lett.*, 224(3–4), 363–370, doi:10.1016/j.epsl.2004.05.018.

Van der Hilst, R., E. R. Engdahl, W. Spakman, G. Nolet, 1991. Tomographic imaging of subducted lithosphere below northwest Pacific island arcs. *Nature*, 353, 37-43.

Van der Hilst, R. D., and T. Seno, 1993. Effects of relative plate motion on the deep structure and penetration depth of slabs below the Izu-Bonin and Mariana island arcs. *Earth Planet. Sci. Lett.*, 120(3–4), 395–407, doi:10.1016/0012- 821X(93)90253-6.

Richard, G., D. Bercovici and S. Karato, 2006. Hydration of the mantle transition zone by subducting slabs. *Earth Planet Sci. Lett.*, 251, 156–167.

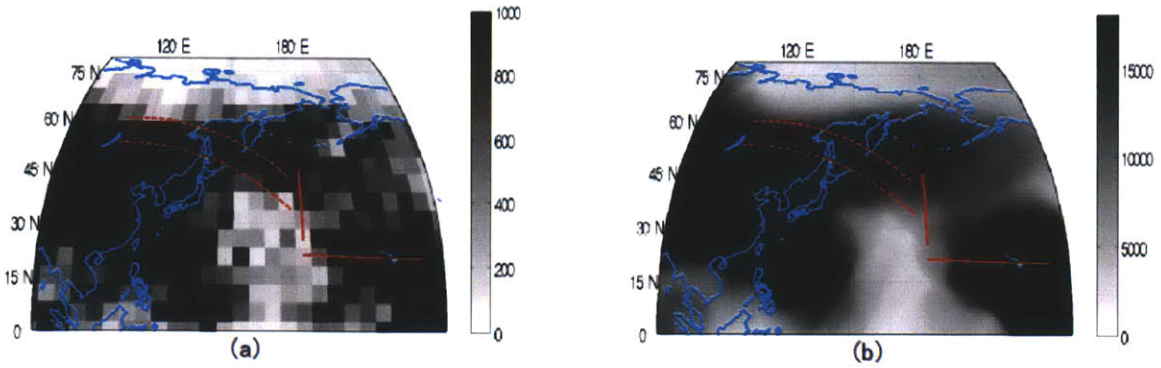

Figure 5-1. (a) the density map of the *SS* bounce points for each 5°×5° grid on the surface. (b) the GRT data distribution for each 1°×1° grid. The dark color means dense data coverage, while white color represents fewer data coverage. The two solid red lines in (a) and (b) represent the location of the two profiles shown in Figure 2-10a and Figure 3-2 (also in *Cao et al., 2010; Cao et al., 2011*). The two dashed red lines are two new images cross-sections shown in this Chapter. The coastlines are shown in cyan.

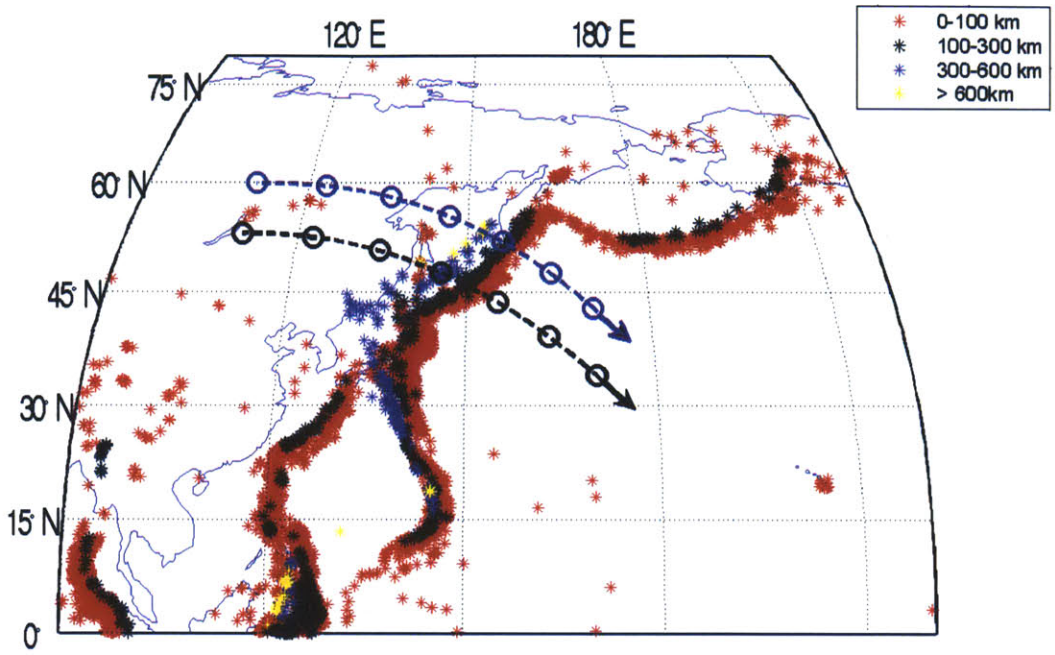

Figure 5-2. The subduction zone seismicity along the Kuril trench, shown as "*". Earthquake locations from the IRIS data management center from January of 1990 to June of 2011 are shown, with red color for events with focal depth between 0 and 100 km, black for events between 100 and 300 km, blue for events between 300 and 600 km, and yellow for events deeper than 600 km. The blue and black lines show the locations of the two new great-circle cross-sections (Figure 5-3 and Figure 5-4).

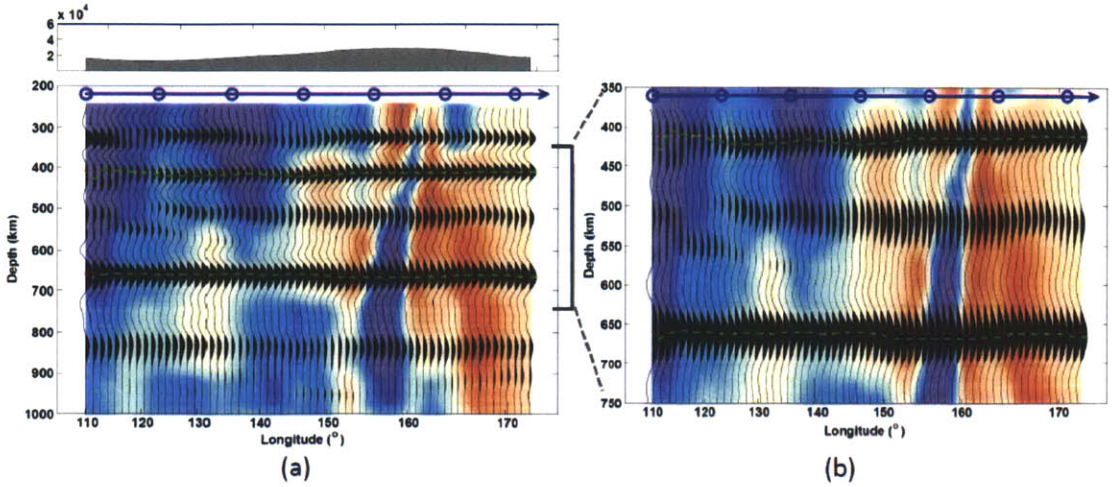

Figure 5-3. The GRT images for the blue cross-section in Figure 5-2 across the north part of the Kuril subduction zone. Left: seismic image superimposed on tomographic P-wavespeed variation from *Li et al. (2008)*. The red stars in the background color represent seismicity at this cross-section during January 1990 to June 2011. Red lines denote reference depth of 410 and 660 km. The depth profiles are corrected for 3D mantle heterogeneity (from tomography) and for the depth to the ocean floor where *SS* reflections occur. Right: blow up of image between 350 and 750 km depth, along with interpretation of 410' (dashed green line) and 660'(lower dashed green line) discontinuities. The top panel shows the numbers of seismograms contributing to each image depth profiles.

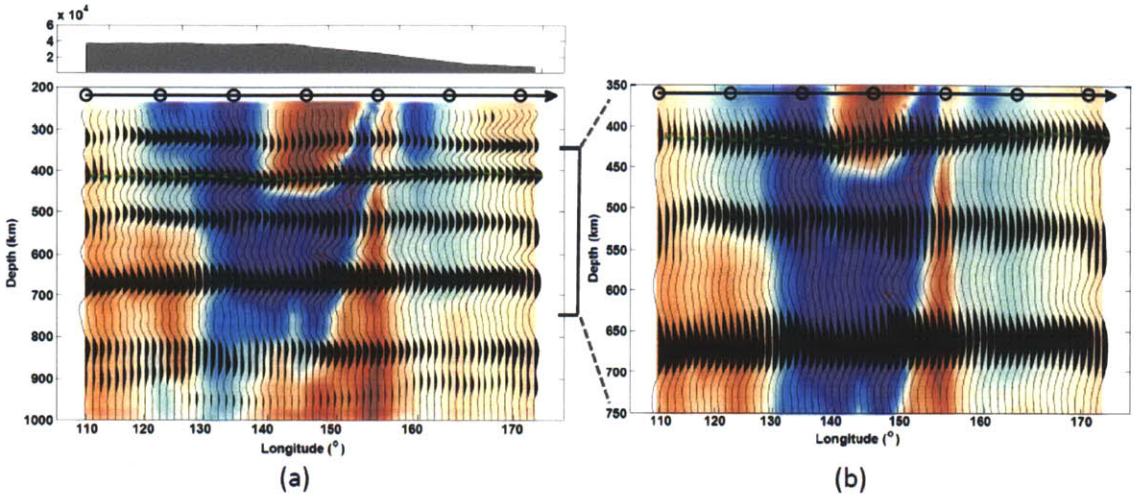

Figure 5-4. The GRT images for the black cross-section in Figure 5-2 across the south part of the Kuril subduction zone. Left: seismic image superimposed on tomographic P-wavespeed variation from *Li et al.* (2008). The tomography wavespeed model indicates a stagnant slab in the transition above around 660 km depth. The red stars in the background color represent seismicity at this cross-section during January 1990 to June 2011. Red lines denote reference depth of 410 and 660 km. The depth profiles are corrected for 3D mantle heterogeneity (from tomography) and for the depth to the ocean floor where *SS* reflections occur. Right: blow up of image between 350 and 750 km depth, along with interpretation of 410' (dashed green line). The 660' topography is not marked, because the broadening of the 660' signal near the high wavespeed structure makes it hard to determine the topography. The top panel shows the numbers of seismograms contributing to each image depth profiles. The *y*-axis is kept the same as in the upper panel of Figure 5-3a for easy comparison.

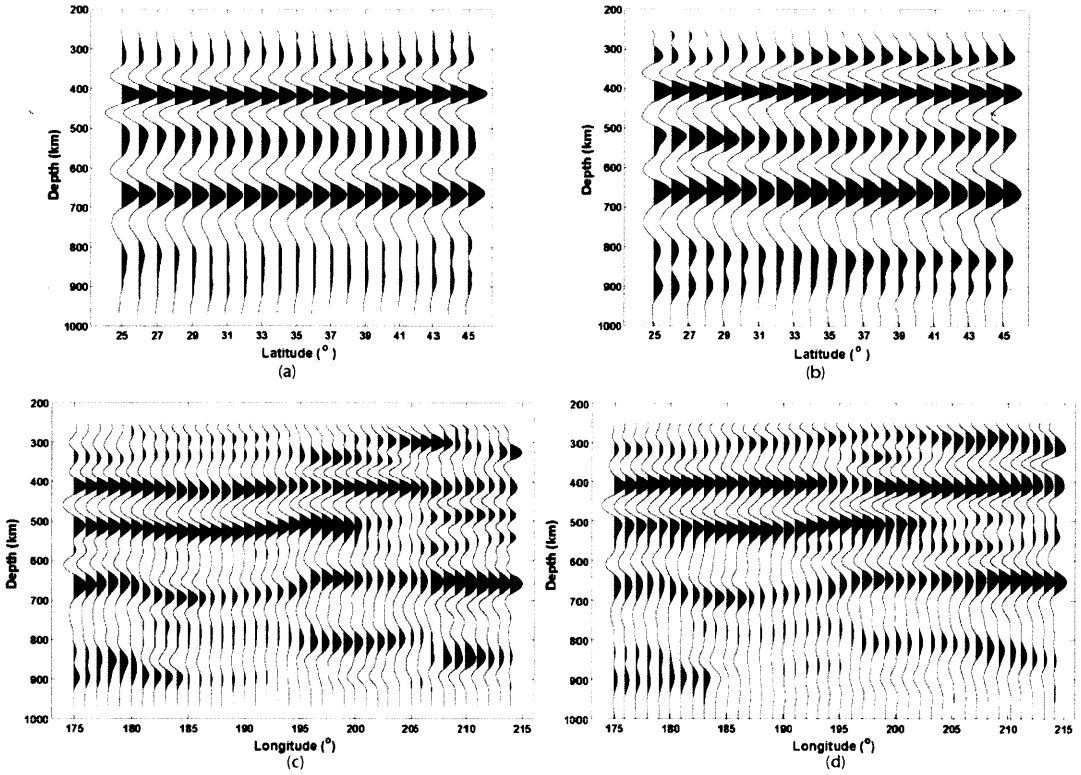

Figure 5-5. Comparison between the image profiles using old and latest dataset respectively. The left two figures (Figure 5-1a,c) show the same image profiles from Figure 2-10a and Figure 3-2 respectively, which are constructed with old dataset as specified in **Chapter II** and **Chapter III**. The right panels (Figure 5-1b,d) show the image profiles for the same geographic locations as the left profiles, but they are constructed using a recently updated dataset (including global seismic records till 2001 June). The location of the upper row profiles is the red solid vertical line in Figure 5-1. The location for the lower row profiles is the red solid horizontal line in Figure 5-1.

Chapter 6

Summary, concluding remarks, and future work

6.1 Summary

In this thesis, we developed a generalized Radon transform (GRT) to construct images of the mantle transition zone with the broadband wavefield of *SS* and its precursors. The GRT is an inverse-scattering technique that enables 3-D exploration type seismic imaging of the transition zone over large geographic regions far away from sources and receivers (such as oceans). The feasibility of this method is demonstrated in **Chapter II**, taking into account the influences of interfering phases and different types of noise.

We apply the GRT to study transition zone interfaces beneath part of the Pacific Ocean, including a tectonically stable cross-section in the northwest Pacific, a 40°×15° area surrounding the Hawaii islands, and the Kuril subduction zone. A total of about 1,600,000 transverse-component seismograms are used in our studies.

The GRT images of the transition zone beneath an oceanic region in the northwest Pacific far away from known down- and upwellings (**Chapter II**) are relatively simple to interpret. Pronounced and lateral continuous 410' and 660' signals show up in the images for all frequencies considered (20-50 s, 10-50s, 5-50s, 2-50s) with small (~10 km peak-to-peak) depth variation. The average depths to the 410' and 660' are 415±5 and 665±7 km, respectively, consistent with those of conventional *SS* stacking.

Frequency dependence of the images is observed, with a slight increase in depth variation of 410' and 660' and small scale structures showing up as frequency increases. The relative amplitude of 660' with respect to 410' amplitude becomes larger in higher frequency studies (5-50s, 2-50s). This may indicate that the 660' is a sharper phase boundary than the 410'. The 520' is a pronounced feature in the low frequency images of this part of the Pacific Ocean. In lower frequency images the widths of 520' signals are larger than those of the 410' and 660'. As frequency increases, the 520' signals begin to split, even when the 410' and 660' signals are not similarly affected. This frequency dependence of the 520' is consistent with the broad two-phase loop of the wadsleyite to ringwoodite transition, but it might also reflect phase transitions in non-olivine components that can be detected only with short-period data. In addition to the "usual suspects" (that is, the 410', 520', and 660'), the transition zone images also suggest presence of multiple, laterally intermittent interfaces near 350 km and between 800-1000 km depth.

The GRT images beneath the Central Pacific (**Chapter III**), including the Hawaii hotspot, reveal transition zone structures that are more complicated than expected. First order observations of interface depths suggest that Hawaii is located above the eastern margin of a large-scale topographic feature comprising a deep 410' (~430 km) and 660' (~700 km depth) and a thick transition zone, surrounded by shallow 660' (~640 km) and a thinner transition zone. Below and east of Hawaii the 660' is slightly shallower (~650 km) than the global average. West of 180°E the interfaces are near global average depths. This structural complexity suggests large variations in temperature (and, perhaps, composition) near the upper-lower mantle boundary beneath Hawaii and environs.

To estimate *in situ* mantle temperatures near the top (ΔT_{410}) and bottom (ΔT_{660}) of the transition zone we first use the Clapeyron slopes Γ of phase transitions in the olivine system in a mantle of pyrolitic bulk composition. Interpreting the observations in terms of transitions in $(Mg,Fe)_2SiO_4$ olivine

(olivine to wadsleyite, at~410 km, $\Gamma_{410}\approx$2.5 MPa/K (*Morishima et al., 1994*)), and ringwoodite to perovskite+ferropericlase (post-spinel) at ~660 km, $\Gamma_{p\text{-}sp}\approx$ –2.7 MPa/K (*Irifune et al., 1998*)) renders a temperature map with a weak perturbation ($\Delta T_{410}\approx\Delta T_{660}\approx$150K) below and east of Hawaii but larger anomalies ($\Delta T_{660}\approx$300K) further west, in accord with previous estimates (*Li et al., 2000; Collins et al., 2002*). The small ΔT_{410} on top of the west shallow 660' anomaly suggests that the broad anomaly is confined to the base of the transition zone. Further north, a deep *410'* and shallow *660'* suggest high temperatures in the upper mantle beneath the Hawaii chain.

Using $\Gamma_{p\text{-}sp}$ as above, a change in the post-spinel phase boundary from 640 to 700 km depth implies a temperature difference of ~850 K, which is unrealistic far away from plate margins. It is also unlikely that the enigmatic deep 660' is an artifact due to velocity anomalies not fully accounted for in the traveltime corrections with 3D mantle tomographic models, because such a deep 660' would then require implausible seismic and thermal anomalies. Therefore, for realistic values of $\Gamma_{p\text{-}sp}$, ΔT_{660}, and upper mantle velocities, the post-spinel transition does not seem a plausible explanation of the interface near 700 km depth.

We suggest that the interface depth changing from 640 to 700 km depth depicts a lateral change from the post-spinel transition (between Hawaii and 165°W) to the post-garnet transition (167-179°W, to the far west of Hawaii). The possibility of detecting a post-garnet transition seismically in high temperature region of the mantle is supported by multi-anvil experiments (*Weidner and Wang, 1998; Hirose, 2002; Nishiyama and Yagi, 2003*) and several previous seismic findings (*Deuss et al., 2006; Houser and Williams, 2010*). A Clapeyron slope $\Gamma_{p\text{-}gt}$=3.0 MPa/K for the post-garnet transition would yield and upper bound of 450 K.

The inference that the mantle near 660 km depth is hot west of Hawaii (ΔT_{max}~300–400K), over a region that is at least 800 km wide (if restricted to the shallow 660' area that is to the west of Hawaii)

but possibly as broad as 2,000 km (if the anomalous deep 660' to the further west of Hawaii is also included) is not consistent with the canonical picture of a narrow thermal plume rising from the lower mantle below the moving Pacific plate.

In **Chapter IV**, the geodynamical counterpart of **Chapter III**, we use finite-element modeling techniques to study the dynamical evolutions of plumes, using realistic earth's mantle parameters, and taking into account the influence of phase transitions at 410 and 660 km. We simulated plumes in a mantle environment with ambient convective flow. Our modeling reveals a variety of plumes that are different from the traditional thin, narrow mushroom type plume. Just as subducted slabs can be stagnant above the 660 km phase change (e.g. *Van der Hilst et al., 1991; Fukao et al., 1992*), in our simulations, hot plumes are also observed to pond beneath the transition zone, due to the inhibition effect of the endothermic phase change at 660 km depth. The hotspots at the surface may be triggered by secondary plumes emerging from the ponding of the primary plume head beneath the transition zone. The location of the center of the secondary plume might not coincide with the center of the primary plume. As a result of the plume ponding effect, the horizontal scales of the topography of the 660 km boundaries can be much larger than that of the 410 km phase boundaries. The geographic locations with the largest hot anomaly indicated by the depression of 410' may not necessarily be the locations with the maximum elevation of 660'. A simple anti-correlation between these two topographies no longer exists because of the complex interaction of mantle convection flow with the phase changes.

Inferring from the geodynamical simulation results, our seismic images are consistent with the scenario that, underneath Hawaii, hot material does not rise from the lower mantle through a narrow vertical plume but accumulates and spreads near the top of the lower mantle (the base of the transition zone), before being entrained in flow towards Hawaii and, perhaps, other islands. If this is true, Hawaii hotspot volcanism may be fueled by secondary upwellings from the base of the transition zone. This

scenario suggests complex material exchanges and heat transfer processes across the 660 km phase boundary, which might imply that geochemical observations based on hotspot lavas cannot constrain lower mantle domains directly.

In the preliminary GRT images of the Kuril subduction zone, we found a deepened 660' in the slab that penetrates directly into the lower mantle according to tomography results, and broadening of 660' at both edges of the slab when the slab is stagnant above the top of the lower mantle. However, 410' topography does not correlate with the tomography results.

6.2 Comparison between the transition zone thickness results by different groups and additional remarks on velocity-topography trade-off

In Figure 6-1, we show the global transition zone (TZ) thickness obtained by four different groups: *Deuss (2009), Houser et al. (2008), Gu et al. (2003) and Lawrence & Shearer (2008)*. In Figure 6-2, we show their regional results in the northwest and central Pacific together with our GRT results for Hawaii (from **Chapter III**). We plotted the TZ map from the GRT using a colormap similar to the maps on the left to facilitate comparison.

The four global TZ thickness maps (Figure 6-1) have some similarities at long wavelengths: for example, they all show thickening of the TZ at the west Pacific Rim; the Pacific Ocean generally has thiner TZ; there is some thickening of TZ beneath the Eurasia plate. However, at smaller scales (i.e. several degrees), these maps do not agree with each other well (see also Figure 6-2).

One possible explanation concernns the use of different data selection criteria (Table 6-1). However, this explanation should not be the major reason why they are so different. In each of the studies, a large number of seismograms have been stacked together to obtain the final results and make the maps. Stacking will suppress noise and enhance the signal-to-noise ratio (SNR). In principle, as the

number of data increases, the results should converge to within a reasonable error estimate (shown in *Deuss, 2009; Houser et al., 2008; Gu et al., 2003, and Lawrence and Shearer, 2008*, not shown here). This is not the case, however.

A more likely explanation lies in the imaging/inversion methods they used. As pointed out in **Chapter III** (section S3.3.4), there is a trade-off between the choice of velocity model and the discontinuty topographies when explaining the traveltime of *SS* precursors. *Deuss (2009)* and the GRT method outlined in this thesis separated the inversions for TZ discontinuity topographies and 3-D velocity perturbations. In these studies, independent tomographic models re assumed and used to map the traveltime (or time series) to depth (image points). The other three studies (*Houser et al., 2008; Gu et al., 2003 and Lawrence and Shearer, 2008*) all used a joint inverison scheme to simultaneously invert for mantle velocity anomalies and 410' and 660' topographies using a variety of non-precursors and *SS* precursors travel time data.

Of the four maps in the left panel of Figure 6-2, the maps by *Houser et al. (2008)* and *Lawerence and Shearer (2008)* share the most similarities. They both adopted a joint inverision of velocity and TZ discontinuity topographies. Also, they used the same stacking cap radius (5°, see table 6-1), so their resolution is comparable. The differences may result from the different travel time sensivity kernels. *Houser et al. (2008)* used a 1-D traveltime sensitivity kernel of SS precursors to invert TZ topographies (*Dziewónski and Gilbert, 1976*). *Lawerence and Shearer (2008)* ultilized a 3-D finite frequency kernel (*Dahlen, 2005*), which should in principle produce higher resolution maps compared to studies using 1-D sensitivity kernels. But the smoothing/regularization during the inversion process seems to reduce the resolution difference between these two studies.

Gu et al. (2003) also inverted the velocity and TZ topographies simultaneously, but they used a 10° radius stacking cap instead of 5° radius. The large stacking cap lowers the resolution compared to that of *Houser et al. (2008)* and *Lawerence & Shearer (2008)*. The averaging of TZ thickness caused by

stacking over large areas and the smoothing during the inversion process make the amplitudes of TZ thickness found by *Gu et al. (2003)* smaller than that of *Houser et al. (2008)* and *Lawerence and Shearer (2008)*.

Instead of joint inversion, *Deuss (2009)* and the GRT in this thesis both used independently derived velocity models to invert for the TZ thickness. Some simliarities exist, e.g. they both show a thicker-than-average TZ to the west of Hawaii, although the exact locations of the thickening differ. Deuss used a 10° stacking cap. The lateral resolution of this study is several thousands kilometers, so it may represent an averaged version of the TZ thicknesss obtained by the GRT. Due to the uneven data coverage within each stack bin, the TZ thickness in each bin may be biased by the most densely sampled spots in that stack bin.

The differences between the results yielded by these two groups of methods (joint inversion vs. TZ thickness only) can be attributed to several factors. First, the three joint inversion studies all assume the global existence of 410' and 660', ignoring the existence of other interfaces in the transition zone (e.g. 520', and possible intermittent interfaces at around 350 km and between 800 km and 900 km). Only the topographies of 410' and 660' are included in the paramterization of their inversions. The velocity jumps at 520' or at the other interafaces will also affect the traveltime of *SS* precursors. In the common-midpoint-stacking (CMP, see Chapter II) method by *Deuss (2009)* and the GRT method, we do not need to make any assumptions about the existence of scatters/interfaces/reflectors at other depths. The signals from all the interfaces will show up automatically in the final images. Second, the three joint inversion studies all pick the *SS* precursor traveltime (after stacking), and then try to invert the velcoity and topographies paramters that best explain the traveltime. By picking only the traveltime, important information about the waveforms is lost. In the CMP method and in the GRT, the entire waveform is used for stacking/imaging. Third, the joint-inversion studies assume that 410' and 660' are both first-order velocity discontinuties that will generete reflecting and converted waves. In fact, 410'

and 660' are caused by phase transition loops with certain widths. It is uncertain how these assumptions will affect the traveltime estimates in the forward modeling of inversion process using high frequency data (e.g. 10~50s as in *Lawerence and Shearer (2008)*). Fourth, and perhaps most importantly, we know from inversion theory that with more parameters we can explain the data better. So adding the velocity models into parameterization may give a better fit of the *SS* precursors traveltime. However, if the model that fits the data with an acceptable degree of error is non-unique, we can obtain different inversion results using the different choices of regularization. This non-uniqueness can explain the differences between different joint-inversion results. Moreover, the discontinuity topographies derived from stacking inversion together with the independently derived tomography velocity models may also belong to this solution space.

Which method is better? Joint inversion or topography-only inversion?

Admittedly, we face a trade-off between velocity and topographies in applying the GRT. We rely on independently dervied tomography models and assume that they are accurate. Joint inversions of both upper mantle velocities and transition zone discontinuty topographies can prevent possible inaccuracies in topography estimates introduced by independently derived tomography models. However, joint inversion based on traveltime seems to give non-unique solutions. Finding a self-consistent way to simultaneously invert for velocity perturbation and interface depth with waveform technqiues such as the GRT is a target of future research.

6.3 Future work

We have carried out various synthetic tests to establish the feasibility and accuracy of the GRT method using WKBJ synthetic seismograms (see **Chapter II**, section 2.4). For more rigorous tests we need to consider more complete synthetics. Calculating synthetic waveforms for realistic event and station

distributions and 3-dimensional velocity models is, still, computationally too demanding. For example, using the SEM (*Komatitsch et al., 1999; Tromp, 2001*) codes, calculating the global synthetic seismograms for a single event requires 1-2 days, using currently available computing resources, and we use thousands of events for GRT imaging. The use of, for instance, full reflectivity synthetics would be better than WKBJ synthetics. In parallel, analytical methods to quantify the resolution of the GRT method, taking into account the uneven distribution of events and stations in global seismology, need to be developed.

When we started this thesis work five years ago, the Pacific Ocean was the most densely sampled area with *SS* bouncing points, which is why we began working in this area. Today, with the increase in the deployment of the seismic stations worldwide, and the rapidly growing amount of high quality waveform data, the GRT can be applied to more areas around the world. Also, in our Hawaii study, we used seismograms filtered between 20s and 50s, but, as we demonstrated in **Chapter II**, data filtered with higher frequency bandwidth may still generate images above the ambient noise if an appropriate data selection method is used. Higher frequency studies may help put constraints on multi-scale structures of the phase transitions (i.e. how mineral properties change within the phase transition loop).

References Cited

Collins, J. A., F. L. Vernon, J. A. Orcutt, and R. A. Stephen, 2002. Upper mantle structure beneath the Hawaiian swell: Constraints from the ocean seismic network pilot experiment. *Geophys. Res. Lett.* 29, 1522.

Dahlen, F.A., 2005. Finite-frequency sensitivity kernels for boundary topography perturbations.

Geophys. J. Int., 162, 525–540.

Deuss, S. A., T. Redfern, K. Chambers, and J. H. Woodhouse, 2006. The nature of the 660-kilometer discontinuity in Earth's mantle from global seismic observations of PP precursors. *Science*, 311, 198.

Deuss, A. , 2009. Global Observations of Mantle Discontinuities Using *SS* and *PP* Precursors. *Surveys in Geophysics*, 30 (4). 301-326.

Dziewónski, A. M. and F. Gilbert, 1976. The effect of small, aspherical perturbations on travel times and a re-examination of the corrections for ellipticity. *Geophys. J. R. astr. Soc.*, 44, 7–18.

Fukao, Y., M. Obayashi, H. Inoue, and M. Nenbai, 1992. Subducting slabs stagnant in the mantle transition zone. *J. Geophys. Res.*, 97, 4809-4822.

Gu, Y., A. M. Dziewonski, and G. Ekström, 2003. Simultaneous inversion for mantle shear wave velocity and topography of transition zone discontinuities. *Geophys. J. Int.*, 154:559–583.

Hirose, K., 2002. Phase transitions in pyrolitic mantle around 670-km depth: Implications for upwelling of plumes from the lower mantle. *J. Geophys. Res.*, 107, (B4), 2078.

Houser, C., G. Masters, M. Flanagan, and P. Shearer, 2008. Determination and analysis of long-wavelength transition zone structure using SS precursors. *Geophys. J. Int.*, 174:178–194

Houser, C., and Q. Williams, 2010. Reconciling Pacific 410 and 660 km discontinuity topography, transition zone shear velocity patterns, and mantle phase transitions. *Earth Planet. Sci. Lett.*, 296, 255.

Irifune, T., N. Nishiyama, K. Kuroda, T. Inoue, M. Isshiki, W. Utsumi, K. Funakoshi, S. Urakawa, T. Uchida, T. Katsura and O. Ohtaka, 1998. The postspinel phase boundary in Mg_2SiO_4 determined by in situ X-ray diffraction. *Science,* 279, 1698.

Lawrence, J., and P. Shearer, 2008. Imaging mantle transition zone thickness with *SdS-SS* finite-frequency sensitivity kernels. *Geophys. J. Int.* ,174:143–158.

Kennett, B. L. N., E. R. Engdahl, and R. P. Buland, 1995. Constraints on seismic velocities in the Earth from travel times. *Geophys. J. Int.*, 122, 108-124.

Komatitsch, D., C. Barnes, and J. Tromp, 1999. A spectral element method for wave propagation simulation near a fluid-solid interface. *Proceedings of the First ACES Workshop*, editor P. Mora, University of Queensland, Australia.

Li, X., R. Kind, K. Priestley, S. V. Sobolev, F. Tilmann, X. Yuan and M. Weber, 2000. Mapping the Hawaiian plume conduit with converted seismic waves. *Nature*, 405, 938.

Morishima, H., T. Kato, M. Suto, E. Ohtani, S. Urakawa, W. Utsumi, O. Shimomura, and T. Kikegawa, 1994. The phase boundary between agr- and beta-Mg_2SiO_4 determined by in situ X-ray observation. *Science,* 265, 1202.

Nishiyama, N., T. Yagi, 2003. Phase relation and mineral chemistry in pyrolite to 2200°C under the lower mantle pressures and implications for dynamics of mantle plumes. *J. Geophys. Res.*, 108, 2255.

Tromp, J., 2001. Opinion: Dawn of a new era in computational global seismology. *Seism. Res. Lett.*, 72, 639–641.

Van der Hilst, R. D., R. Engdahl, W. Spakman, and G. Nolet, 1991. Tomographic imaging of subducted lithosphere below northwest Pacific island arcs. *Nature*, 353, 37-43.

Weidner, D. J., and Y. Wang, 1998. Chemical- and Clapeyron-induced buoyancy at the 660 km discontinuity. *J. Geophys. Res.*, 103, (B4), 7431.

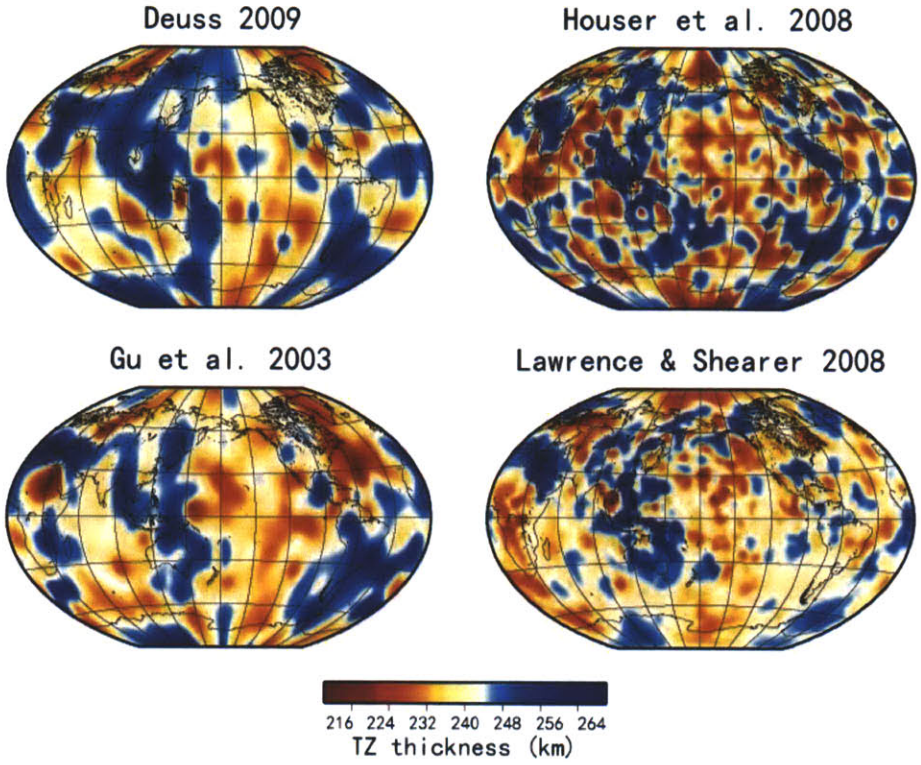

Figure 6-1. Global TZ thickness maps by different groups. Figure from *Deuss (2009)*.

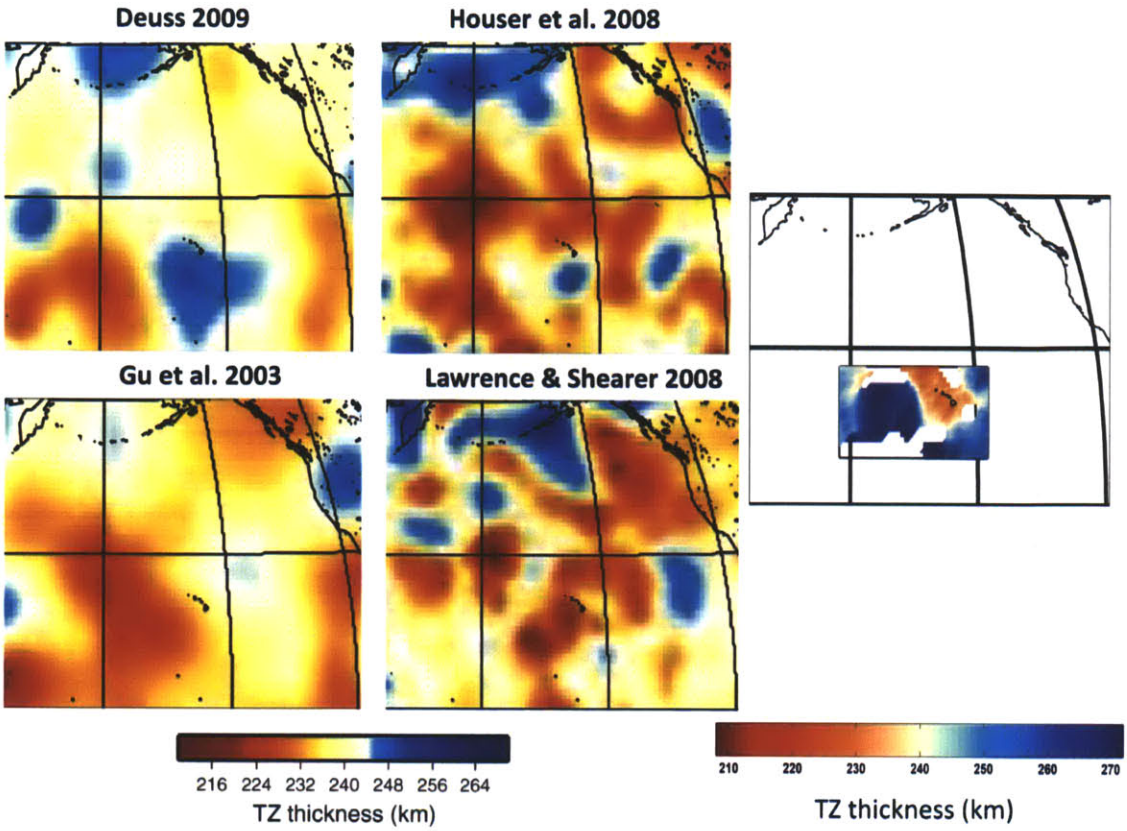

Figure 6-2. Regional maps of TZ thickness in part of the Pacific including the Hawaii islands. On the right, we show the TZ thickness obtained by the GRT from **Chapter III** Figure 3-3.

Table 6-1. Data selection criterions and preprocessing processes by different groups.

	Deuss 2009	Houser et al. 2008	Gu et al. 2003	Lawrence & Shearer 2008	Our study
	TZ topography only	Joint inversion of TZ topography and velocity	Joint inversion of TZ topography and velocity	Joint inversion of TZ topography and velocity	TZ topography only
Epicenter distance range	[100° 160°]	[110° 180°]	[100° 160°]	[110° 175°]	[90° 170°]
Source magnitude	[6.0 7.0]	>5.5	>5.5	>5.8	>5.2
Focal depth	<75 km	<75 km	<75 km	<30 km	<75 km
SNR criterion*	3	n/a	Automatic and interactive editing	3	cluster analysis correlation coef >0.5
Dataset year	January 1st 1980-March 27th, 1998	1976 -2005	n/a	1976-2004	1980-2010
Bandpass filter	15-75 s	n/a	15-100 s	10-50s	20-50s
Pick SS phase	Maximum pulse	Cluster analysis to determine SS arrivals	Correlation with SS phase	n/a	Maximum pulse
Stack cap radius	10°	5°	10°	5°	No stacking

*In computing SNR, the signal is defined as the maximum amplitude of the SS arrival in a ~60s time window around the predicted main phase arrival, and the noise is defined as the maximum amplitude in the precursor window.